

論文 / 著書情報
Article / Book Information

題目(和文)	
Title(English)	Improvement of SAFT by Implementation of Approximate Wave Solution for Ultrasonic Beam Radiation
著者(和文)	P.WORAWIT
Author(English)	Worawit Padungsriborworn
出典(和文)	学位:博士(学術), 学位授与機関:東京工業大学, 報告番号:甲第10043号, 授与年月日:2015年12月31日, 学位の種別:課程博士, 審査員:廣瀬 壮一,岩波 光保,井上 裕嗣,アニール ワイジェ,佐々木 栄一
Citation(English)	Degree:., Conferring organization: Tokyo Institute of Technology, Report number:甲第10043号, Conferred date:2015/12/31, Degree Type:Course doctor, Examiner:,,,,
学位種別(和文)	博士論文
Type(English)	Doctoral Thesis

Improvement of SAFT by Implementation of Approximate Wave Solution for Ultrasonic Beam Radiation

Worawit Padungsriborworn

Submitted to the Department of Civil Engineering
in Partial Fulfillment of the Requirements for the Degree of
Doctor of Philosophy

**Department of Civil Engineering, Tokyo Institute of Technology
2015**

Improvement of SAFT by Implementation of Approximate Wave Solution for Ultrasonic Beam Radiation

Worawit Padungsriborworn

Supervisor: Professor Sohichi Hirose

Submitted to the Department of Civil Engineering
in Partial Fulfillment of the Requirements for the Degree of
Doctor of Philosophy

**Department of Civil Engineering, Tokyo Institute of Technology
2015**

Abstract

Synthetic Aperture Focusing Technique (SAFT) is a signal processing technique that has evolved the way in the presentation of the inspection results in an ultrasonic testing (UT). By using this technique, complicated A-scan waveform signals are synthesized, thus the internal images of materials and structures are reconstructed. SAFT has been widely used in Non-Destructive Evaluation (NDE) due to its simplicity and speedy calculation. However, precise results cannot be obtained in some cases because the conventional SAFT considers ultrasonic waves radiating at the same intensities in the radial directions, which is different from the actual wave phenomenon. Many researches for the improvement of SAFT performance show that the wave theory is a key point to efficiently improve such popular imaging technique.

This dissertation proposes the rectification of the above mentioned weak point by implementation of the Approximate Wave Solution (AWS) of the ultrasonic beam radiation into SAFT. AWS is an explicit solution which uses a stationary phase method to reduce double surface integration in the Kirchhoff Beam Transmission model into a Surface Integral model, thus the computation becomes less time-consuming. Ultrasonic beam radiation modelled using AWS is implemented into SAFT algorithm by a simple multiplication. The improved version of SAFT is called the AWS-SAFT. The characteristics of the proposed AWS-SAFT are confirmed in a water immersion test and a contact transducer test.

Mutual improvement effects which are observed from both test configurations are: (1) artifacts from longitudinal wave mode which are normally appeared in transverse wave mode results can be eliminated and (2) image reconstruction of flaw located inside the region where the intensities of AWS are high will be much clearer than the conventional SAFT i.e. flaw image in AWS-SAFT has narrower side lobes with overall noise reduction. One drawback of AWS-SAFT is that noises over the region where the intensities of AWS are high will be highly amplified, thus sometimes it may obscure the flaw image. However, this drawback can be overcome by the use of Structural Similarity (SSIM) index in the detection of differences between images from non-defect test medium (a benchmark) and a defective one.

AWS can also be used to predict the region in a test medium where high imaging capability can be anticipated. The concept of using AWS in such a way is proposed as an Effective Region (ER) theory. ER is defined as a region of a test medium where a defect will be definitely reconstructed using AWS-SAFT. The cutoff value to be used as a boundary of ER is investigated and proposed. Finally, a case study considering the real inspection problem is given and the results from applying the ER technique and AWS-SAFT to such problem verifies that validity of ER technique while also well demonstrate the performances of AWS-SAFT.

Acknowledgements

First of all, I would like to express my first gratitude to Professor Sohichi Hirose for his kind advice and fruitful supervising throughout my PhD study. Thanks to Chulalongkorn University for selecting me as a candidate for Nikon-Chulalongkorn scholarship. Many thanks to Nikon Corporation for a long financial support. Without this help, it is totally impossible for a student of poor financial background like me to study in a PhD course at this high ranked university.

Another deep gratitude is paid to Mr. Nattaphob and Mr. Nattaphong Rattanasuwanthawee of the SC Group (Thailand) for the very kind financial support during my final semester. Thank you Mr. Tiratas Suwathep and his family for lending me a tuition fee for my final semester. Thank you Mr. Pracha Khamphakdi for letting me share a room during my final semester. Without helps from these people, I might have been in a big trouble.

Thank you my family for the everlasting warmth and kindness which does not attenuate whether we are so far away. Thank you Ms. Chadcharin Thanyapot for the kindest encouragement during my stay in Japan. Thank you the Tokodai 3G gang who shared exciting times along the way we walked together in Japan.

Thank you Mr. Keita Sakuma and Mr. Kenichi Ishimatsu who supported me a lot when I was working part-time at Sankus (Oimachi). Thank you my comrades at Tokyo Chikara Meshi (Oimachi) who helped me a lot when I was working part-time there.

Finally, I would like to express my deepest gratitude to Dr. Akira Furukawa who guided me, a proper way to conduct a research. He is the one who taught me many things while also understanding my circumstance as a friend, hence eventually, I can finish this dissertation.

At the very final, I would like to thank myself for never giving up, no matter what happened.

Table of Contents

	Page
Chapter 1: <i>Introduction</i>	
1.1 Background	1
1.2 Objectives	3
1.3 Outline of dissertation	4
Chapter 2: <i>Development of the AWS-SAFT</i>	
2.1 Fundamental of ultrasonic testing	5
2.1.1 Refraction and mode conversion	7
2.1.2 Test configurations in UT	8
2.1.3 Representation of UT result	10
2.2 Principle of SAFT	12
2.2.1 SAFT in a single medium case	13
2.2.2 SAFT in a two media case	16
2.3 Modelling of ultrasonic beam radiation by the Approximate Wave Solution (AWS)	18
2.3.1 AWS of fluid-solid two phase media with curved interface	19
2.3.2 AWS of two solids media with planar interface	25
2.3.3 Verification of AWS using actual beam measurement	30
2.4 AWS-SAFT	33
2.4.1 Implementation of AWS into SAFT in water immersion test	33
2.4.2 Implementation of AWS into SAFT in contact transducer test	36
2.5 Summary	40
Chapter 3: <i>Application of AWS-SAFT in water immersion ultrasonic test</i>	
3.1 Experimental setup	41
3.2 Study on characteristics of an AWS-SAFT image	45
3.3 Efficient way to obtain ultrasound images of SDHs in a rod specimen by AWS-SAFT	56
3.4 Summary	64
Chapter 4: <i>Application of AWS-SAFT in angle beam ultrasonic test</i>	
4.1 Experimental setup	66
4.2 Characteristics of AWS-SAFT	68
4.3 ER technique and AWS-SAFT	70
4.3.1 Effective Regions for each wave mode of AWS-SAFT	70
4.3.2 Experimental verification of ER technique	71

4.4 A case study: Imaging of steel bottom defect	79
4.4.1 Outline of studied problem and experimental setup	79
4.4.2 Experimental results	81
4.4.3 Additional results	85
4.5 Summary	87
Chapter 5: <i>Conclusions</i>	
5.1 Review of dissertation	89
5.2 Summary of findings	89
5.3 Limitation in using the AWS-SAFT	91
5.4 Future works	92
Appendix A: <i>Structural SIMilarity (SSIM) index</i>	93
References	98

List of Figures

Figure	Page
2.1 Longitudinal and transverse wave modes.	6
2.2 Wave refraction at the interface.	7
2.3 Pulse-echo test configuration.	9
2.4 Pitch-catch test configuration.	9
2.5 A-Scan presentation.	11
2.6 B-Scan presentation.	11
2.7 C-Scan presentation.	12
2.8 SAFT computation at a non-defect part in a single medium case.	14
2.9 SAFT computation at a defect in a single medium case.	15
2.10 Outline for SAFT in a two media case.	17
2.11 Outline of water immersion test.	20
2.12 L-mode beam radiation.	23
2.13 T-mode beam radiation.	24
2.14 Outline of contact transducer test.	25
2.15 L-mode beam radiation models of transducer ch.16.	28
2.16 T-mode beam radiation models of transducer ch.16.	29
2.17 Verification of actual beam radiation in a single medium.	31
2.18 L-mode verification of actual beam radiation in two solids media.	32
2.19 T-mode verification of actual beam radiation in two solids media.	32
2.20 L-mode AWS-SAFT for transmitter $i = 32$ and receiver $j = 32$.	35
2.21 T-mode AWS-SAFT for transmitter $i = 64$ and receiver $j = 64$.	35
2.22 Test configuration for sub-section 2.4.2.	36
2.23 L-mode AWS-SAFT for transmitter $i = 8$ and receiver $j = 24$.	38
2.24 T-mode AWS-SAFT for transmitter $i = 8$ and receiver $j = 24$.	39
3.1 64 channels linear phased-array transducers.	42
3.2 Pulser-receiver and wave acquisition system.	43
3.3 A typical rod specimen.	43
3.4 Outline of water immersion test.	44
3.5 Photo of experimental setup.	44
3.6 L-mode summed AWS beam radiations from all 64 transducers.	46
3.7 T-mode summed AWS beam radiations from all 64 transducers.	46
3.8 Specimens for experiment step 1.	47
3.9 Case 1A results when SDH is inside the ER of L-mode.	48-49
3.10 Case 1B results when SDH is inside the ER of T-mode.	50-51
3.11 Case 1C results when SDH is outside the ER of L-mode.	52-53
3.12 Case 1D results when SDH is outside the ER of T-mode.	54-55
3.13 L- and T-mode combined ER in case transducer on top and bottom.	57
3.14 Specimen for experiment case 2A and its ERs.	59
3.15 Specimen for experiment case 2B and its ERs.	59
3.16 Case 2A results where both d_1 and d_2 are inside the ER of T-mode.	60-61

Figure	Page
3.17 Case 2B results where d1 and d2 are inside the ERs of L- and T-modes.	62-63
4.1 32-channels phased-array transducers with PS wedge.	67
4.2 Pulser-receiver system.	67
4.3 Typical setup for experiments in this Chapter.	68
4.4 L-mode experimental result.	69
4.5 T-mode experimental result.	69
4.6 L-mode ABR using $\theta_{PA} = 16^\circ$.	71
4.7 T-mode ABR using $\theta_{PA} = 38^\circ$.	71
4.8 Case-L1 results testing $\chi = 0.075$.	72
4.9 Case-L2 results testing $\chi = 0.05$.	73
4.10 Case-L3 results testing $\chi = 0.025$.	74
4.11 Case-T1 results testing $\chi = 0.125$.	75
4.12 Case-T2 results testing $\chi = 0.1$.	76
4.13 Case-T3 results testing $\chi = 0.05$.	77
4.14 Case-T4 results testing $\chi = 0.025$.	78
4.15 Photo and illustration of Kisogawa bridge case.	80
4.16 Simplified model used in this study.	80
4.17 Typical setup of experiment in this section.	80
4.18 Case-1: $L = 1$ mm.	82
4.19 Case-2: $L = 10$ mm T-mode.	83
4.20 Case-3: $L = 20$ mm T-mode.	84
4.21 Circular notch: $L = 1$ mm T-mode.	85
4.22 Triangular notch: $L = 1$ mm T-mode.	86
A1 Results from conventional SAFT	96
A2 Results from AWS-SAFT	97

List of Tables

Table	Page
2.1 Material properties used in water immersion test.	22
2.2 Material properties used in contact transducer test.	27

Chapter 1: *Introduction*

1.1 Background

Many of crucial infrastructures such as bridges and dams had been constructed since the middle of the 20th century. In other words, they have been in-service for more than 50 years. Properly designed and built structures are supposed to maintain through their design life specified in the design codes [1, 2]. However, without appropriated maintenance, they may encounter sudden collapses due to structural deficiencies such as fatigue cracks and corrosions [3]. Structural health monitoring [4] is becoming a significant part in society because failure of an infrastructure lead to catastrophes to life and assets. Understanding of the flaw propagation mechanisms can help to predict the detrimental effects from defects on structural performance. However, a reliable method to locate defects before they become severe enough to cause a catastrophic damage is required. Such importance has been drawing mass attentions from researchers and engineers into the development of techniques to precisely identify flaws and defect by means of quantitative information such as size, shape and location.

Nondestructive testing (NDT) techniques have been playing an important role for some decades since they can be used to assess flaws and defects inside materials and structures in a harmless manner. The five standard discipline, defined by United States Army [5], can be classified into two categories using the locations of flaws and defects to be inspected. Category 1: Liquid Penetrant testing, Magnetic Particle testing and Eddy Current testing are disciplines for the inspection of the defects which are already appearing on the surface of target. Category 2: Radioactive testing, and Ultrasonic testing are used for the inspection of internal defects. Method of NDT was once considered an empirical technology based on judgment of skilled operators and a benchmarking. However, acceptable results were obtained for decades in simple applications. Concept of quantitative nondestructive evaluation (QNDE), introduced by Achenbach [6] had emerged the possibility for NDT to deal with much advanced applications. Among a bunch of quantitative measurement techniques, *imaging techniques* had high potential in generalizing results, hence non-specialized personnel can understand, visually. Ultrasonic testing (UT) and Radioactive testing (RT) are two typical imaging techniques which had been using in both medical field and nondestructive evaluation until now.

Study on imaging capabilities between UT and RT was conducted by Light [7]. At the meantime, RT could provide clearer defect image than UT. However, developments of techniques which combines UT and digital visual imaging has great potential in improving the resolution of UT image. Considering the drawbacks of RT due to its hazardous properties, a feasibility study to replace RT with UT was studied by Moran et al [8]. Research on the UT is considered worthwhile because it has high potential to replace the use of hazardous substance required in RT. Two interesting points in further development of UT imaging are as follows:

1. Improvement of signal processing algorithm to obtain more precise image
2. Assessment of efficient test method in a specific test situation.

One of the most efficient signal processing techniques to obtain ultrasound image is Synthetic Aperture Focusing Technique (SAFT).

SAFT has evolved the way in the interpretation of UT results since its first development in 1974 by the US Nuclear Regulatory Commission (NRC) at the University of Michigan [9]. SAFT applies the same concept as in Synthesis Aperture Radar (SAR) which is an imaging technique utilizing microwave [10]. The principle of SAFT is explained in detail by Seydel [11] and a review of SAFT development was reported by Doctor et al. [12]. With this signal processing technique, high resolution ultrasound image of the scanned volume can be obtained by applying SAFT algorithm to a series of UT waveform signals from many independent probe positions. Transverse and longitudinal resolution of SAFT was studied by Thomson [13]. Experiences with SAFT in field measurement were introduced by Schmitz et al. [14]. Strong points of SAFT lay on its simple and flexible algorithm. Improvement of signal-to-noise ratio (SNR) can be obtained by superposition of signals from independent probe positions, hence flaw echo buried inside the noises become visible.

SAFT was originally developed for use with single element transducer where the transducer was scanned along a line to collect waveform signals. Therefore, acquiring waveform signals from various probe positions was quite a tedious task until the invention of phased-array technology at the end of the 20th century following the same principle as phased-array radar technology [15]. Using an array of ultrasonic transducers, waveform signals can be easily obtained within a short time. Preliminary use of array system for the inspection of weldments was conducted by Lamarre et al. in 1999 [16]. Several years later,

Drinkwater et al. reviewed a meantime research progress in the use of ultrasonic arrays for NDE which offering a step change over the traditional monolithic transducer [17]. Signal processing on vast amount of data is not a problem because computer technology has also been developing dramatically in parallel with the phased-array technology.

However, drawback of SAFT is a by-product of its algorithmic simplicity. Hence, improvement of ultrasound imaging techniques based on a conventional SAFT algorithm had drawn attentions from engineers and researchers for decades in both time and frequency domains. In frequency domain, SAFT is treated as a special solution of the inverse scattering problem [18-20]. Another example of SAFT improvement is by allowing the use of multiple reflections [21, 22]. The most recent state-of-the-art review on SAFT was written by Spies et al. [23]. Such accomplishments in improvement of SAFT show that *wave theory* is a key point in getting high accuracy ultrasound image since it can predict the characteristic of utilized wave resulting in good approximation of reality. One of the wave characteristics which has high potential in improving SAFT algorithm is a beam radiation inside a target object. Ultrasonic beam radiations can be explicitly computed by approximate wave solution (AWS) derived by Schmerr [24] and accounted into SAFT to improve an ultrasound image [25]. It is reported that observed improvement effects are (1) to get better contrast and (2) to eliminate artifacts from multiple reflections of longitudinal wave in transverse wave mode. However, the implementation method was still ambiguous, hence it is necessary to create a clear method to implement AWS into SAFT.

1.2 Objectives

This dissertation has three objectives. The first and main objective is to find an efficient way to implement AWS into SAFT. The improved version of SAFT using AWS is called the AWS-SAFT. Second objective of this dissertation is to confirm the improvement effects or the characteristics of AWS-SAFT. Finally, efficient ways to use AWS-SAFT are proposed using the demonstrations from two case studies. The performance of AWS-SAFT is experimentally tested in water immersion test and angle beam test which are two fundamental test configurations in UT.

Objectives of this dissertation can be listed as follows:

- I. To define a clear implementation method to account AWS into SAFT
- II. To confirm the characteristics of AWS-SAFT
- III. To propose an effective way to use AWS-SAFT

1.3 Outline of dissertation

This dissertation is organized into 5 chapters and the first chapter is this introduction.

Chapter 2 presents the theoretical background necessary to understand the work developed further in this dissertation. The principle of SAFT in single medium problem is first explained and followed by the extension into the two media. Then, modelling of ultrasonic wave radiation by using the AWS is explained separately for two cases which are: (1) fluid-solid water immersion test and (2) solid-solid angle beam test. Experimental verification of beam radiation model is reported to cross-check our approximation with the actual wave phenomenon. Then, the implementation method of the AWS into SAFT algorithm is defined and demonstrated. AWS-SAFT is defined in the final section of this chapter. At this stage, objective I is accomplished.

In Chapter 3, AWS-SAFT is first applied to a water immersion test of an aluminum rod processed with a side-drilled hole (SDH) to check the characteristics of AWS-SAFT, to fulfill objective II. AWS-SAFT is further applied to an immersed aluminum rod with two SDHs to propose an efficient way to use AWS-SAFT in imaging of SDH in arbitrary position, thus objective III is accomplished.

In Chapter 4, AWS-SAFT is applied to an angle beam transducer test of a steel plate processed with an SDH to check the characteristics of AWS-SAFT in fulfillment of objective II. Then, ER theory is proposed as another way to use ultrasonic beam radiation modelled from AWS. ER theory can predict the region of tested volume where high imaging capability can be anticipated. ER theory is experimentally verified using AWS-SAFT. Finally, a case study from Kisogawa bridge is introduced to demonstrate the use of ER theory in real inspection problem. Using ER theory, an efficient way to use AWS-SAFT in any arbitrary test configuration is proposed, hence objective III is accomplished.

A wrap-up of this dissertation is given in chapter 5 starting with an overall review, followed by main findings from the accomplishment of objectives I, II and III. Eventually, future works are given as an intuition for further development of AWS-SAFT and ER theory.

Chapter 2: *Development of AWS-SAFT*

This chapter presents the development process of AWS-SAFT. First, the fundamental of ultrasonic testing is brief in section 2.1 followed by the principle of SAFT in section 2.2. Method for the modelling of ultrasonic beam radiation using Approximate Wave Solution (AWS) is explained in section 2.3 with an experimental verification. Then, the implementation method to account AWS into the conventional SAFT algorithm is explained in section 2.4. A summary of this chapter is given in the final section.

2.1 Fundamental of ultrasonic testing

The term ultrasonic pertains to sound waves of a frequency greater than 20,000 Hz. In ultrasonic testing, the ultrasound is generated by a device called a transducer and such sound wave can be used on almost any materials to locate internal discontinuities ranging from cracks to disbonds. Vibrations of ultrasonic are generated by applying the electrical energy to a piezoelectric element cased inside a transducer. Such element transforms the electrical energy into mechanical energy i.e. the vibration of a frequency determined by the material and thickness of the element. On the contrary, the same element can also transform the mechanical energy of received vibration into electrical energy which can be displayed as a waveform on an oscilloscope.

Ultrasonic energy that is propagated by the vibration of particles in a material can be classified into various modes considering the direction in which the particles vibrate in relation to the propagation direction of the bulk ultrasonic beam. This dissertation utilize the two fundamental ultrasonic wave modes which are longitudinal and transverse wave modes, illustrated in **Figure 2.1**.

Longitudinal wave (also known as “compressional” or “pressure” or “p” waves) is a wave in which the particle motion of a material moves in essentially the same direction as the sound wave propagation. This wave mode is generated when a target of inspection is subjected to an incident wave with the angle of incidence near normal to the surface of a target. The wave velocity (c_L) of longitudinal wave is the highest compared to transverse and surface waves, and it is a determinate constant related to elastic modulus and density of a material. This wave mode is extensively used for thickness inspection, corrosion thinning, and for the detection of other defects parallel to the inspection surface.

Transverse wave (also known as “shear” or “s” waves) is a wave in which the particle motion is perpendicular to the direction of propagation. Transverse wave travels at a velocity (c_T) which is approximately half velocity of the longitudinal wave for the same material. Transverse wave can exist in any elastic solid, but is not supported by liquid or gas. Transverse wave is generated when a target of inspection is impinged on the surface by a longitudinal wave at an angle other than normal (90°) ranging from the first to the second critical angles. Some part of the wave is reflected while mode conversion and refraction occur in the other part, resulting in a longitudinal wave propagating at an angle in a target. Shear wave inspections are used extensively for crack and other defect where it is suspected to be located at other than parallel to the inspection surface.

Longitudinal wave mode will be shortly called as *L-mode* and transverse wave mode will be called as *T-mode* through this dissertation.

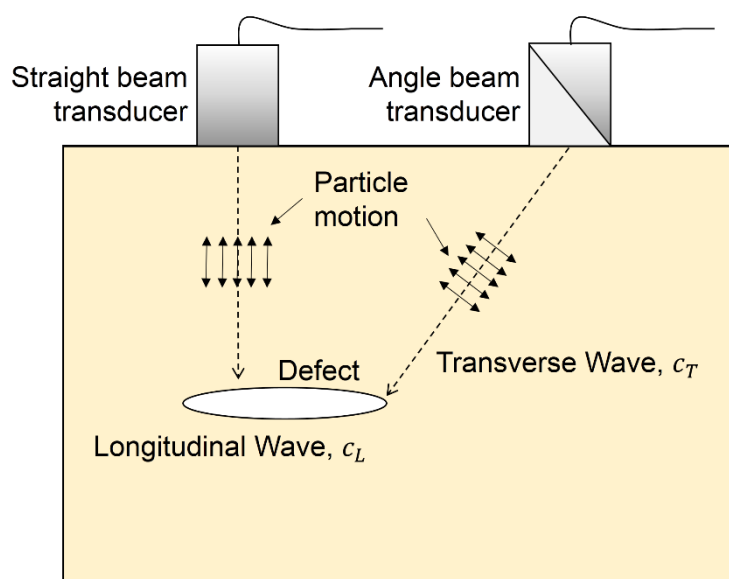


Figure 2.1 Longitudinal and transverse wave modes.

2.1.1 Refraction and mode conversion

When a longitudinal wave is impinged on the surface of a target in normal direction ($\theta = 0^\circ$), the longitudinal sound beam is transmitted straight into the target and no refraction occurs. However, when the incident angle is other than normal; refraction, reflection and mode conversion occur. Refraction is a change in propagation direction. Mode conversion is a change in the nature of the wave motion. A portion of the longitudinal incident beam is refracted into one or more wave modes traveling at various angle in the test piece. Wave refraction at the interface is defined by Snell's law given in **Equation 2.1**, and illustrated in **Figure 2.2**.

$$\frac{c_{L,1}}{\sin \theta_{L,1}} = \frac{c_{L,2}}{\sin \theta_{L,2}} = \frac{c_{T,2}}{\sin \theta_{T,2}} \quad (2.1)$$

$\theta_{L,1}$ represents angle of incidence of longitudinal wave propagating in the plastic wedge at the wave velocity of $c_{L,1}$, where $\theta_{L,2}$ and $\theta_{T,2}$ represent angles of refractions for longitudinal and transverse waves propagating in the target of inspection at the wave velocities of $c_{L,2}$ and $c_{T,2}$, respectively. Waves propagating in both solids can be either a longitudinal or transverse wave modes. However, in all experimental setup throughout this dissertation, transverse wave mode only exists in a target as a result from mode conversion.

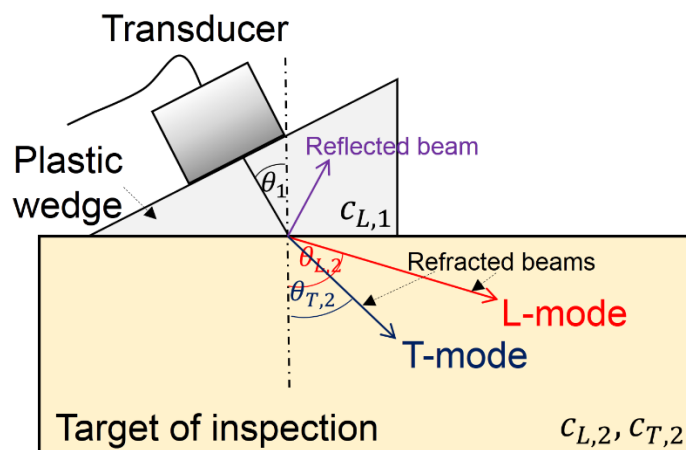


Figure 2.2 Wave refractions at the interface.

2.1.2 Test configurations in UT

In UT, there are two fundamental test configurations which are classified by the number of probe used in a single measurement. The one probe technique is called a “pulse-echo” configuration, and another technique using two probes is called a “pitch-catch” configuration.

Pulse-echo configuration is illustrated in **Figure 2.3** where the same transducer is used as both a transmitter and a receiver. First, a transducer is actuated by a signal sent from a pulser-receiver and transmits ultrasonic waves into a test medium. Then, its behavior is changed into a receiver to received echoes from ultrasonic waves propagated through a test medium. An example of received waveform signal is shown in **Figure 2.3**. At time t_2 , ultrasonic waves reflected at the bottom is received, hence a relatively high amplitude can be observed. This is normally called a bottom echo.

Pitch-catch configuration is illustrated in **Figure 2.4** where a transmitter and a receiver are provided, separately. Ultrasonic waves transmitted from a transmitter are scattered by any discontinuities in a test medium and received at a receiver. Considering an example waveform in **Figure 2.4**, at time t_2 , scattered ultrasonic waves are received at a receiver, thus a relatively high amplitude can be observed at time t_2 . This received signal is normally called a flaw echo.

Time t_2 , in **Figure 2.3** and **2.4** are travelled times of ultrasonic waves in test medium at specific propagation routes. In **Figure 2.3**, it is a bottom echo. In **Figure 2.4**, it is a flaw echo. These travelled times are called the *time-of-flights (TOFs)*.

TOF is used extensively in UT NDT since it can be used to locate the flaw by dividing the TOF by corresponding wave velocity in a test medium. However, wave propagation route is basically an unknown that inspectors and engineers need to predict. SAFT algorithm can be a remedy for this problem since it can stochastically predict the location of scatterer by using vast combinations of independent transducer position. Its principle is explained in **Section 2.2**.

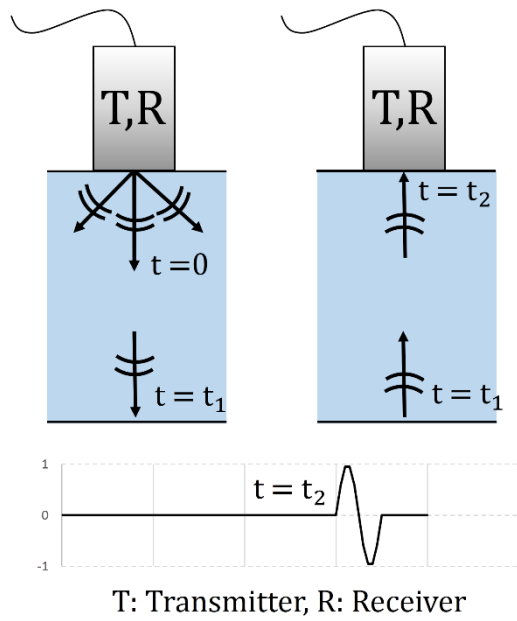


Figure 2.3 Pulse-echo test configuration.

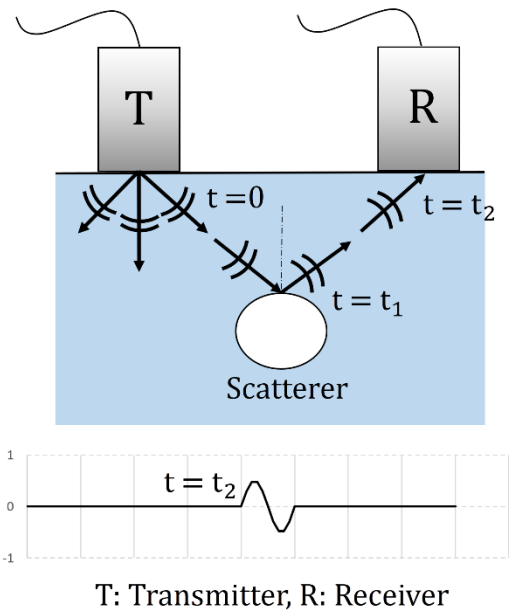


Figure 2.4 Pitch-catch test configuration.

2.1.3 Representation of UT result

Basically, there are three methods to present measured data in UT.

A-Scan presentation is a plot of time versus amplitude, in other words, is a raw waveform signal appeared on an oscilloscope. Horizontal axis normally indicates time and is used as a baseline. Any vertically deflected signals from the baseline indicates the amplitude of electrical pulses (sound echoes) received from the receiving transducer. Example of A-scan presentation and corresponding test configuration is shown in **Figure 2.5**. Vertically deflected signals observed at time $2t_1$ and $2t_2$ represent reflected ultrasonic waves from flaw and bottom surface, respectively.

B-Scan presentation provides a cross-sectional view of a test medium from a linear scan over the surface. Horizontal and vertical axes indicate distances in lateral and vertical directions, respectively. Considering **Figure 2.6**, an example of B-scan presentation is shown with a corresponding test configuration. Positions of a flaw and bottom surface of a test medium can be obtained from plotting the position where vertically deflected signals are observed in A-scan. However, the time axis in A-scan shall be divided by the wave velocity in a test medium to convert the measurement from time to position.

C-Scan presentation provides a plan view of the discontinuities in a test medium. This can be accomplished by collecting A-scan signals over the surface of a test medium with a manual or automated two-axis scanner. An example of C-scan presentation is shown in **Figure 2.7** with a corresponding test configuration. A transducer is moved over the surface of a test medium to collect A-scan signals. Then, vertically deflected signals in A-scan are plotted with some different intensities corresponding to different depths or thickness. Considering **Figure 2.7**, three colors are used to indicate signals reflected from different depths. Most of the scanned area is plotted by the third color (pink) which indicate the bottom surface of a test medium. Defects D1 and D2 are plotted with different colors, indicating that two defects are located in different depths.

At this stage, it can be noticed that basic data presentations in UT are quite difficult to interpret. Therefore, signal processing technique such as SAFT is invented to transform these incomprehensible result presentations into an easy to understand digital image.

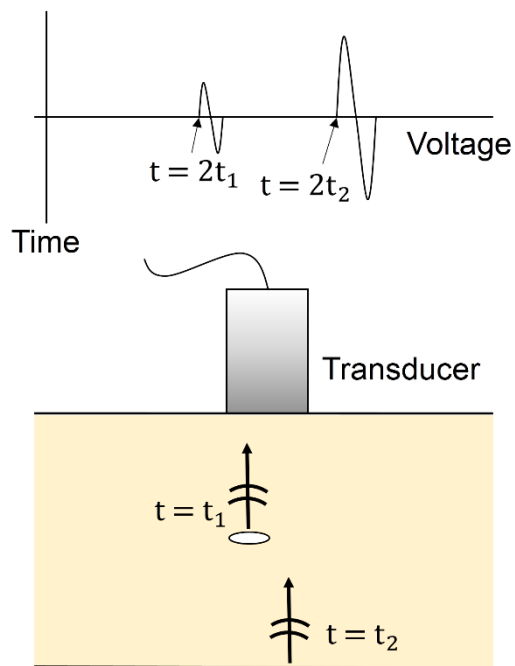


Figure 2.5 A-Scan presentation.

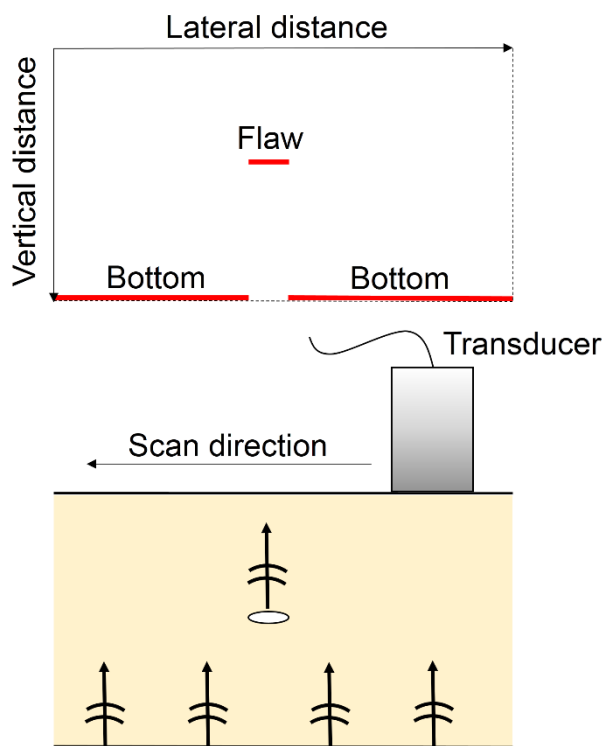


Figure 2.6 B-Scan presentation.

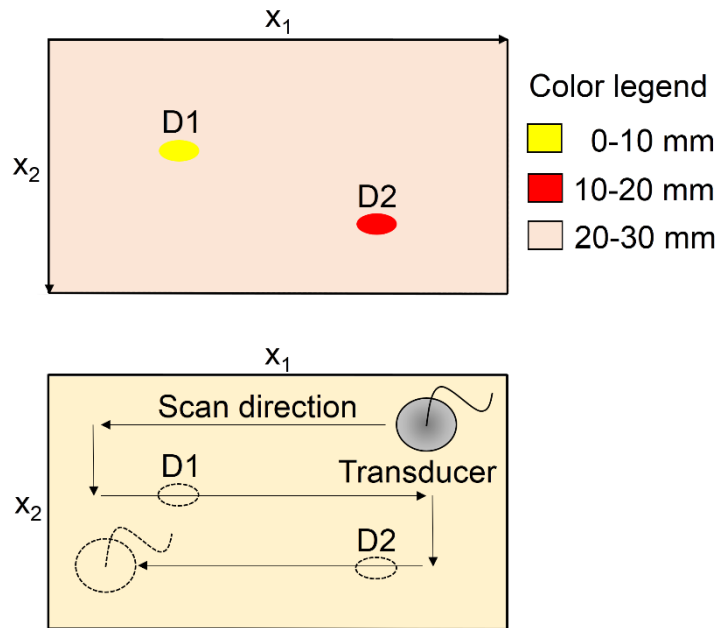


Figure 2.7 C-Scan presentation.

2.2 Principle of SAFT

SAFT is a TOF based signal processing technique that can be implemented in both 2-D and 3-D problems. However, this dissertation is dealing with targets of inspections containing cut through type defects. In other words, the cross sections of a target are similar, hence it can be considered as a 2-D problem. Therefore, this dissertation will only explain the principle of SAFT in 2-D. The same principle can also be applied to a 3-D problem. By applying the SAFT algorithm to the received A-scan waveform signals from every transmitter and receiver pair, A-scan signals are synthesized so strongly reflected echoes in an insonified test medium are refocused. Therefore, the location of scatterer can be identified. Comparison between B-scan and SAFT processed images are reported by Stepinski [26].

This section explains principle of SAFT, first in a single medium case, then followed by the extension of the same principle in two media case which is the one actually used throughout this dissertation.

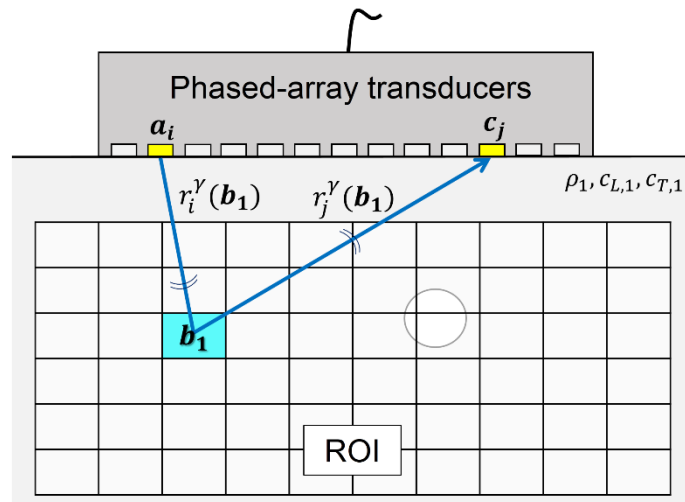
2.2.1 SAFT in a single medium case

This section explains the principle of SAFT in a single medium case which is a traditional usage of this technique. An outline of a single medium case is illustrated in **Figure 2.8(a)**. A phased-array transducer consisting of n number of piezoelectric elements (or channels) is placed over a medium of density ρ . Ultrasonic wave velocities in such medium are c_L and c_T for longitudinal and transverse wave modes, respectively. For simplicity, longitudinal wave mode is called as L-mode and transverse wave mode is called as T-mode throughout this dissertation. Designated area in a test medium where it is to be imaged is normally defined as a Region Of Interest (ROI) which is discretized into pixels similar to a production of a digital image [27]. Each pixel is represented by a spatial vector $\mathbf{b} = \{b_1, b_2\}$. Spatial resolution of a SAFT image can be arbitrarily selected by choosing the pixel width. The finer pixel produces a higher resolution image in substitute of much more computational time.

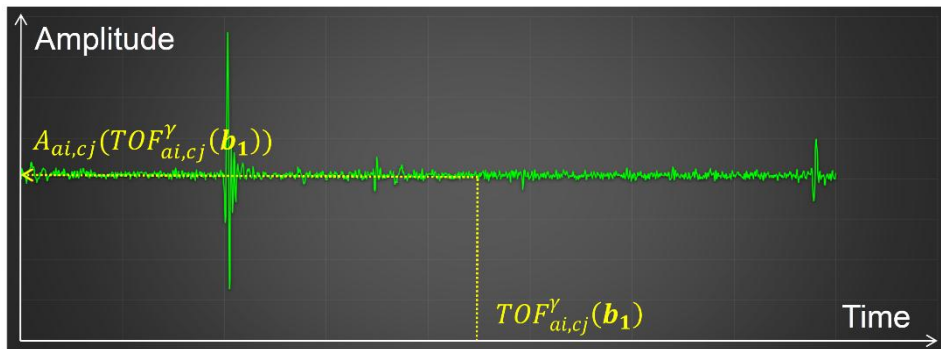
$TOF_{ai,cj}^\gamma(\mathbf{b})$ of a specific wave propagating route to an arbitrary pixel governed by the positions of a transmitter ($\mathbf{a}_i = \{a_1, a_2\}$) and a receiver ($\mathbf{c}_j = \{c_1, c_2\}$) and a wave velocity of mode γ , can be computed as shown in **Equation 2.2**

$$TOF_{ai,cj}^\gamma(\mathbf{b}) = \frac{r_i^\gamma(\mathbf{b}) + r_j^\gamma(\mathbf{b})}{c_\gamma}, \quad (2.2)$$

where $r_i^\gamma(\mathbf{b})$ represents wave propagation distance from \mathbf{a}_i to \mathbf{b} , and $r_j^\gamma(\mathbf{b})$ represents wave propagation distance from \mathbf{b} to \mathbf{c}_j . The subscripts i and j are used to represent channels of a phased-array transducer which are used to transmit and receive the ultrasonic wave, respectively. Another subscript γ represents a wave mode: $\gamma = L$ for L-mode and $\gamma = T$ for T-mode. Either mode must be selected as a configuration for SAFT imaging. SAFT assumes that there may be a scatterer in any points \mathbf{b} in the ROI, hence the calculation must be performed on every point \mathbf{b} . Considering **Figure 2.8(a)**, pixel \mathbf{b}_1 contain no ultrasonic wave scatterer, such as a side-drilled hole (SDH). Therefore, there will be no significant echo detected at such TOF, $TOF_{ai,cj}^\gamma(\mathbf{b}_1)$ in an A-scan signal. **Figure 2.8(b)** illustrates the process of acquiring corresponding amplitude value from an A-scan signal. In this case, since there is no flaw echoes from a scatterer, $A_{ai,cj}(TOF_{ai,cj}^\gamma(\mathbf{b}_1))$ will acquire an amplitude of the noises.



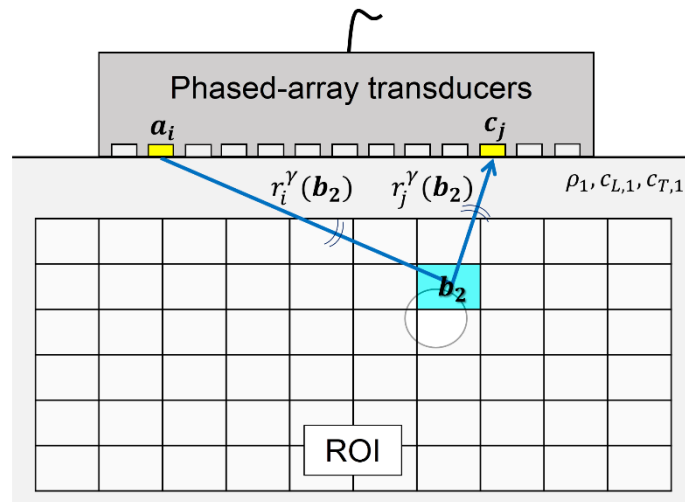
(a)



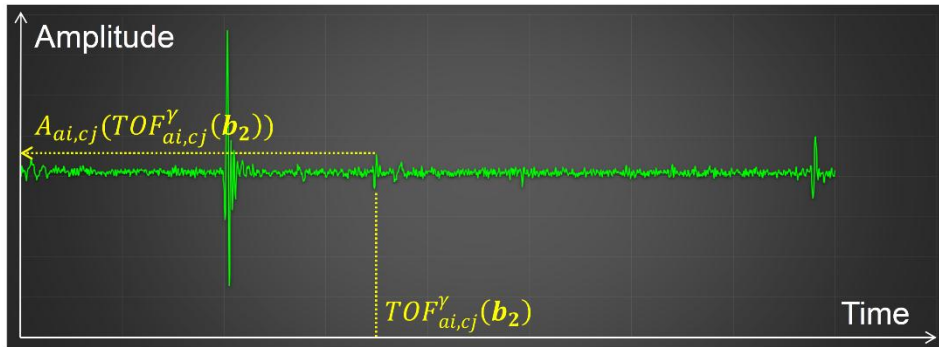
(b)

Figure 2.8 SAFT computation at a non-defect part in a single medium case;
(a) Outline and (b) Waveform.

In **Figure 2.9(a)**, a pixel \mathbf{b}_2 contain a part of an SDH which acts as a scatterer for the ultrasonic wave. Therefore, ultrasonic wave transmitted from a transmitter \mathbf{a}_i , scattered at \mathbf{b}_2 shall be received at a receiver \mathbf{c}_j at a travelled time of $TOF_{ai,cj}^y(\mathbf{b}_2)$. Therefore, $A_{ai,cj}(TOF_{ai,cj}^y(\mathbf{b}_2))$ should acquire a relatively large amplitude value from the ultrasonic wave scattered at the curved boundary of an SDH as shown in **Figure 2.9(b)**.



(a)



(b)

Figure 2.9 SAFT computation at a defect in a single medium case;
(a) Outline and (b) Waveform.

Pixel value $A_{ai,cj}(TOF_{ai,cj}^y(\mathbf{b}))$ is computed using the same process for every pixels in ROI. At this stage, it can be noticed that pixel value $A_{ai,cj}(TOF_{ai,cj}^y(\mathbf{b}))$ is a function of time $TOF_{ai,cj}^y(\mathbf{b})$ only, hence acquired pixel values will be similar for the same transducer pair on every pixel with the similar $TOF_{ai,cj}^y(\mathbf{b})$. Therefore, a SAFT image using only one transducer pair has no meaning since we cannot identify the location of scatterer on the hyperbolic curve of the pixels with similar $TOF_{ai,cj}^y(\mathbf{b})$ where the pixel values are plotted with similar intensities. This is the reason why it is required to have a summation of pixel values from as much combination of transducer pair as possible and this is the reason why this technique is called a Synthesis Aperture Focusing Technique. Synthesizing the A-scan signals from more apertures will result in higher resolution of ultrasound image. However, without synthesizing a number of A-scan signals from independent transducer positions, resulting image may be poor or

meaningless as mentioned above. Using pixel value calculated from **Equation 2.2**, summation is performed on every pixel in ROI as shown in **Equation 2.3**

$$S^\gamma(\mathbf{b}) = \sum_i \sum_j |A_{ai,cj}(TOF_{ai,cj}^\gamma(\mathbf{b}))| \quad (2.3)$$

where i and j are numbers of piezoelectric transducer elements used as a transmitter and a receiver, respectively. The location of a scatterer can be found by superposing of $|A_{ai,cj}(TOF_{ai,cj}^\gamma(\mathbf{b}))|$ from all available transducer pair since high amplitudes from scatterer are repeatedly plotted at the same point \mathbf{b} . Therefore, plotting $S^\gamma(\mathbf{b})$ of every point \mathbf{b} in ROI will result in a SAFT image. Absolute value is used here since phase information is not accounted.

2.2.2 SAFT in a two media case

SAFT has traditionally been applied for a single medium ultrasound imaging. However, some recent researches have shown potentials of SAFT imaging in multilayered mediums. Skjelvareid et al. developed a SAFT imaging for three layered mediums by using an Omega-K algorithm [28]. Shih et al. used a Root-Mean-Square velocity to improve complicated and time-consuming delay time computation of SAFT imaging for two media problem [29]. The only difference between a single medium and two media cases is that it is required to determine a refraction point at the interface of two media according to Snell's laws in order to calculate a TOF of a wave propagation inside two media.

Outline of SAFT for two media case is shown in **Figure 2.10**. A phased-array transducers is placed over a specimen with two media. Medium 1 has a density of ρ_1 and ultrasonic wave velocities of $c_{L,1}$ and $c_{T,1}$ for L- and T-modes, respectively. Medium 2 has a density of ρ_2 and ultrasonic wave velocities of $c_{L,2}$ and $c_{T,2}$ for L-mode and T-mode, respectively. Considering **Figure 2.10**, ultrasonic wave from a transmitter at $(\mathbf{a}_i = \{a_1, a_2\})$, refracted at point of refraction $\mathbf{x}_i = \{x_{i,1}, x_{i,2}\}$ on the interface between two media and propagated to an arbitrary pixel $(\mathbf{b} = \{b_1, b_2\})$ inside the ROI, is called a transmitting route indicated by the subscript i which also indicates a transducer number which is used as a transmitter. On the other hand, ultrasonic wave scattered at point \mathbf{b} , refracted at refraction point $\mathbf{x}_j = \{x_{j,1}, x_{j,2}\}$ on the interface between two media and received at a receiver $(\mathbf{c}_j = \{c_1, c_2\})$ is called a receiving route

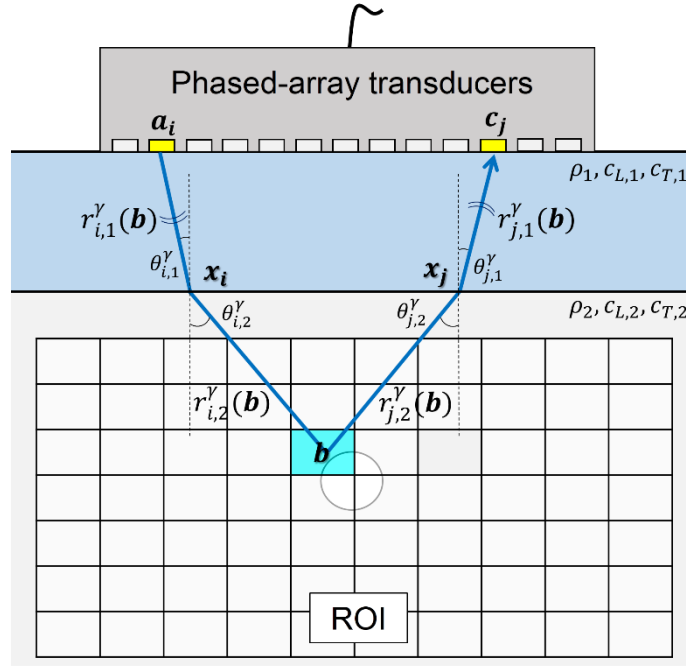


Figure 2.10 Outline for SAFT in a two media case.

indicated by a subscript j that also represents a transducer number used as a receiver. TOF which is used to get corresponding amplitude data from received waveform data can be calculated from dividing the distance, ultrasonic wave travelled from point \mathbf{a}_i scattered at \mathbf{b} and received at \mathbf{c}_j by wave velocities in each medium.

For transmitting route, refraction point \mathbf{x}_i satisfying Snell's laws shown in **Equation 2.4** is required to be solved for any \mathbf{a}_i and \mathbf{b} to get propagated distance $r_{i,1}^\gamma$ and $r_{i,2}^\gamma$ in first and second medium, respectively.

$$\frac{\sin \theta_{i,1}^L}{c_{L,1}} = \frac{\sin \theta_{i,1}^T}{c_{T,1}} = \frac{\sin \theta_{i,2}^L}{c_{L,2}} = \frac{\sin \theta_{i,2}^T}{c_{T,2}}. \quad (2.4)$$

$\theta_{\gamma,\delta}$ is an angle of incidence or angle of refraction on the interface between two media. The subscripts γ and δ indicate medium and wave mode, respectively. The newly introduced subscript $\delta = 1$ for first medium and $\delta = 2$ for second medium. Be noted that if first medium is fluid, there will be no T-mode exists in the first medium. $C_{\gamma,\delta}$ is a wave velocity of wave mode γ in medium δ . In this dissertation, refraction points are determined numerically by bisection method (with admissible error of 10^{-3} mm) on

assumption that refraction points shall locate in between any \mathbf{a}_i and \mathbf{b} in a transmitting route, and any \mathbf{b} and \mathbf{c}_j in a receiving route. After refraction point has been determined, propagated distance can be simply calculated using the Cartesian coordinates of three points. For a receiving route, calculation for $r_{j,1}^\gamma$ and $r_{j,2}^\gamma$ can be calculated in the same manner. Then, $TOF_{ai,cj}^\gamma(\mathbf{b})$ of an arbitrary pixel \mathbf{b} from an independent transducer pair, a transmitter at \mathbf{a}_i and a receiver at \mathbf{c}_j , can be calculated using **Equation 2.5** with its corresponding wave speed for a chosen wave mode γ .

$$TOF_{ai,cj}^\gamma(\mathbf{b}) = \frac{r_{i,1}^\gamma + r_{j,1}^\gamma}{c_{\gamma,1}} + \frac{r_{i,2}^\gamma + r_{j,2}^\gamma}{c_{\gamma,2}} \quad (2.5)$$

After TOF is calculated, the second step is to sum pixel value from all available combinations of transmitter and receiver which is similar to a single medium case. Corresponding amplitude value from a transmitter \mathbf{a}_i and a receiver \mathbf{c}_j from received A-scan signal is acquired and stored as pixel value of \mathbf{b} , $A_{ai,cj}(TOF_{ai,cj}^\gamma(\mathbf{b}))$. Finally, a summation in **Equation 2.3** is performed on every pixel \mathbf{b} in ROI and plotting the $S^\gamma(\mathbf{b})$ of every pixel in ROI will result in a SAFT image.

2.3 Modelling of ultrasonic beam radiation by the Approximate Wave Solution (AWS)

Ultrasonic beam radiation can be modelled by various methods [30-32]. This dissertation models the ultrasonic beam radiation from a spatial displacement in a test medium, induced by the ultrasonic wave transmitted from a planar type transducer when striking at the interface between two media. Such displacement can be approximated by various solutions such as Kirchhoff Beam Transmission (KBT) model which is applicable to a wide range of general geometries. However, drawback of a KBT model is that it requires the numerical evaluation of double surface integration over the surface of transducer and interface between two media.

Schmerr et al. used the stationary phase approximation to evaluate the integrations over the interface of two media and simplified this problem into a simpler model called a Surface Integral (SI) model which only require one 2-D surface integral [24]. The drawback of this SI model is that it will fail if caustics in the wave field, usually observed in focusing type transducer, are present. However, this problem can be negligible in this dissertation since a planar type transducer is used. Main purpose of this dissertation is to

implement approximate ultrasonic beam radiation into the SAFT algorithm, thus optimization between accuracy and speed in computation must be made. The SI model using a method of stationary phase is selected since it consumes less computational time than a KBT model. The SI model will be called Approximate Wave Solution abbreviated as AWS throughout this dissertation.

This section is divided into four sub-sections. Section 2.3.1 explains the AWS of fluid-solid two phase media with curved interface, which is applied to the water immersion tests of rod specimens in chapter 3. Then, the AWS of two solids media with planar interface, which is applied to the angle beam tests in chapter 4, is explained in sub-section 2.3.2. Experimental verification of AWS is reported in section 2.3.3.

2.3.1 AWS of fluid-solid two phase media with curved interface

A detail on the derivation of the AWS for fluid-solid curved interface can be followed in [24]. This dissertation shows only the final form of equations which are actually implemented into the SAFT algorithm. Considering **Figure 2.11**, an outline of water immersion test is illustrated using the same mathematical expressions as in explanation of SAFT in section 2.2. Magnitude of the spatial displacement $u_i^\gamma(\mathbf{b}, \omega)$ of point \mathbf{b} at a circular frequency ω of a wave mode γ when the ultrasonic wave transmitted from a transducer at \mathbf{a}_i strikes the interface can be represented as shown in **Equation 2.6**,

$$u_i^\gamma(\mathbf{b}, \omega) = \frac{-p_0}{2\pi\rho_2 c_{L,1} c_{\gamma,2}} \int_{S_{T,ai}} \frac{T_{12}^{\gamma;L} \exp(ik_{L,1}r_{i,1}^\gamma + ik_{\gamma,2}r_{i,2}^\gamma + i\sigma^\gamma)}{r_{i,1}^\gamma r_{i,2}^\gamma \sqrt{|\Phi_{p1}^\gamma| |\Phi_{p2}^\gamma|}} dS(\mathbf{a}_i) \quad (2.6)$$

where ρ_δ is the density of media phase δ ($\delta = 1,2$), p_0 is a uniform pressure acting over the transducer surface and $S_{T,ai}$ represents the surface of a transducer at point \mathbf{a}_i . $c_{\gamma,2}$ is a wave velocity of mode γ ($\gamma = L, T$) in media phase 2. $k_{\gamma,\delta}$ is a wave number of wave mode γ in media phase δ , ω is an angular frequency and $i = \sqrt{-1}$. $T_{12}^{\gamma;L}$ is a transmission coefficient of ultrasonic wave propagating from medium phase 1 to 2 of the wave mode γ in medium 2 and can be computed using **Equation 2.7** and **Equation 2.8** for L- and T-modes, respectively, where Δ is defined in **Equation 2.9** [33].

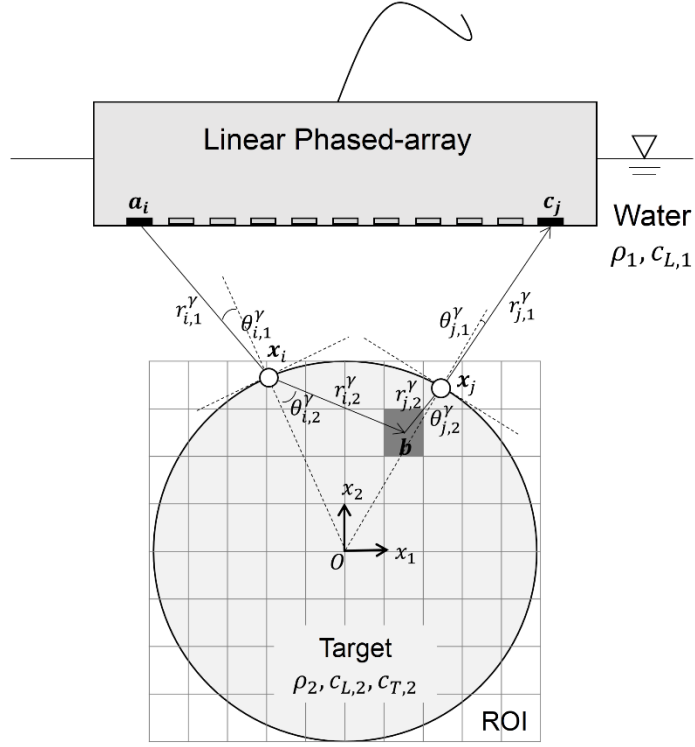


Figure 2.11 Outline of water immersion test.

$$T_{12}^{L;L} = \frac{2 \cos \theta_{i,1}^L [1 - 2(\sin \theta_{i,2}^T)^2]}{\cos \theta_{i,1}^L + \frac{\rho_2 c_{L,2}}{\rho_1 c_{L,1}} \cos \theta_{i,1}^L \Delta} \quad (2.7)$$

$$T_{12}^{T;L} = \frac{-4 \cos \theta_{i,1}^L \cos \theta_{i,2}^L \sin \theta_{i,2}^T}{\cos \theta_{i,2}^L + \frac{\rho_2 c_{L,2}}{\rho_1 c_{L,1}} \cos \theta_{i,1}^L \Delta} \quad (2.8)$$

$$\Delta = \left[4 \left(\frac{c_{T,2}}{c_{L,2}} \right)^2 \sin \theta_{i,2}^T \cos \theta_{i,2}^T \sin \theta_{i,2}^L \cos \theta_{i,2}^L + 1 - 4(\sin \theta_{i,2}^T \cos \theta_{i,2}^T)^2 \right] \quad (2.9)$$

ϕ_{p1}^y, ϕ_{p2}^y in **Equation 2.6** are given by **Equations 2.10** and **2.11**.

$$\phi_{p1}^y = \frac{\phi_{11}^y + \phi_{22}^y}{2} + \frac{1}{2} \sqrt{(\phi_{11}^y - \phi_{22}^y)^2 + 4(\phi_{12}^y)^2} \quad (2.10)$$

$$\phi_{p2}^y = \frac{\phi_{11}^y + \phi_{22}^y}{2} - \frac{1}{2} \sqrt{(\phi_{11}^y - \phi_{22}^y)^2 + 4(\phi_{12}^y)^2} \quad (2.11)$$

ϕ_{11}^γ , ϕ_{12}^γ and ϕ_{22}^γ are given by **Equations 2.12-2.14**.

$$\phi_{11}^\gamma = \frac{1}{r_{i,2}^\gamma} + \frac{c_{\gamma,2} \cos^2 \theta_{i,1}^L}{c_{L,1} \cos^2 \theta_{i,2}^\gamma} \frac{1}{r_{i,1}^\gamma} - \frac{(c_{\gamma,2} \cos \theta_{i,1}^L / c_{L,1} - \cos \theta_{i,2}^\gamma)}{R_I \cos^2 \theta_{i,2}^\gamma} \quad (2.12)$$

$$\phi_{12}^\gamma = \phi_{21}^\gamma = \frac{(c_{\gamma,2} \cos \theta_{i,1}^L / c_{L,1} - \cos \theta_{i,2}^\gamma)}{R_{I0} \cos^2 \theta_{i,2}^\gamma} \quad (2.13)$$

$$\phi_{22}^\gamma = \frac{1}{r_{i,2}^\gamma} + \frac{c_{\gamma,2}}{c_{L,1}} \frac{1}{r_{i,1}^\gamma} - \frac{\left(\frac{c_{\gamma,2} \cos \theta_{i,1}^L}{c_{L,1}} - \cos \theta_{i,1}^L \right)}{R_0}, \quad (2.14)$$

Where curvature terms R_I, R_{I0}, R_0 are assumed to be infinitely large. Phase change term σ^γ in **Equation 2.6** is given by **Equation 2.15**, and $\text{sgn } \phi_{p1}^\gamma$ and $\text{sgn } \phi_{p2}^\gamma$ are signum functions of ϕ_{p1}^γ and ϕ_{p2}^γ .

$$\sigma^\gamma = \frac{\pi}{4} (\text{sgn } \phi_{p1}^\gamma + \text{sgn } \phi_{p2}^\gamma) \quad (2.15)$$

For the receiving process from the point \mathbf{b} to the receiver \mathbf{c}_j , AWS is used in the same manner as in the transmitting route, but the transmission coefficient $T_{12}^{\gamma;L}$ was changed to $T_{21}^{L;\gamma}$ which can be calculated by **Equation 2.16**.

$$T_{21}^{L;\gamma} = \frac{\rho_1 c_{L,1} \cos \theta_{i,2}^\gamma}{\rho_2 c_{\gamma,2} \cos \theta_{i,1}^L} T_{12}^{\gamma;L}. \quad (2.16)$$

Therefore, AWS for the receiving route is obtained as shown in **Equation 2.17**

$$u_j^\gamma(\mathbf{b}, \omega) = \frac{-p_0}{2\pi \rho_2 c_{L,1} c_{\gamma,2}} \int_{S_{T,cj}} \frac{T_{21}^{L;\gamma} d_n^\gamma \exp(ik_{L,1} r_{j,1}^\gamma + ik_{\gamma,2} r_{j,2}^\gamma + i\sigma^\gamma)}{r_{j,1}^\gamma r_{j,2}^\gamma \sqrt{|\phi_{p1}^\gamma| |\phi_{p2}^\gamma|}} dS(\mathbf{c}_j). \quad (2.17)$$

Examples of ultrasonic beam radiation model using the AWS are shown in **Figure 2.12** and **2.13**, in case of $\gamma = L$ and T , respectively. Frequency is 5 MHz, $p_0 = 1$ MPa and material properties are shown in **Table 2.1**. First medium is Water and second medium is an Aluminum. Element numbers of transducers used in these examples are Ch.16 and 32. Element size is 0.4 mm×12.0 mm with 0.5 mm pitch between adjacent elements.

Ultrasonic beam radiation of second phase medium in T- and L-modes for any transducer positions can be approximated using **Equation 2.6**. Considering **Figure 2.12**, AWS beam radiation model in L-mode shows that ultrasonic wave from both transducers strongly propagated in the direction normal to the nearest interfaces, or the tangential line of closest surface of aluminum rod specimen.

Considering **Figure 2.13**, T-mode AWS beam radiation models are show. In this case, ultrasonic wave from both transducers strongly propagated in $\pm 45^\circ$ directions from the normal of the nearest interfaces, or the tangential line of closest surface of an aluminum rod specimen. Implementing these beam radiation models into SAFT will amplify pixel value in direction where ultrasonic wave strongly propagates for each mode. On the other hand, it will suppress the SAFT imaging values at the pixels where ultrasonic amplitudes are weak.

Material	Density (Kg/m ³)	c_L (m/s)	c_T (m/s)
Water	1000	1470	-
Aluminum	2700	6300	3130

Table 2.1 Material properties used in water immersion test.

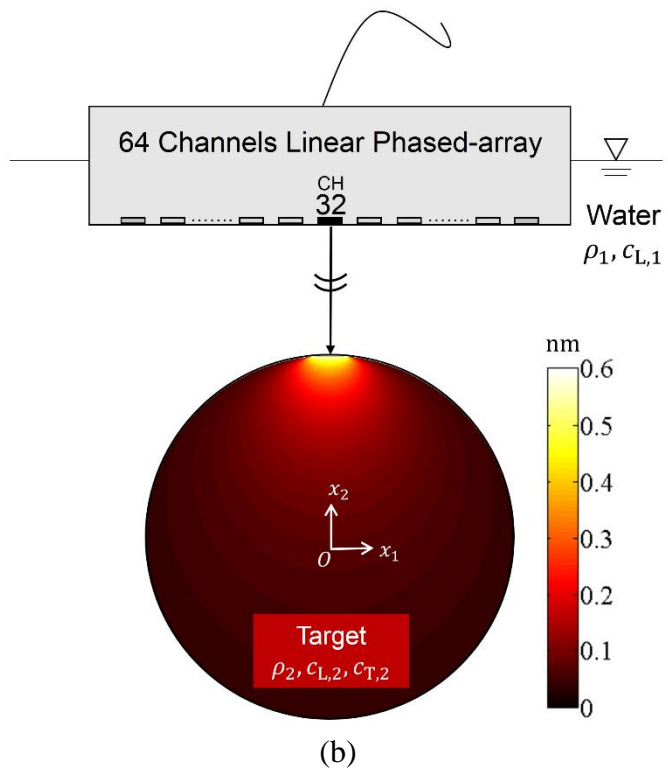
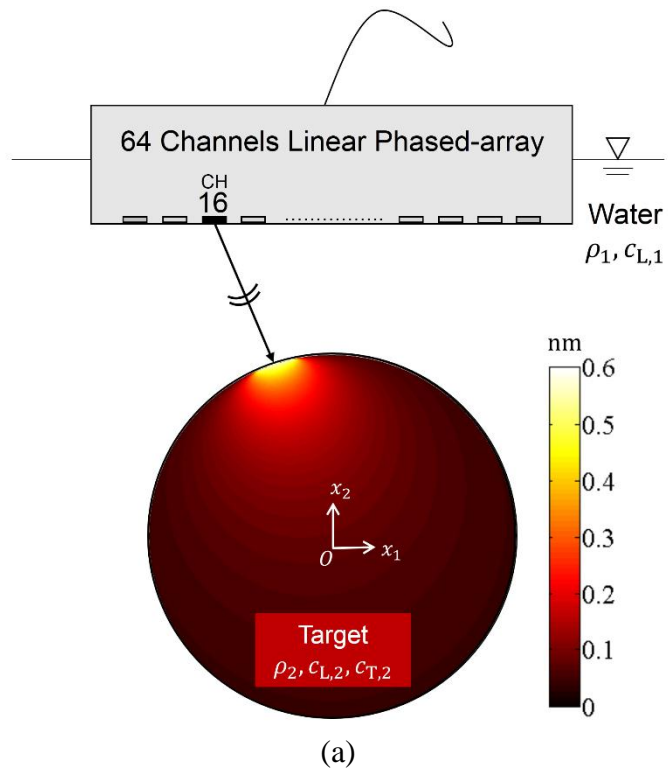
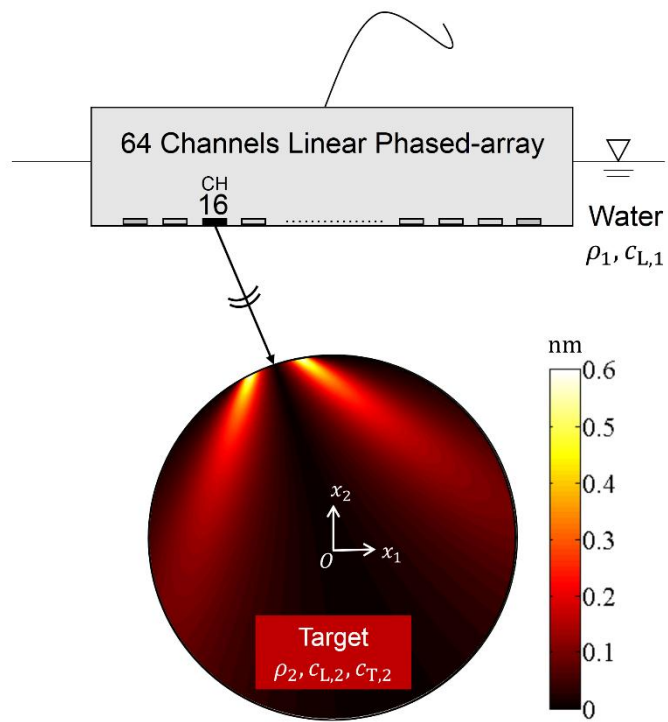
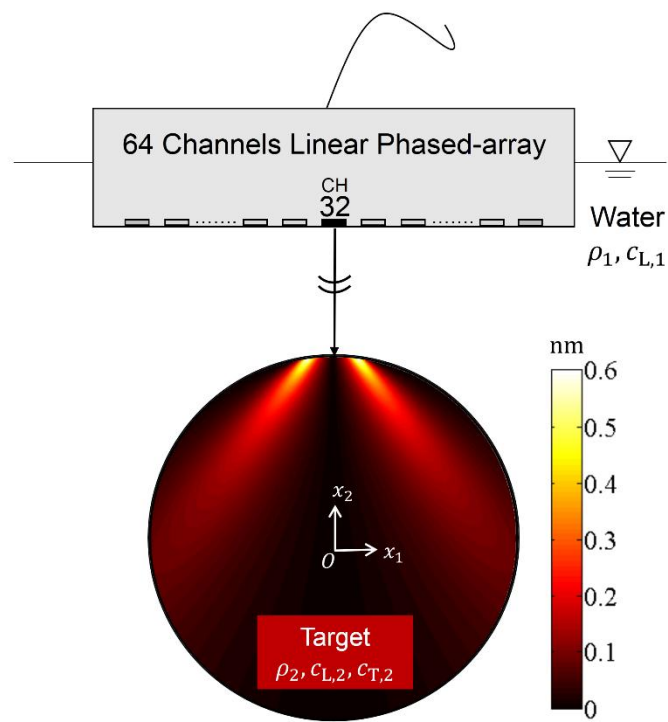


Figure 2.12 L-mode beam radiation; (a) Ch.16 and (b) Ch.32.



(a)



(b)

Figure 2.13 T-mode beam radiation models; (a) Ch.16 and (b) ch.32.

2.3.2 AWS of two solids media with planar interface

Outline of angle beam test is shown in **Figure 2.7** using the same mathematical expressions as in the explanation of SAFT in section 2.2. Detail on the derivation of AWS for solid-solid two layered medium with planar interface can also be found in [24]. Magnitude of the spatial displacement $u_i^\gamma(\mathbf{b}, \omega)$ of point \mathbf{b} at a circular frequency ω of a wave mode γ when the ultrasonic wave transmitted from a transducer channel i strikes the interface of two solids can be represented as shown in **Equation 2.18**.

$$u_i^\gamma(\mathbf{b}, \omega) = \frac{p_0}{2\pi\rho_1 c_{L,1}^2} \int_{S_{T,ai}} \frac{K_\gamma(\theta_1^{\gamma,L}) T_{12}^{\gamma,L} \exp(ik_{L,1}r_{i,1}^\gamma + ik_{\gamma,2}r_{i,2}^\gamma)}{\sqrt{\Delta_x^{\gamma,L}} \sqrt{\Delta_y^{\gamma,L}}} dS(a_i) \quad (2.18)$$

where p_0 is a pressure acting on the transducer surface $S_{T,ai}$, ρ_δ is a density of media phase δ , $k_{\gamma,\delta}$ represents the wave number of wave mode γ in solid δ and $i = \sqrt{-1}$. Directivity function $K_L(\theta_1^{\gamma,L})$ can be computed from **Equation 2.19** and **Equation 2.20** for L- and T-modes, respectively.

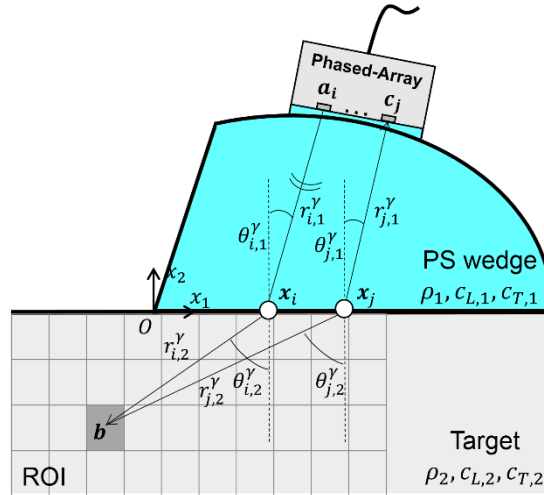


Figure 2.14 Outline of angle beam test.

$$K_L(\theta_{i,1}^L) = \frac{\cos \theta_{i,1}^L \kappa_1^2 (\kappa_1^2/2 - \sin^2(\theta_{i,1}^L))}{2G(\sin \theta_{i,1}^L)}, \quad (2.19)$$

$$K_T(\theta_{i,1}^L) = \frac{\kappa_1^3 \cos \theta_{i,1}^L \sin \theta_{i,1}^L \sqrt{1 - \kappa_1^2 \sin^2(\theta_{i,1}^L)}}{2G(\kappa_1 \sin \theta_{i,1}^L)} \quad (2.20)$$

where $\kappa_1 = c_{L,1}/c_{T,1}$. $G(x)$ is the function written as follows:

$$G(x) = (x^2 - \kappa_1^2/2)^2 + x^2 \sqrt{1 - x^2} \sqrt{\kappa_1^2 - x^2}. \quad (2.21)$$

Considering **Equation 2.18**, $T_{12}^{\gamma;L}$ is a transmission coefficient of ultrasonic wave propagating from solid 1 to 2 of the wave mode γ in solid 2 which can be calculated using **Equation 2.22** and **2.23** for L- and T-modes, respectively.

$$T_{12}^{L;L} = \frac{2 \cos \theta_{i,1}^L (1 - 2\sin^2 \theta_{i,1}^T) (1 - 2\sin^2 \theta_{i,2}^T)}{\Delta_1 + \Delta_2} \quad (2.22)$$

$$T_{12}^{T;L} = \frac{-4 \sin \theta_{i,2}^T \cos \theta_{i,1}^L \cos \theta_{i,2}^L (1 - 2\sin^2 \theta_{i,2}^T)}{\Delta_1 + \Delta_2}, \quad (2.23)$$

where Δ_1 and Δ_2 are defined in **Equation 2.24** and **2.25** [33].

$$\Delta_1 = \cos \theta_{i,2}^L \left[1 - 4\sin^2 \theta_{i,1}^T \cos^2 \theta_{i,2}^T + 4 \frac{c_{T,1}^2}{c_{L,1}^2} \sin \theta_{i,1}^T \cos \theta_{i,1}^T \sin \theta_{i,1}^L \cos \theta_{i,1}^L \right], \quad (2.24)$$

$$\Delta_2 = \frac{\rho_2 c_{L,2}}{\rho_1 c_{L,1}} \cos \theta_{i,1}^L \left[1 - 4\sin^2 \theta_{i,2}^T \cos^2 \theta_{i,2}^T + 4 \frac{c_{T,2}^2}{c_{L,2}^2} \sin \theta_{i,2}^T \cos \theta_{i,2}^T \sin \theta_{i,2}^L \cos \theta_{i,2}^L \right]. \quad (2.25)$$

Phase terms $\Delta_x^{\gamma;L}$ and $\Delta_y^{\gamma;L}$ in **Equation 2.18**, which are derived from a stationary phase method, are given by **Equation 2.26** and **2.27**, respectively.

$$\Delta_x^{\gamma;L} = r_{i,1}^\gamma + \frac{c_{\gamma,2} \cos^2 \theta_{i,1}^\gamma}{c_{L,1} \cos^2 \theta_{i,2}^\gamma} r_{i,2}^\gamma, \quad (2.26)$$

$$\Delta_y^{\gamma;L} = r_{i,1}^\gamma + \frac{c_{\gamma,2}}{c_{L,1}} r_{i,2}^\gamma \quad (2.27)$$

Considering a receiving route, AWS is described in the same manner as a transmitting

route but transmission coefficient $T_{12}^{\gamma;L}$ must be changed to $T_{21}^{L;\gamma}$ which can be calculated using **Equation 2.16**. AWS for receiving route shown in **Figure 2.14** can be written as **Equation 2.28**.

$$u_j^\gamma(\mathbf{b}, \omega) = \frac{p_0}{2\pi\rho_1 c_{L,1}^2} \int_{S_{T,cj}} \frac{K_L(\theta_1^{\gamma,L}) T_{21}^{L;\gamma} \exp(ik_{L,1}r_{j,1}^\gamma + ik_{\gamma,2}r_{j,2}^\gamma)}{\sqrt{\Delta_x^{\gamma;L}} \sqrt{\Delta_y^{\gamma;L}}} dS(c_j). \quad (2.28)$$

Using **Equation 2.18**, displacement $u_i^\gamma(\mathbf{b}, \omega)$ when the ultrasonic wave transmitted from an i -th transducer of wave mode γ strike the interface of two solids can be computed, and its magnitude is used to model the ultrasonic beam radiation. Examples of AWS beam radiation model will be shown using a central frequency of 5 MHz, $p_0 = 1$ MPa and materials properties as shown in **Table 2.2** where first solid medium is Polystyrene (PS) and second solid medium is Steel. An element number of the transducer used in these examples is Ch.16 located near the center of a phased-array transducer. The element size is 0.4 mm×12.0 mm with 0.5 mm pitch between adjacent elements.

Material	Density (Kg/m ³)	c_L (m/s)	c_T (m/s)
PS	1000	2320	1153
Steel	7800	5940	3233

Table 2.2 Material properties used in angle beam test.

Ultrasonic beam radiation models using AWS are shown in **Figure 2.15** and **2.16** for L- and T-modes, respectively. Angle θ_{PA} represents an angle between surfaces of a transducer and the second solid, or the line of interface. **Figure 2.15(a)** shows L-mode beam radiation in case of $\theta_{PA} = 0^\circ$ and **Figure 2.15(b)** shows the case of $\theta_{PA} = 16^\circ$. The Unit of displacements are in nanometer(nm). Both AWS beam radiations show that ultrasonic wave in L-mode strongly propagated in the normal direction to the interface between two solids. When angle θ_{PA} is rotated to 16° , transducer no.16 moved to the right, thus strong beam radiation region also shifted to the right.

Figure 2.16(a) shows the T-mode beam radiation in case of $\theta_{PA} = 0^\circ$ and **Figure 2.16(b)** shows the case of $\theta_{PA} = 16^\circ$. In these cases, strong beam radiation regions were observed in approximately $\pm 45^\circ$ directions from the normal of the closest interface. When angle θ_{PA} is rotated to 16° , transducer no.16 moved to the right, thus strong beam radiation region also shifted to the right, however, the high intensity region became wider. Implementing these beam radiation models into SAFT will amplify pixel value $|A_{ai,cj}(TOF_{ai,cj}^\gamma(\mathbf{b}))|$ in the regions where ultrasonic wave strongly propagates while also suppress the opposite. Implementation method of AWS into conventional SAFT will be explained in next section.

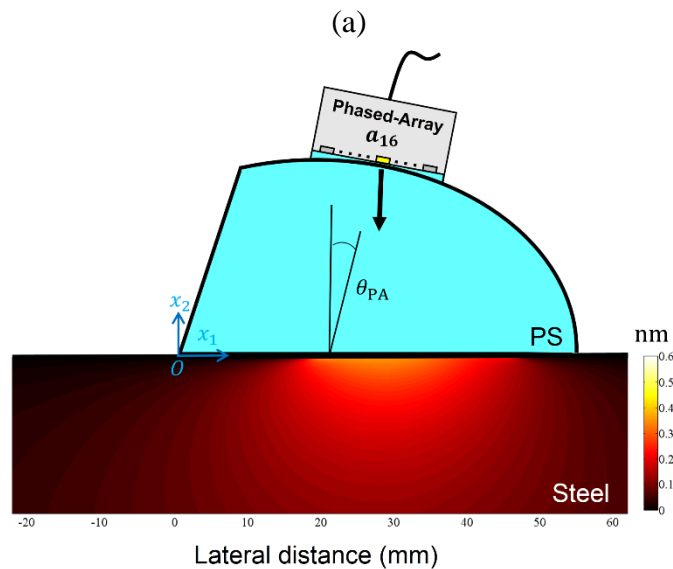
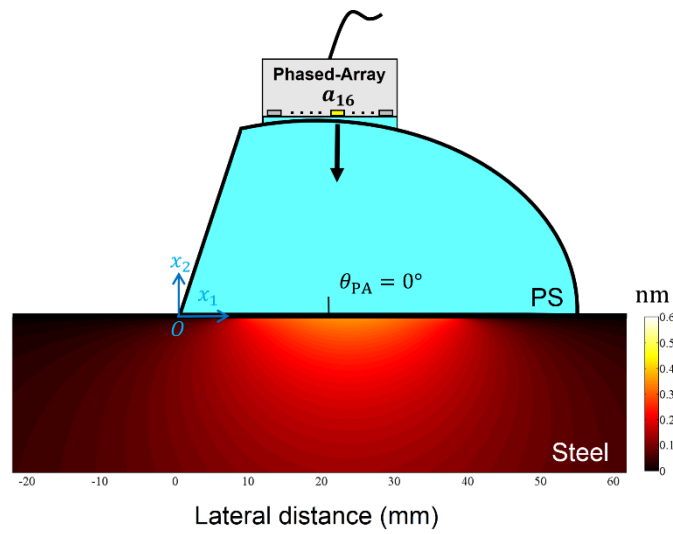
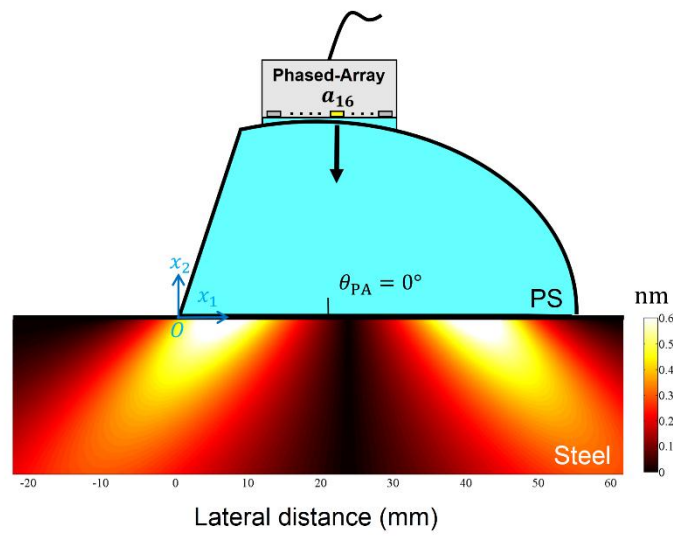
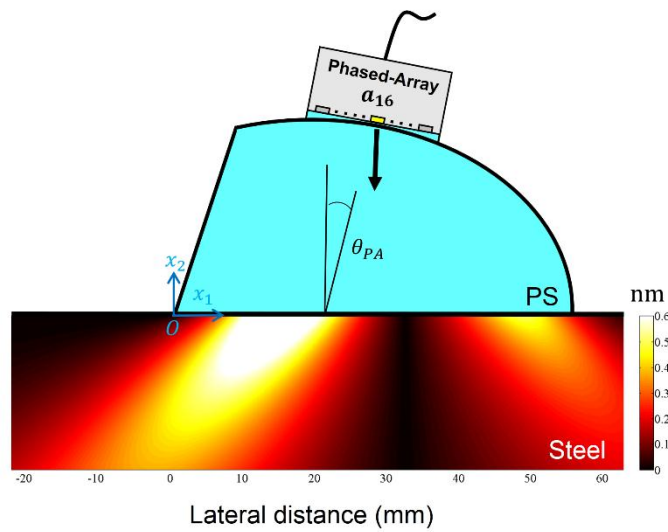


Figure 2.15 L-mode beam radiation models of transducer ch.16;

(a) $\theta_{PA} = 0^\circ$ and (b) $\theta_{PA} = 16^\circ$.



(a)



(b)

Figure 2.16 T-mode beam radiation models of transducer ch.16;

(a) $\theta_{PA} = 0^\circ$ and (b) $\theta_{PA} = 16^\circ$.

2.3.3 Verification of AWS using actual beam measurement

This section explains the verification of an actual ultrasonic beam radiation by means of experiments. The objective is to observe the phenomenon shown in **Figure 2.15(a)** and **(b)**, where the high intensity region of L-mode beam radiation shifted to the right when angle θ_{PA} is rotated to 16° . However, it is difficult to obtain direct comparison using similar situation since the PS wedge used for phased-array transducers is quite small. Therefore, an indirect comparison was considered using two experimental cases that help in implying above the mentioned phenomenon.

Experiment is divided into two steps. Experiment step-1 is performed on a single medium as shown in **Figure 2.17(a)**. The same phased-array transducer (PA) used throughout all angle beam tests in this dissertation is placed on a 39.5 mm thick PS rectangular prism. A pulse of central frequency at 5 MHz is transmitted from Ch.16 of such PA. A circular type single element transducer of 20 mm diameter and central frequency of 5 MHz is used as a receiver. There are 23 points for the measurement, where Pt.1 starting from the position -27.5 mm to the left of center line of PA. Interval between each point is kept as 2.5 mm. The measurements are conducted 3 times and the mean from 3 measurements is used to represent the result.

The experimental result for step-1 is shown in **Figure 2.17(b)**. Plotted amplitudes are corresponding to the TOF which ultrasonic wave required to travel from the surface of a transmitter to the surface of a receiver. Gauss integration is used on the receiver surface in order to obtain more precise amplitude data. Yellow line in **Figure 2.17(b)** is drawn using the mean from 3 measurements and it can be used to represent 1-D beam radiation on the bottom surface of PS prism. It can be observed that the peak beam radiation is located beneath the location of PA Ch.16 which was used as a transmitter. This verified the phenomenon which L-mode wave strongly propagated in normal direction.

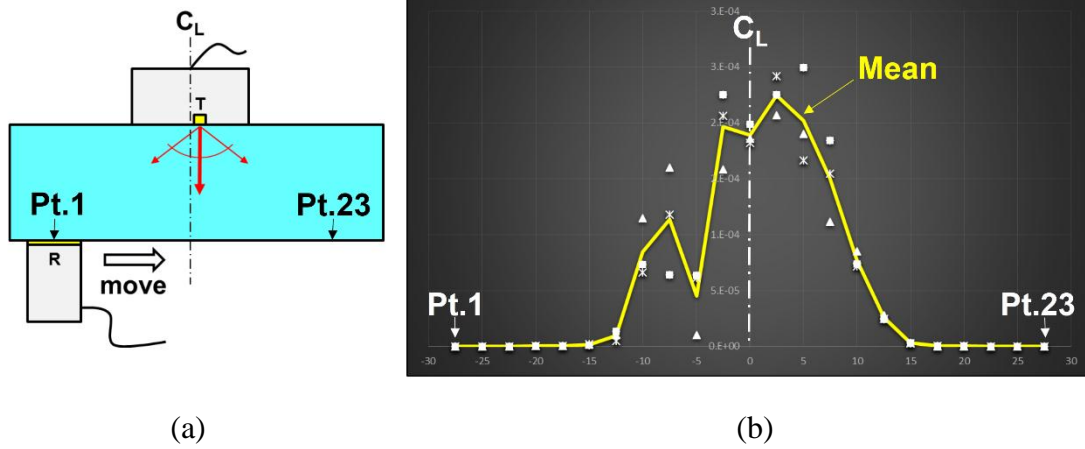


Figure 2.17 Verification of actual beam radiation in a single medium.

Experiment step-2 on a two solid media case is shown in **Figure 2.18(a)**. The same PA is placed on a large PS wedge of known geometry which is used as the first medium. A steel plate of thickness 21.5 mm is properly tied to the wedge using clamps. Couplant is applied on the interface between these two solids for ultrasonic wave to transmit efficiently. A pulse of central frequency at 5 MHz is transmitted from Ch.16 of PA. The same circular type single element transducer of 20 mm diameter and central frequency of 5 MHz is used as a receiver. Measurement is performed on 23 points where Pt.1 starting from -27.5 mm to the left of center line C_0 as shown in **Figure 2.18(a)**. Interval between each point is kept the same as 2.5 mm. Measurements are conducted 3 times, hence the mean is used to represent the result.

Experimental result for step-2 is shown in **Figure 2.18(b)**. Plotted amplitudes are corresponding to the TOF when the ultrasonic wave propagated from the surface of a transmitter, refracted at the interface and received at the surface of a receiver. Yellow line in **Figure 2.18(b)** represents 1-D beam radiation on the bottom surface of steel plate. It can be observed that the peak beam radiation is located beneath the location of PA Ch.16 which was used as a transmitter. This verified the phenomenon which L-mode wave strongly propagated in normal direction, even in the case of two solids media. Using such results, it can be implied that L-mode ultrasonic beam radiation approximated from the AWS is correct.

The investigation for T-mode actual beam radiation was performed using the same experimental result from step-2. Plotted amplitudes are corresponding to the TOF when the ultrasonic longitudinal wave propagated from the surface of a transmitter, converted to transverse wave at the interface, and received at the surface of a receiver. The yellow line in **Figure 2.19(b)** represents 1-D beam radiation on the bottom surface of steel plate in transverse wave mode. The magnitudes of received waves in this case are very small (order of 10^{-6}) compared to those from L-mode (order of 10^{-2}). Hence, it can be considered that the yellow line is showing the magnitude of noises. It can be implied that the actual beam radiation in transverse wave mode had not been yet verified through experiment. Changing of the receiver and its couplant may yield better result, however, it had not been tested in this dissertation, due to difficulties in the test setup.

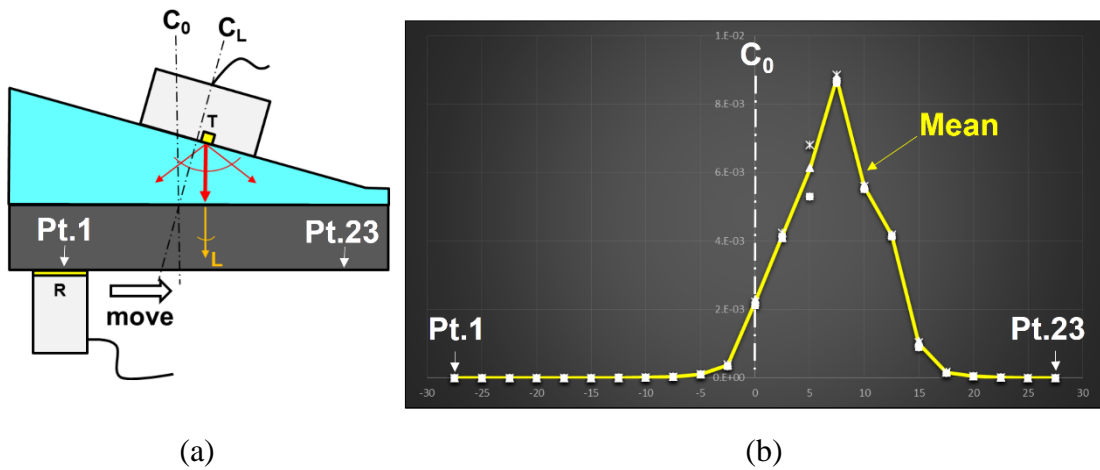


Figure 2.18 L-mode verification of actual beam radiation in two solids media.

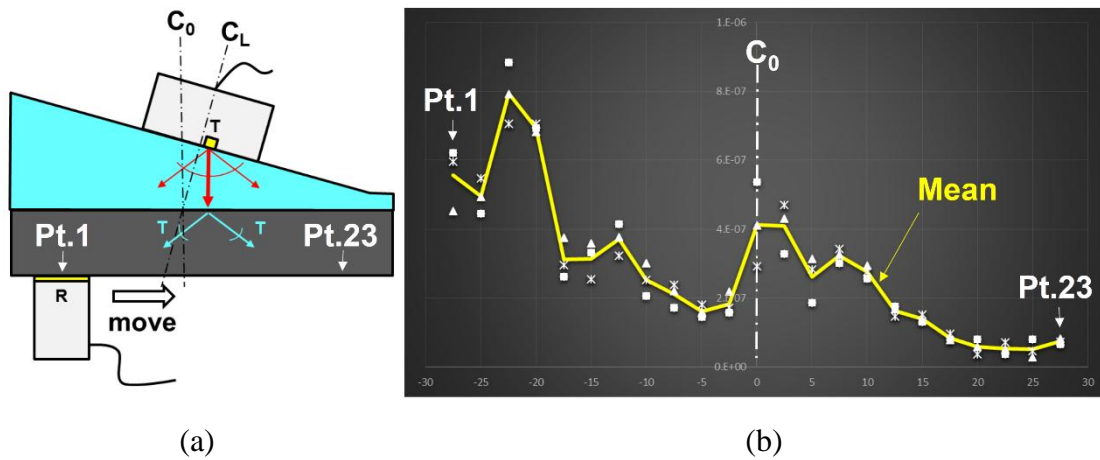


Figure 2.19 T-mode verification of actual beam radiation in two solids media.

2.4 AWS-SAFT

This section explains the AWS-SAFT. Sub-section 2.4.1 explains the implementation method used to account the AWS into the conventional SAFT for fluid-solid water immersion test. The implementation methods are mutual for both fluid-solid water immersion and solid-solid angle beam tests. However, it will be explained separately to avoid confusion. Therefore, the implementation method is explained again in sub-section 2.4.2 for solid-solid angle beam test.

2.4.1 Implementation of AWS into SAFT in water immersion test

This section explains the implementation of AWS into SAFT for fluid-solid water immersion test. Considering **Figure 2.11**, the pixel value at point \mathbf{b} located in ROI for a pair of transmitter i and receiver j can be computed from $|A_{ai,cj}(TOF_{ai,cj}^Y(\mathbf{b}))|$. In principle, however, there are other pixel points \mathbf{x} in ROI, for which the time of flight $TOF_{ai,cj}^Y(\mathbf{x})$ shows the same value as $TOF_{ai,cj}^Y(\mathbf{b})$. It means that when $S^Y(\mathbf{b})$ defined by Eq. (3) is plotted as a function of \mathbf{b} in SAFT imaging, the value of $|A_{ai,cj}(TOF_{ai,cj}^Y(\mathbf{b}))|$ may be distributed as undesired noises even at other pixel points where transmitted waves are very weak and no real scatterer exists. That is why images created by a conventional SAFT sometimes become unclear.

As described in the previous section, the displacement amplitude at a pixel point in ROI can be easily calculated by using AWS. Then it is expected that the incorporation of AWS with SAFT may reduce undesired noises from pixel points where only insignificant wave fields exist. Hence we propose the improved formula of AWS-SAFT as

$$AWS^Y(\mathbf{b}) = \sum_i \sum_j |A_{i,j}(TOF_{i,j}^Y(\mathbf{b}))u_i^Y(\mathbf{b})u_j^Y(\mathbf{b})|. \quad (2.26)$$

To show the efficiency of AWS-SAFT, we consider a single waveform obtained by a pulse-echo experiment using the 32th array element. The experimental conditions used are the same as those in case 1A in section 3. On the assumption that longitudinal waves propagate in the target specimen, **Figure 2.20(a)** shows the image of $|A_{32,32}(TOF_{32,32}^L(\mathbf{b}))|$ which corresponds to a part of a conventional SAFT. In this figure, it is shown that the amplitude of reflected longitudinal wave is distributed not only at the real defect position but also in side area of the defect. **Figure 2.20(b)** shows the

displacement amplitudes of AWS, $|u_{32}^L(\mathbf{b})u_{32}^L(\mathbf{b})|$, as a function of the position \mathbf{b} in ROI. **Figure 2.20(c)** illustrates the values of $|A_{32,32}(TOF_{32,32}^L(\mathbf{b}))u_{32}^L(\mathbf{b})u_{32}^L(\mathbf{b})|$, which may be a part of AWS-SAFT. Comparing with **Figure 2.20(a)**, **Figure 2.20(c)** gives the image intensity more concentrated around the defect.

Figure 2.21(a) to **(c)** are the same figures as **Figure 2.20(a)** to **(c)**, respectively, but for using the pulse-echo signal for 64th array element and assuming the propagation of transverse waves in a solid specimen. Similar results are obtained as in the case of **Figure 2.20**.

Philosophy for the implementation of AWS into SAFT is to account beam radiation computed from AWS into SAFT calculation. The key in accounting AWS beam radiation into SAFT is by *multiplying* $u_i^\gamma(\mathbf{b}, \omega)$ from **Equation 2.5** and $u_j^\gamma(\mathbf{b}, \omega)$ from **Equation 2.14** of mode γ into corresponding pixel value $|A_{ai,cj}(TOF_{ai,cj}^\gamma(\mathbf{b}))|$ of point \mathbf{b} using the same wave mode.

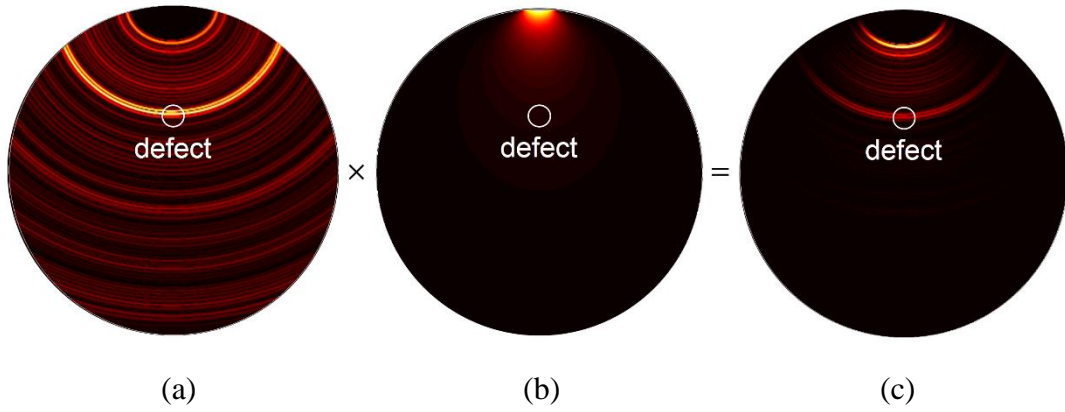


Figure 2.20 L-mode AWS-SAFT for transmitter $i = 32$ and receiver $j = 32$;

(a) $|A_{a32,c32}(TOF_{a32,c32}^L(\mathbf{b}))|$, (b) $|u_{32}^L(\mathbf{b})u_{32}^L(\mathbf{b})|$ and

(c) $|A_{a32,c32}(TOF_{a32,c32}^L(\mathbf{b}))u_{32}^L(\mathbf{b})u_{32}^L(\mathbf{b})|$.

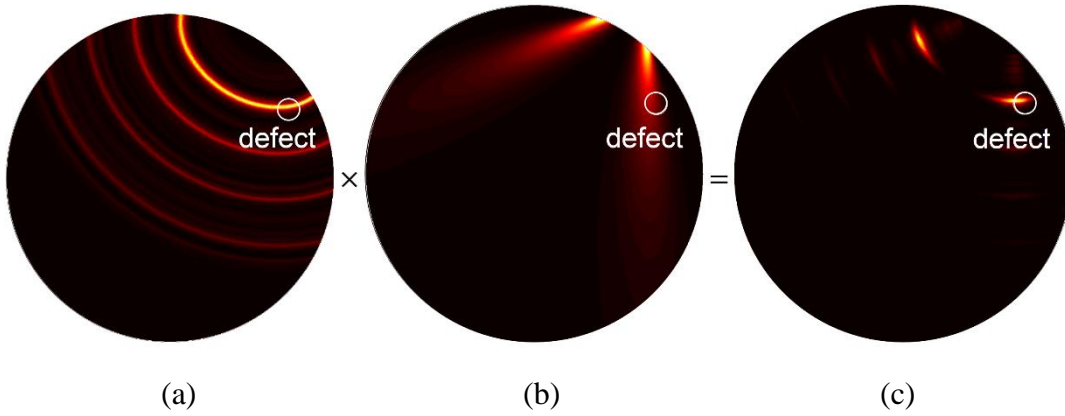


Figure 2.21 T-mode AWS-SAFT for transmitter $i = 64$ and receiver $j = 64$;

(a) $|A_{a64,c64}(TOF_{a64,c64}^T(\mathbf{b}))|$, (b) $|u_{64}^T(\mathbf{b})u_{64}^T(\mathbf{b})|$ and

(c) $|A_{a64,c64}(TOF_{a64,c64}^T(\mathbf{b}))u_{64}^T(\mathbf{b})u_{64}^T(\mathbf{b})|$.

2.4.2 Implementation of AWS into SAFT in angle beam test

This section explains the implementation of AWS into SAFT for a solid-solid angle beam test. Considering **Figure 2.14**, pixel value of point \mathbf{b} located in ROI for a pair of transmitter i and receiver j for wave mode γ can be computed from $|A_{ai,cj}(TOF_{ai,cj}^\gamma(\mathbf{b}))|$.

AWS-SAFT uses the same principle for both fluid-solid and solid-solid cases as mentioned earlier. The key in accounting AWS beam radiation into SAFT is by simply multiplying beam radiation approximate from AWS in **Equation 2.18** and **2.28** into corresponding pixel value $|A_{ai,cj}(TOF_{ai,cj}^\gamma(\mathbf{b}))|$ for all points \mathbf{b} in a test medium.

Figure 2.22 illustrates a test configuration which will be used throughout this section in order to demonstrate the computation of AWS-SAFT. A side-drilled hole (SDH) of diameter 1.5 mm was mocked into the steel plate as an artificial defect for ultrasound imaging. Demonstration for L-mode is shown in **Figure 2.23** where angle θ_{PA} is set to 16° , and for T-mode in **Figure 2.24** where angle θ_{PA} is set to 38° . These angles are selected as the same with those used in Chapter 4 where the rationale of selection is explained. A transducers pair where transmitter $i = 8$ and receiver $j = 24$ is selected for this demonstration.

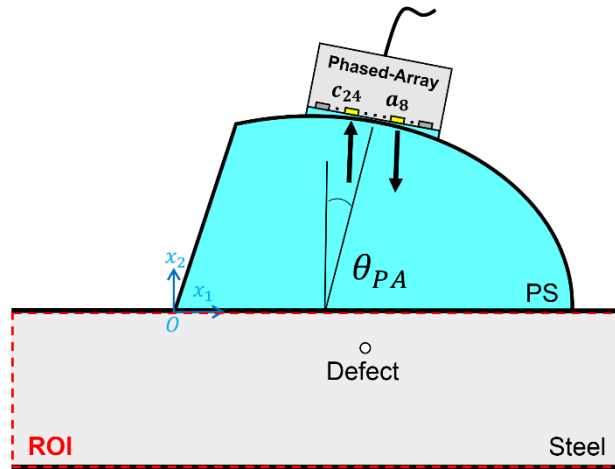
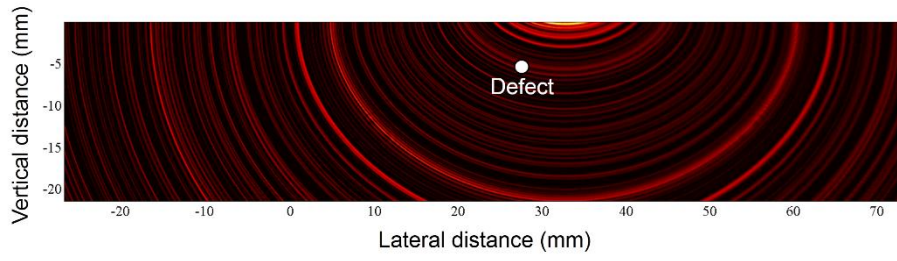


Figure 2.22 Test configuration for sub-section 2.4.2.

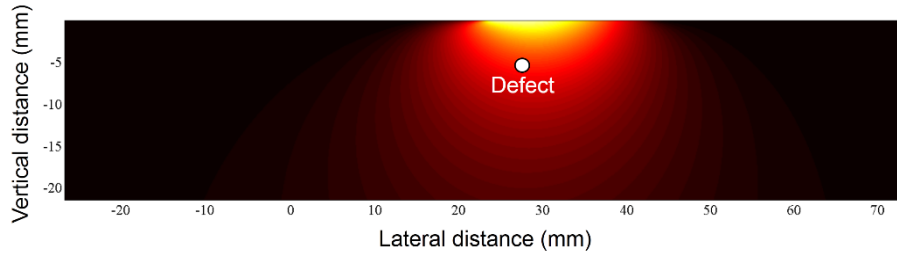
Considering **Figure 2.23(a)** and **2.24(a)**, plots of pixel values for all points \mathbf{b} in ROI are shown with location of the defect. In these figures, it is shown that the amplitude of reflected longitudinal wave is distributed not only at the real defect position but also in side area of the defect. Displacement field computed from AWS for the same pair of transmitter and receiver are shown in **Figure 2.23(b)** for L-mode and **Figure 2.24(b)** for T-mode. Absolute value $|u_8^y(\mathbf{b}, \omega)|$ and $|u_{24}^y(\mathbf{b}, \omega)|$ are used in plotting displacement field here since we only required the magnitude. Beam radiation of this transducers pair is then multiplied with SAFT pixel value, thus the pixel value for AWS-SAFT became $|A_{a8,c24}(TOF_{a8,c24}^y(\mathbf{b}))u_8^y(\mathbf{b})u_{24}^y(\mathbf{b})|$.

AWS-SAFT pixel plots for all pixel in ROI are shown in **Figure 2.23(c)** and **2.24(c)** for L- and T-mode, respectively. Comparing with **Figure 2.23(a)** and **2.24(a)**, **Figure 2.23(c)** and **2.24(c)** give the image intensity more concentrated around the defect. It can be observed that ultrasonic beam radiation model computed from the AWS had been accounted into SAFT, resulting in the amplification of pixel values over the region where the intensities of ultrasonic beam radiation is high. On the other hand, the pixel values over the region where the intensities of ultrasonic beam radiation are low are suppressed. Summation similar to conventional SAFT in **Equation 2.3** is represented in **Equation 2.26** for AWS-SAFT.

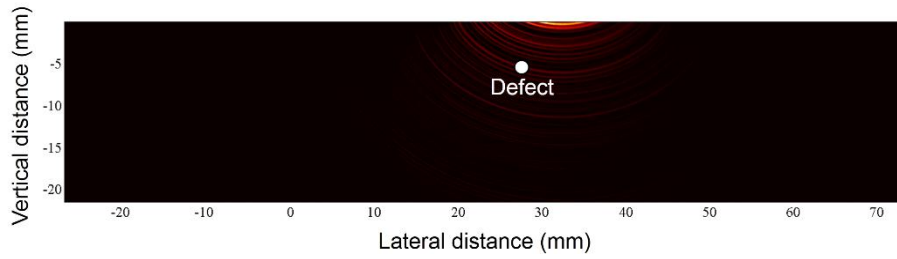
Plotting of $AWS^y(\mathbf{b})$ results in AWS-SAFT image which accounts ultrasonic beam radiation into the computation. Characteristics of this improved version of SAFT will be explained in chapter 4 for solid-solid angle beam test using a case study on ultrasound imaging of steel bottom defect.



(a)



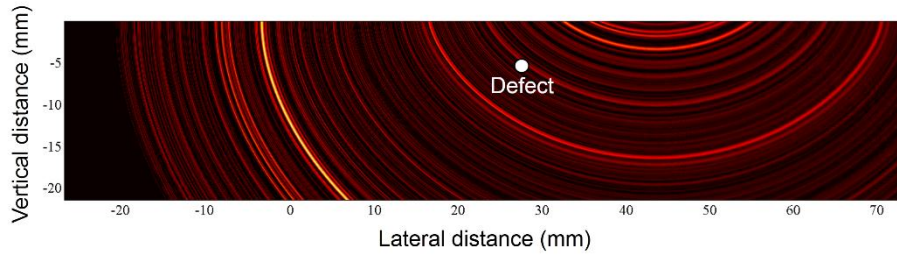
(b)



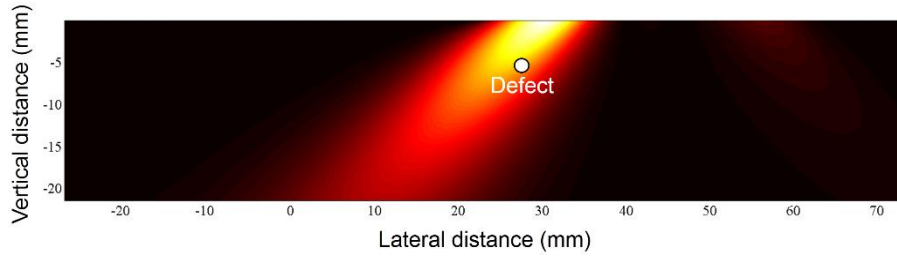
(c)

Figure 2.23 L-mode AWS-SAFT for transmitter $i = 8$ and receiver $j = 24$;

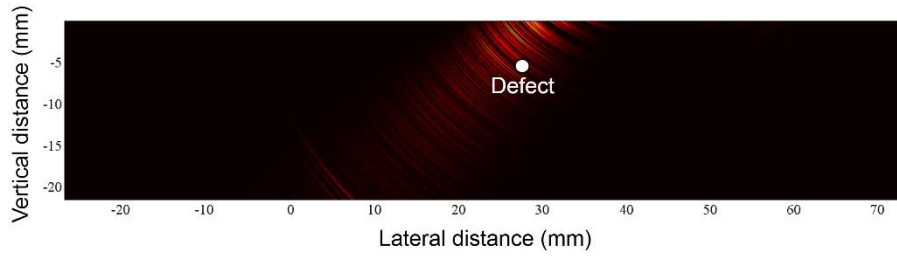
$$(a) |A_{a8,c24}(TOF_{a8,c24}^L(\mathbf{b}))|, (b) |u_8^L(\mathbf{b})u_{24}^L(\mathbf{b})| \text{ and} \\ (c) |A_{a8,c24}(TOF_{a8,c24}^L(\mathbf{b}))u_8^L(\mathbf{b})u_{24}^L(\mathbf{b})|.$$



(a)



(b)



(c)

Figure 2.24 T-mode AWS-SAFT for transmitter $i = 8$ and receiver $j = 24$;

$$(a) \left| A_{a8,c24} (TOF_{a8,c24}^T(\mathbf{b})) \right|, (b) \left| u_8^T(\mathbf{b}) u_{24}^T(\mathbf{b}) \right| \text{ and} \\ (c) \left| A_{a8,c24} (TOF_{a8,c24}^T(\mathbf{b})) u_8^T(\mathbf{b}) u_{24}^T(\mathbf{b}) \right|.$$

2.5 Summary

As a fundamental knowledge to fully understand this dissertation, three significant components are explained:

- Fundamental of ultrasonic testing
- Principles of SAFT in single medium and two media cases
- Modelling of ultrasonic beam radiation using the AWS

Ultrasonic beam radiation computed from AWS was verified using actual beam measurement. However, only L-mode could be verified successfully. For T-mode, the changing of receiving transducer and couplant may help to get meaningful result.

AWS-SAFT, an improved SAFT using the implementation of ultrasonic beam radiation computed using the AWS, was proposed. AWS can be accounted into SAFT using *multiplication*. At this stage, *objective I, define a clear implementation method to account AWS into SAFT algorithm*, was accomplished.

Performance of the proposed AWS-SAFT will be reported in Chapter 3 for fluid-solid water immersion test, and Chapter 4 for solid-solid angle beam test.

Chapter 3: *Application of AWS-SAFT in water immersion ultrasonic test*

In this chapter, the performance of the proposed AWS-SAFT in fluid-solid two-phase medium is evaluated by comparing ultrasound images from AWS-SAFT, with those from conventional SAFT. Experimental setup which is typical for all cases is explained in section 3.1. Experiment is organized in two steps, first, study on the characteristics of AWS-SAFT image is explained in section 3.2 (*to accomplish Objective II*). Then, efficient method to obtain ultrasound image of a rod specimen is proposed and tested in section 3.3 (*to accomplish Objective III*). A summary is given in section 3.4.

3.1 Experimental setup

All ultrasonic tests are performed using a 64 channels linear phased-array transducer (PA) with main frequency of 5 MHz produced by KGK (Kanagawa, JAPAN) as shown in **Figure 3.1**. Element size is 0.4 mm×12.0 mm aligned with 0.5 mm pitch between adjacent elements. A pulser-receiver (TOSHIBA CC-TW-215MRY, Tokyo, JAPAN) as seen in **Figure 3.2** is used, which generates pulses with main frequency of 5 MHz. Wave data is acquired using control software from the same maker with sampling frequency of 50 MHz and averaged 128 times to get stabilized signals. No gain is added in order to suppress noises to minimum level. An aluminum rod specimen is shown in **Figure 3.3**. Diameter and the length of a rod specimen is 30 mm and 50 mm, respectively. Diameter of a side-drilled hole (SDH) is 2 mm and is typical for all SDHs. The water distance between the center of a PA to the specimen's top surface is set to 10 mm as shown in **Figure 3.4**.

A sketch of experimental setup is shown in **Figure 3.4**, and the actual photo of the experimental setup is shown in **Figure 3.5**. The earliest reflection or the ultrasound transmitted from transducer channel 32 or 33 located at the center of PA to the nearest curved surface and reflected back to the same transducers arrived at 13.6 μ s, hence delay time is set as 12.5 μ s in order to record earliest reflection wave data. Number of recorded digitized data is 1024 points yields time increments of 0.02 μ s, thus end recording time would be 32.98 μ s.

L-mode wave velocity in water is 1470 m/s and the L- and T-mode wave velocities in aluminum are 6300 m/s and 3130 m/s, respectively. The longest travelling route expected to be recorded in this setup is ultrasound wave travelling from transducer channel 32 or 33 striking at the interface and propagated to the side surface of rod specimen in T-mode, then reflected back via the same route. Round trip travelling distance in water is 20 mm and in rod specimen is 60 mm, assumed using the diameter of a rod which is the largest distance in a circle. Using wave velocities mentioned above, TOF of this route can be calculated as $32.77\mu\text{s}$. Therefore, wave data recorded from $12.5\mu\text{s}$ to $32.98\mu\text{s}$ as mentioned before is enough to record every scattered wave from both L- and T- modes.



Figure 3.1 64 channels linear phased-array transducers.



Figure 3.2 Pulser-receiver and wave acquisition system.

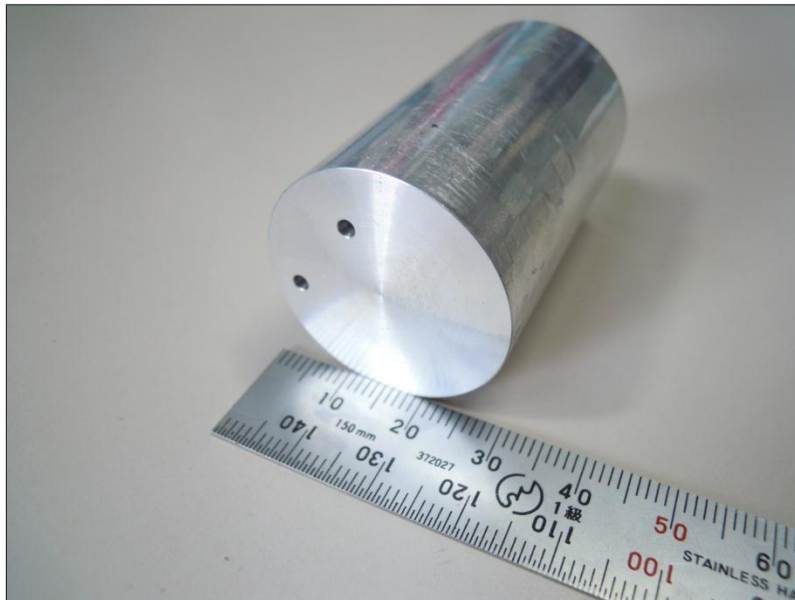


Figure 3.3 A typical rod specimen.

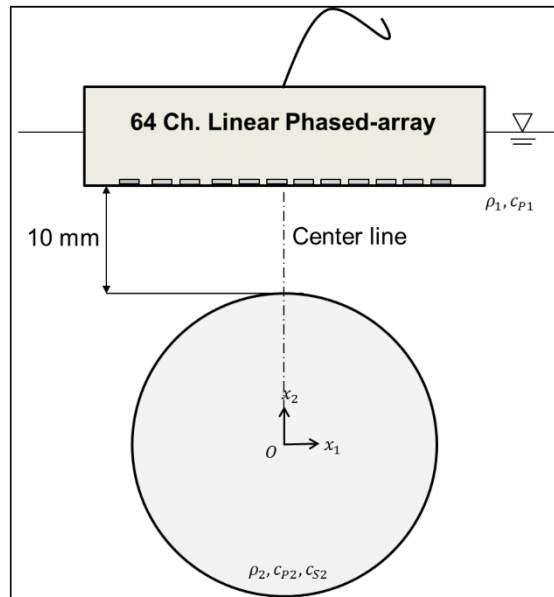


Figure 3.4 Outline of water immersion test

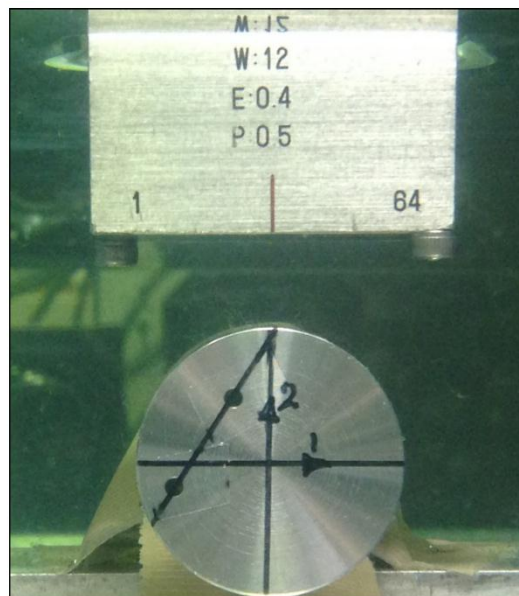


Figure 3.5 Photo of experimental setup.

3.2 Study on characteristics of an AWS-SAFT image

In this section, the characteristics, or the performances of AWS-SAFT are confirmed using ultrasound imaging of an SDH in an aluminum rod specimens, each one located in different position. Position of SDHs are designed to evaluate performance of AWS-SAFT in the cases when SDHs are located *inside* and *outside* the region where intensities of AWS ultrasonic beam radiation are high. Summed beam radiations from all available transducer of this PA for L- and T-modes, which are computed by AWS, are shown in **Figure 3.6** and **3.7**, respectively. Plotted values were normalized and contour lines were added to indicate the intensity of ultrasonic beam radiation in various region over the cross-section of a rod specimen.

Considering the intensity of radiated ultrasound, improvement effect of AWS-SAFT can be predicted using the consideration that the region where the intensities of the AWS ultrasonic beam radiation are high (White and yellow region in **Figures 3.6** and **3.7**) is supposed to get more improvement effect than the region where the intensities of AWS are low. If an SDH is located inside the AWS's high intensity region (assume that it is where the magnitudes of normalized displacement values are larger than 0.1 in both L and T-modes), high improvement effect when using AWS-SAFT can be anticipated. On the other hand, if defect is located outside the high intensity region where displacement values are smaller than 0.1, improvement effect will be gradually minimized according to defect location.

Region in which normalized magnitude of displacement values are larger than 0.1 will be called the *Effective Region (ER)*.

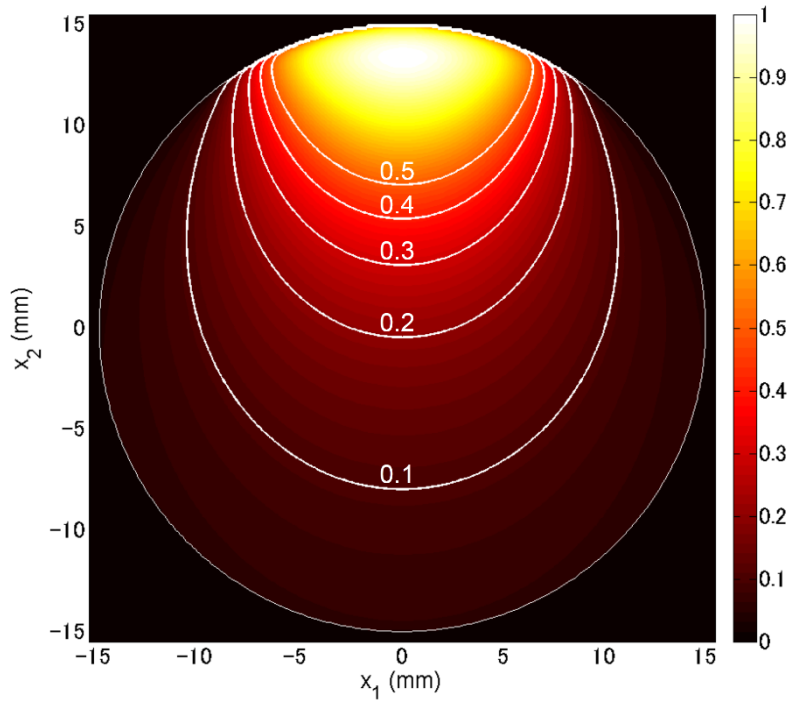


Figure 3.6 L-mode summed AWS beam radiations from all 64 transducers;
 $\sum_i \sum_j |u_i^L u_j^L|$.

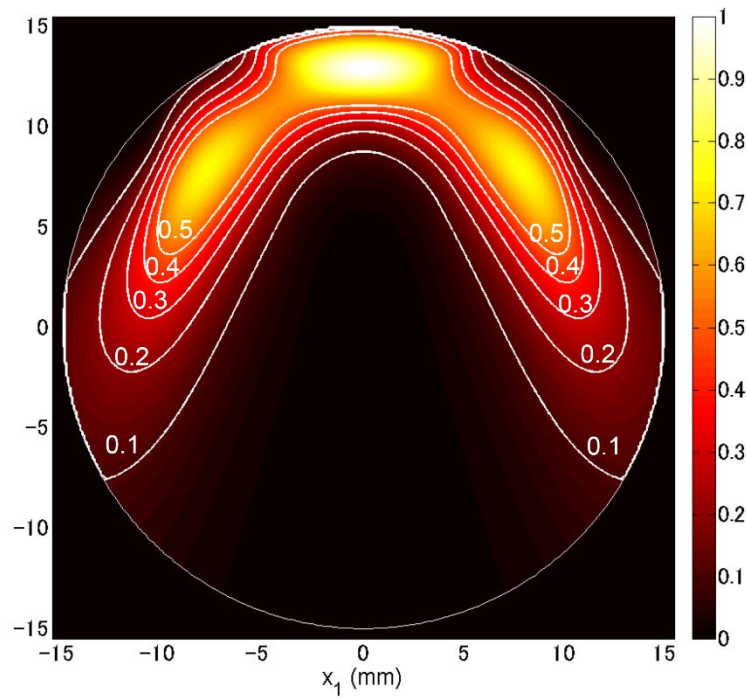


Figure 3.7 T-mode summed AWS beam radiations from all 64 transducers;
 $\sum_i \sum_j |u_i^T u_j^T|$.

Four specimens shown in **Figure 3.8** were designed to confirm the performance of this theory. Numbering codes for each specimen shown under specimen photo in **Figure 3.8** represent as follows: 1 stands for step 1 and alphabets after the number are used to designate each case. Case 1A and 1B are those which high improvement effect is anticipated for L- and T-mode, respectively. Case 1C and 1D were designed to test our assumption that if defects are outside the AWS's high intensity area, the improvement effect will be minimized. In these two cases, SDHs are both located outside the ER hence improvement effect should be remarkably small.

Experimental results are shown in **Figures 3.9-3.12**. The pixel width used throughout this paper is 0.1 mm. In each figure, the benchmark image is shown in **Figure a** as a reference image, where the pixel value on the boundary of an SDH is 1.0, while the values are zero outside the SDH and inside the boundary of an SDH. The width of the boundary strip of an SDH is assumed as 0.15 mm. **Figures b** and **c** show the flaw images obtained by means of the conventional SAFT and the AWS-SAFT, respectively. For images in **Figures a-c**, the index for image quality assessment, called Mean Structural Similarity (MSSIM, see Appendix A), is calculated. For a reference image shown in **Figure a**, MSSIM is set to 1, and $MSSIM (0 \leq MSSIM \leq 1)$ gives a higher value for an image more similar to the reference image. Constants used in MSSIM calculation using **Equation A1-A8** in the **Appendix A** are $K_1 = 0.01$, $K_2 = 0.03$ and $L = 1$.

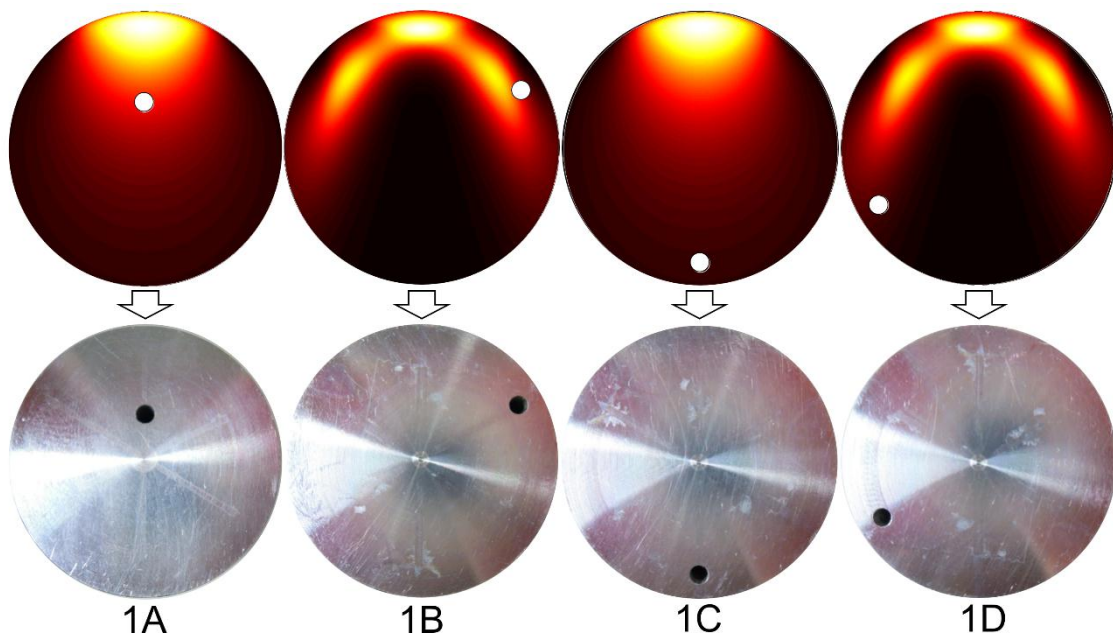
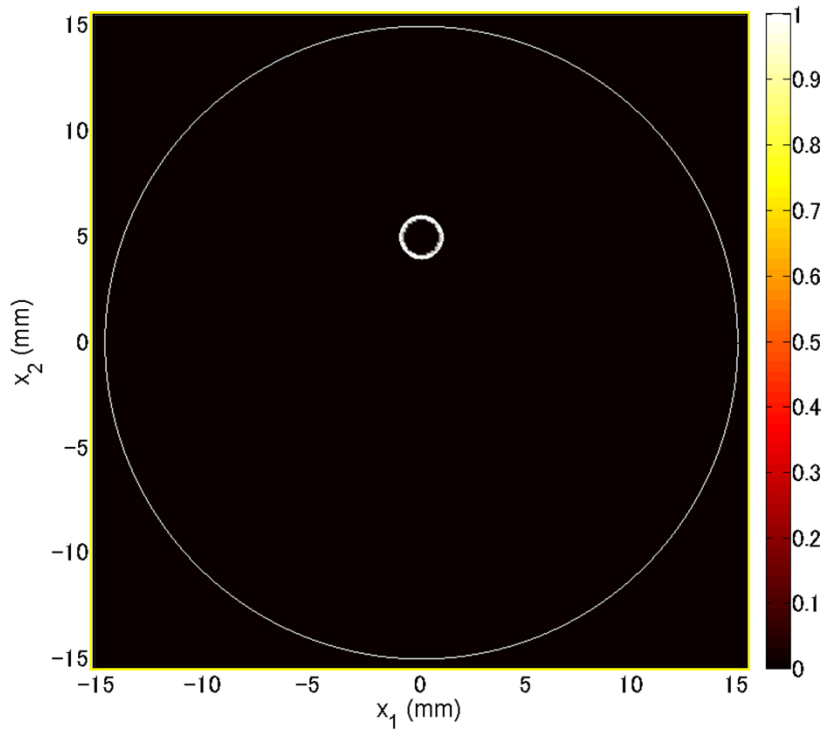


Figure 3.8 Specimens for experiment step 1.

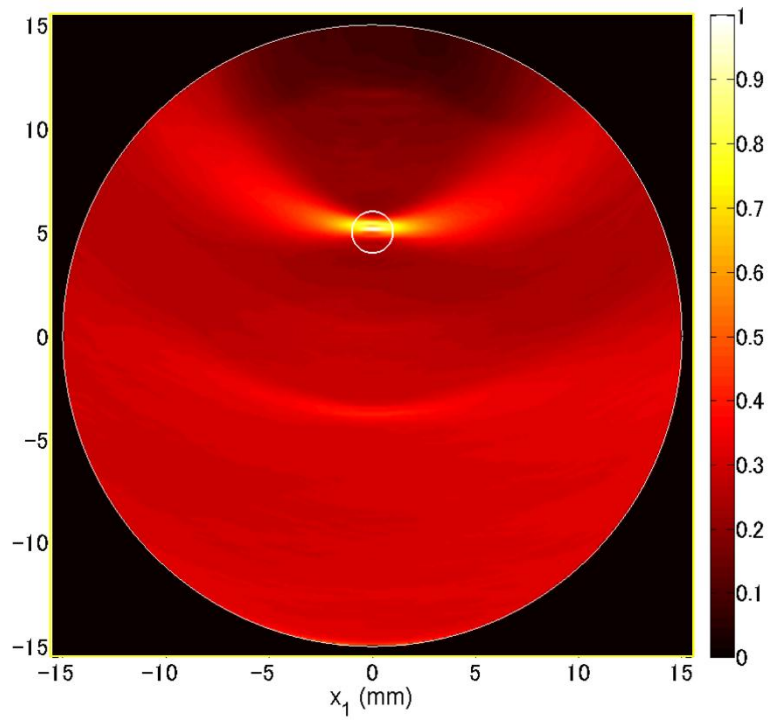
Figure 3.9 shows results of AWS-SAFT using the L-wave mode for case 1A where the SDH is inside the effective zone of L-mode. As seen in **Figures b** and **c**, the SDH images are localized correctly by both SAFT and AWS-SAFT, respectively. Using AWS-SAFT, overall noises of the image are reduced, hence the SDH image becomes clearer. Moreover, the SDH image by AWS-SAFT has less side lobes than SAFT. The MSSIM values for **Figures b** and **c** are 0.2713 and 0.2881, respectively. Therefore, there is not much difference in MSSIMs for AWS-SAFT and SAFT since the image configuration does not differ much compared to the benchmark in **Figure a**.



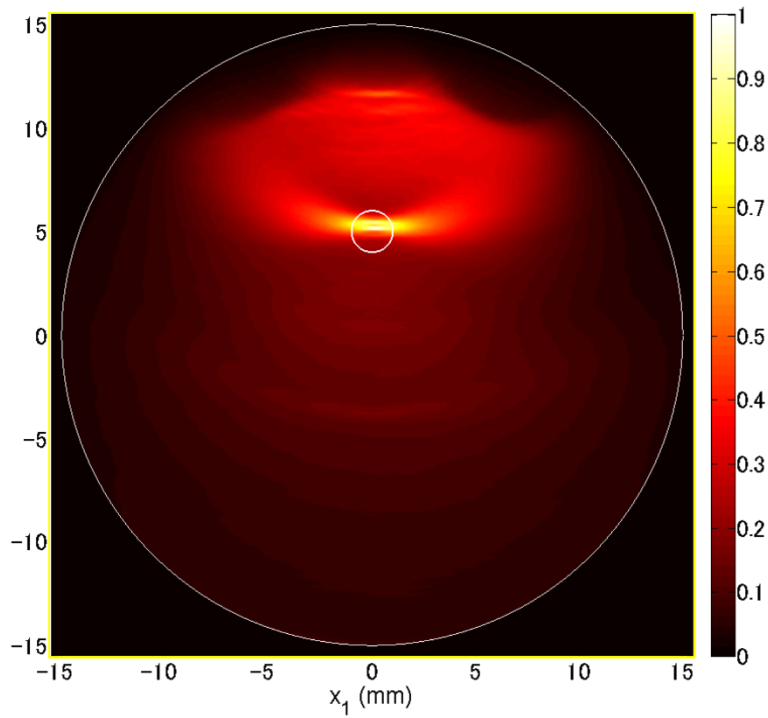
(a)

Figure 3.9 Case 1A results when SDH is inside the ER of L-mode.

(a) Benchmark, MSSIM = 1; (b) SAFT, MSSIM = 0.2713 and (c) AWS-SAFT, MSSIM = 0.2881.



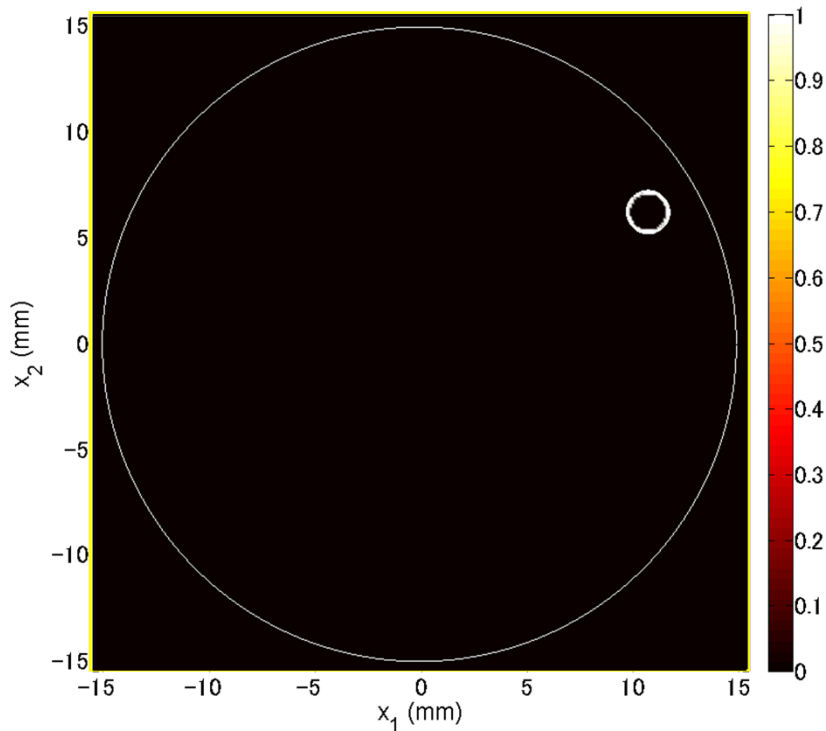
(b)



(c)

Figure 3.9 (con't.) Case 1A results when SDH is inside the ER of L-mode.
 (a) Benchmark, MSSIM = 1; (b) SAFT, MSSIM = 0.2713 and (c) AWS-SAFT, MSSIM = 0.2881.

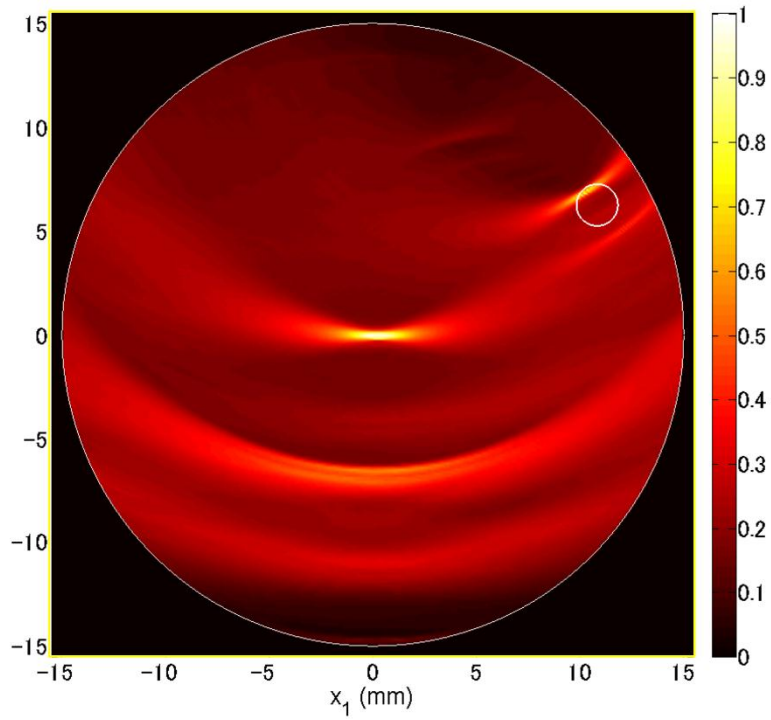
The images using the T-wave mode, for case 1B are shown in **Figure 3.10**, where the SDH is inside the effective zone of T-mode. The SDH images are localized correctly by both SAFT and AWS-SAFT in **Figure (b)** and **Figure (c)**, respectively. However, in SAFT, artifacts due to the longitudinal wave reflected from the bottom of the specimen are observed in the central area of the specimen making the conventional SAFT result inappropriate for NDE since those artifacts may lead to misinterpretation. However, these artifacts are eliminated in AWS-SAFT and overall noises of the image are remarkably reduced. In addition, the SDH image between the right side of SDH and the boundary of a rod is suppressed because it is outside the effective zone. The MSSIM values for figures b and c are 0.2727 and 0.4878, respectively. In this case, the elimination of artifacts in AWS-SAFT strongly influences the image configuration, hence the SDH image by AWS-SAFT is much similar to the benchmark in **Figure (a)**. In this case, the use of AWS-SAFT helps making the ambiguous result more meaningful.



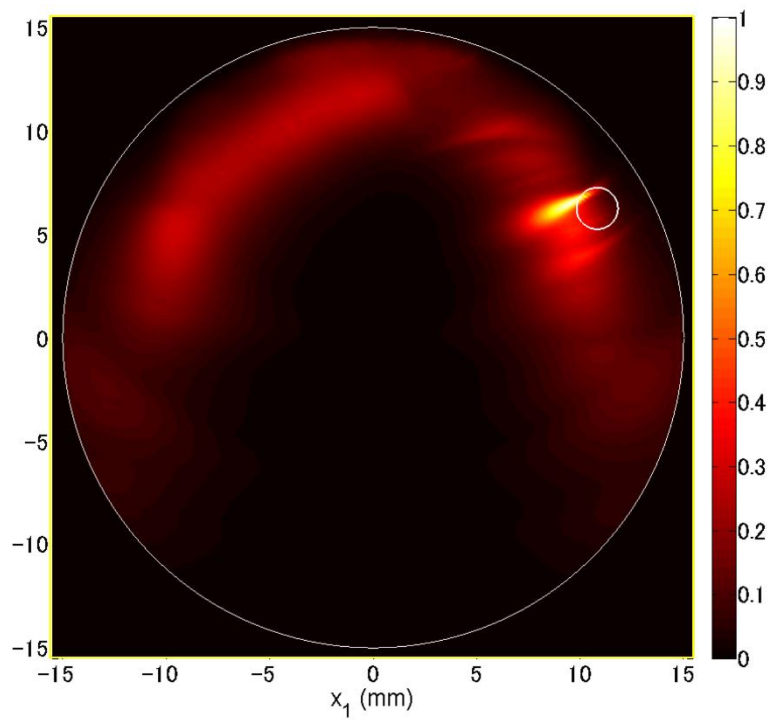
(a)

Figure 3.10 Case 1B results when SDH is inside the ER of T-mode.

(a) Benchmark, MSSIM = 1; (b) SAFT, MSSIM = 0.2727 and (c) AWS-SAFT, MSSIM = 0.4878.



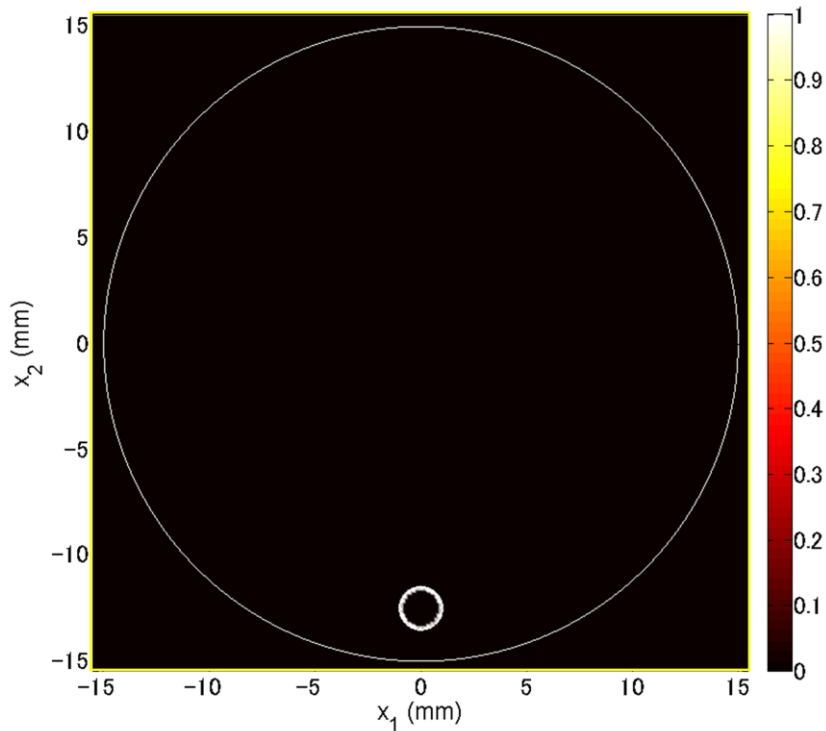
(b)



(c)

Figure 3.10 (con't.) Case 1B results when SDH is inside the ER of T-mode. (a) Benchmark, MSSIM = 1; (b) SAFT, MSSIM = 0.2727 and (c) AWS-SAFT, MSSIM = 0.4878.

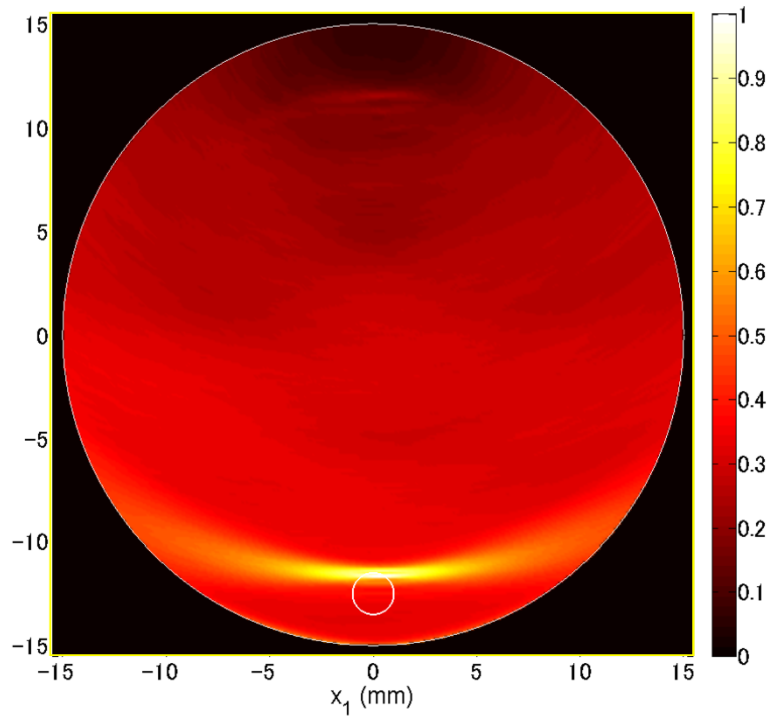
Figure 3.11 shows results using the L-wave mode for case 1C where the SDH is outside the effective zone of L-mode. The location of an SDH is detected correctly by both SAFT and AWS-SAFT in **Figures b** and **c**, respectively. In **Figure c**, however, noises inside the L-mode effective zone are amplified. The MSSIM values for **Figures b** and **c** are 0.2714 and 0.2792, respectively. Therefore, there is little difference in MSSIMs for AWS-SAFT and SAFT since the image configuration does not differ much compared to the benchmark in **Figure a**. Results in this case are considered inappropriate for NDE as they lead to misinterpretation. AWS-SAFT has negligible effect in this cases since the difference between two cases is mainly on luminance comparison function defined in **Equation A2**.



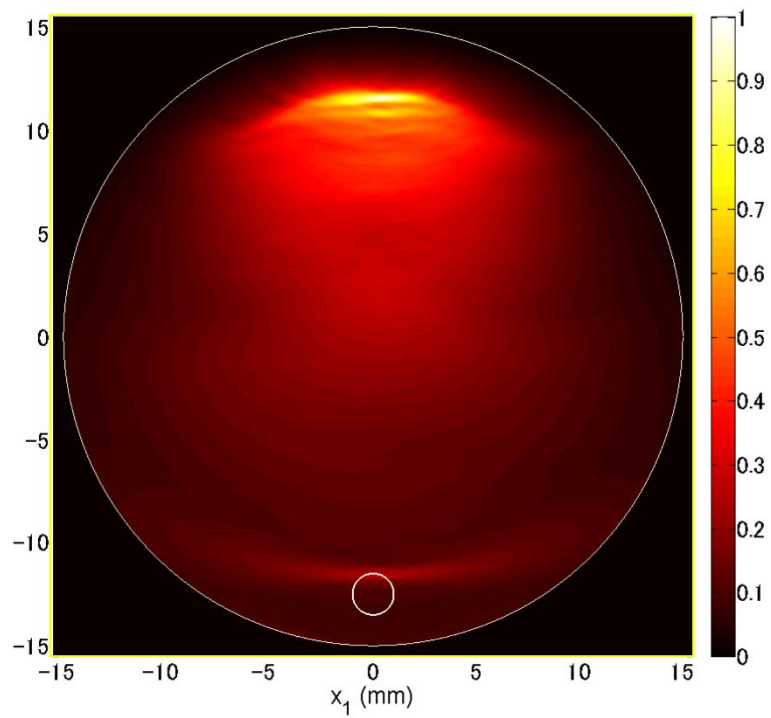
(a)

Figure 3.11 Case 1C results when SDH is outside the ER of L-mode.

(a) Benchmark, MSSIM = 1; (b) SAFT, MSSIM = 0.2714 and (c) AWS-SAFT, MSSIM = 0.2792.



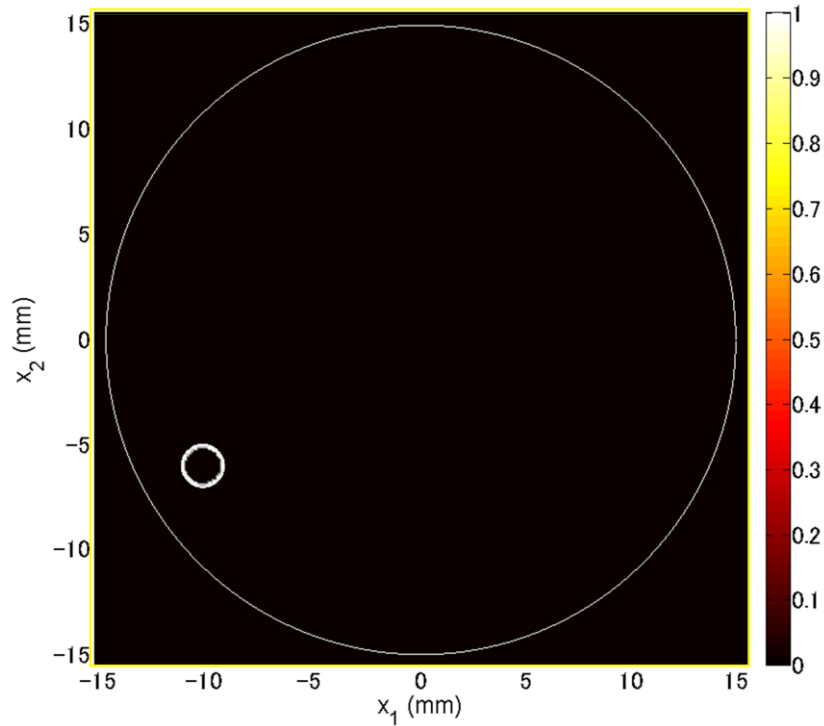
(b)



(c)

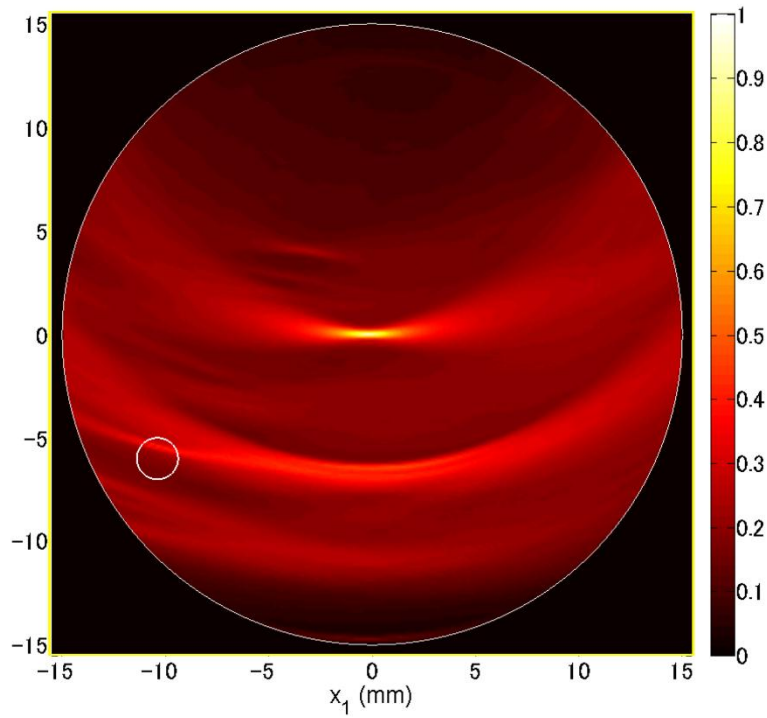
Figure 3.11 (con't.) Case 1C results when SDH is outside the ER of L-mode.
 (a) Benchmark, MSSIM = 1; (b) SAFT, MSSIM = 0.2714 and (c) AWS-SAFT, MSSIM = 0.2792.

SDH images using T-wave mode, for case 1D are shown in **Figure 3.12**, where the SDH is outside the effective zone of T-mode. As shown in **Figures b** and **c**, the SDH images contain high level of noises. Using AWS-SAFT, however, artifacts from L-mode are eliminated. On the other hand, noises inside the effective zone of T-mode are amplified, hence the SDH image does not become as clear as in case 1B. The MSSIM values for **Figures b** and **c** are 0.2740 and 0.3956. Therefore it is said that the elimination of L-mode artifacts makes AWS-SAFT image much similar to the reference image in **Figure a**. Results in this case are also considered inappropriate for NDE since they lead to misinterpretation.

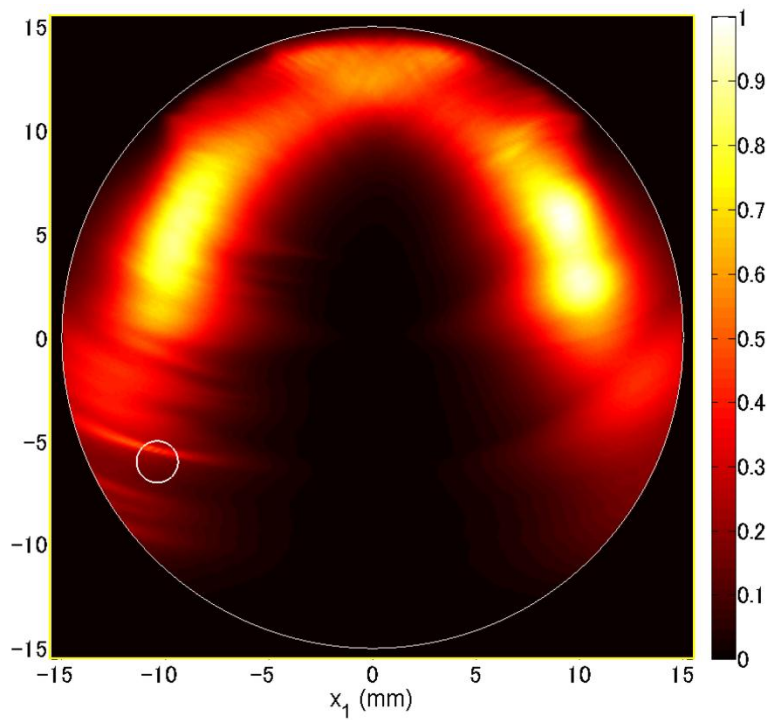


(a)

Figure 3.12 Case 1D results when SDH is outside the effective zone of T-mode.
 (a) Benchmark, MSSIM = 1; (b) SAFT, MSSIM = 0.2740 and (c) AWS-SAFT, MSSIM = 0.3956.



(b)



(c)

Figure 3.12 (con't.) Case 1D results when SDH is outside the effective zone of T-mode. (a) Benchmark, MSSIM = 1; (b) SAFT, MSSIM = 0.2740 and (c) AWS-SAFT, MSSIM = 0.3956.

From the results of step 1, performances of the AWS-SAFT were studied and it was shown that this proposed method improved the conventional SAFT, if used with a consideration of the ER in each wave mode. Strong points of the AWS-SAFT were observed as follows:

1. Improvement effects: SDH image can be obtained with narrower side lobes and overall noises reduction, if an SDH is located inside the ER.
2. Artifacts of L-mode which are normally appear in T-mode results can be eliminated.
3. Noises outside the ER are remarkably reduced.

On the other hand, drawback was observed when an SDH located outside the ER. In that case, noises inside the ER would be highly amplified, hence the SDH image became less clear.

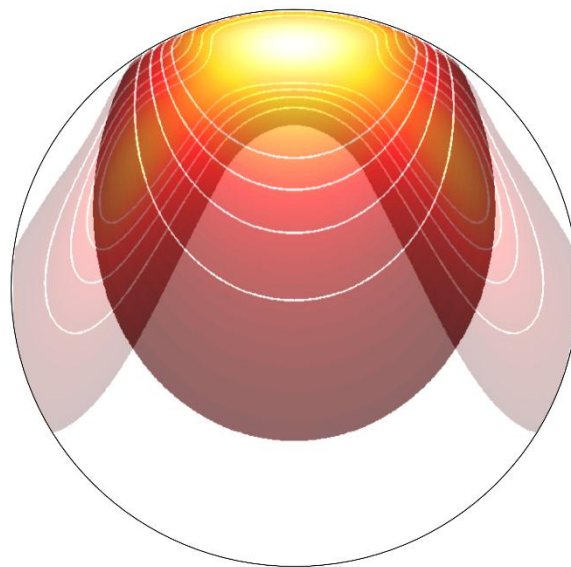
In the next section, an efficient way to use AWS-SAFT to obtain the ultrasound images of SDHs in a rod specimen will be explained as a demonstration on how to use the AWS-SAFT with consideration of the ER concept.

3.3 Efficient way to obtain ultrasound images of SDHs in a rod specimen by AWS-SAFT

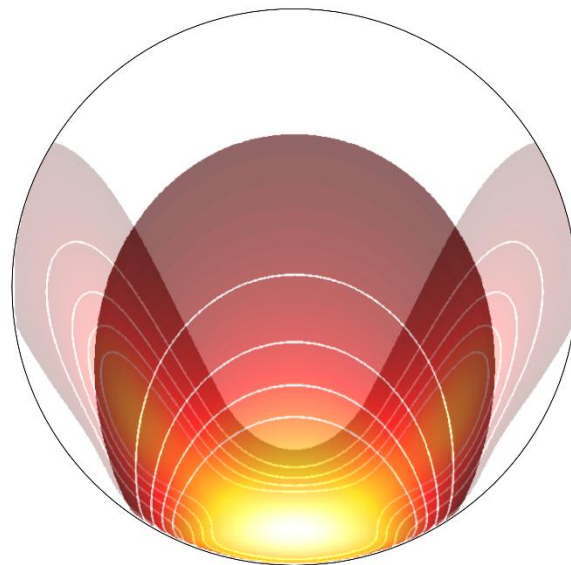
In this section, an efficient way to get ultrasound image of a rod specimen with SDHs in arbitrary locations is proposed. AWS-SAFT will be used as a typical method to obtain images of SDHs in rod specimens since it is verified in section 3.2 that AWS-SAFT supersedes the conventional SAFT if SDH located inside the ER. Considering **Figure 3.6** and **3.7** again, shape of the ERs for L- and T-modes when transducer is placed on the top of specimen are known.

Considering **Figure 3.13(a)**, ER of L- and T-modes when a PA is located on the top of a rod specimen are superposed. From this result, it can be predicted that using AWS-SAFT in both L- and T-modes can provide ultrasound image, sufficient to see an SDH located in any region over the upper half of a rod specimen except for the two low intensity area on the rims which are outside the ER.

However, lower half of a rod specimen has low improvement effect as verified in section 3.2, thus from inspection by placing a PA only on the top may yield insufficient result to localized an SDH in the lower half of a rod specimen. L- and T-modes ER when transducer is located under the bottom of a rod specimen is shown in **Figure 3.13(b)**. It can be predicted that sufficient result to localize SDH in lower half can be obtained by performing one more set of an ultrasonic test by placing a PA under the bottom of a rod specimen.



(a)



(b)

Figure 3.13 L- and T-mode combined ER in case transducer on (a) top and (b) bottom.

Eventually, using a superposition of these two results, an SDH inside most area of a rod specimen can be localized. This section will experimentally prove this theory. Basically, adding two more sets of UTs when a PA is located on the left and right sides of a rod shall make the SDH image much clearer, however, twice in experimental and computational time. Therefore, we will also prove that only two sets are enough to localize an SDH inside most area of the specimen by comparing superposed results from two and four sets.

Two cases of experiment are designed to prove the above-mentioned theory. Case 2A is shown in **Figure 3.14(a)** where two SDHs are both located inside the ER of T-mode, one in the upper half and another one in the lower-half. T-mode ERs where transducers are on the top and the bottom of the specimen are shown in **Figure 3.14(b)** and **(c)**, respectively. It can be predicted that both SDHs would be sufficiently localized using T-mode AWS-SAFT on two sets of UTs when a PA is placed over and under a rod specimen.

Case 2B is shown in **Figure 3.15(a)** where one SDH is inside the ER of L-mode shown in **Figure 3.15(b)** and another one is inside the ER of T-mode shown in **Figure 3.15(c)**. In this case, two sets of UTs using the same configuration as in case 2A are required to localize the SDHs. In addition, both L- and T-modes AWS-SAFT images are required since each SDH is located inside the ER of different mode. It can be predicted that sufficient localization of both SDHs would be obtained by superposing the L-mode result with the T-mode result.

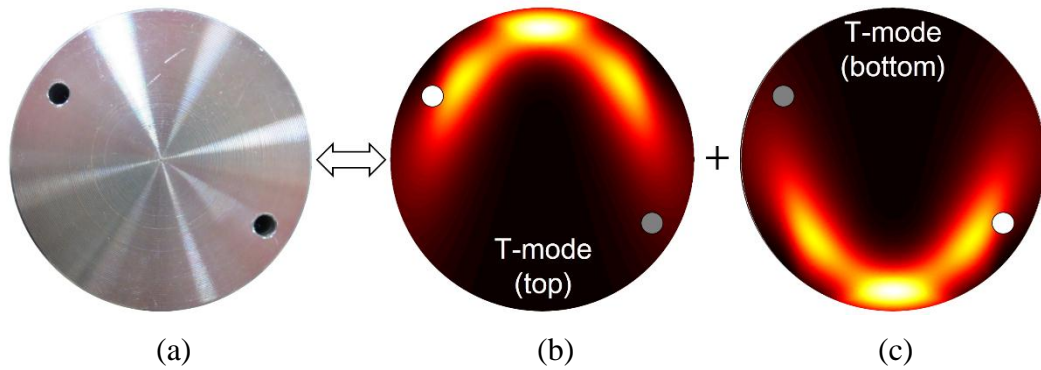


Figure 3.14 (a) Specimen for experiment case 2A and its ER in case of (b) T-mode with transducer on top and (c) T-mode with transducer at the bottom.

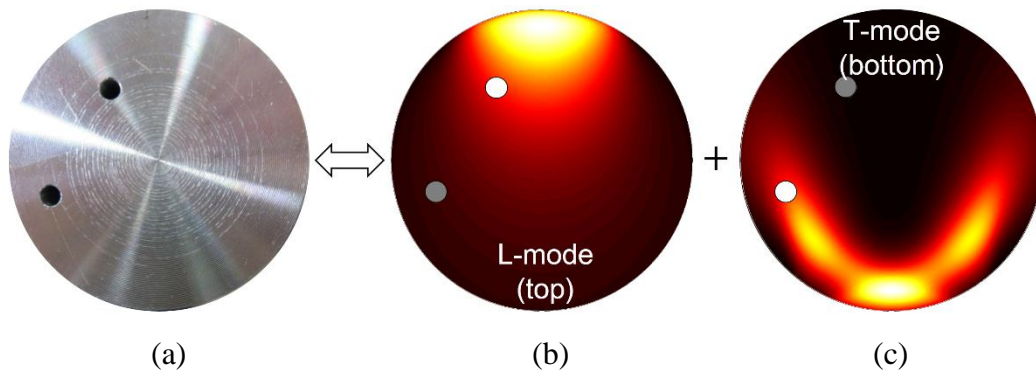
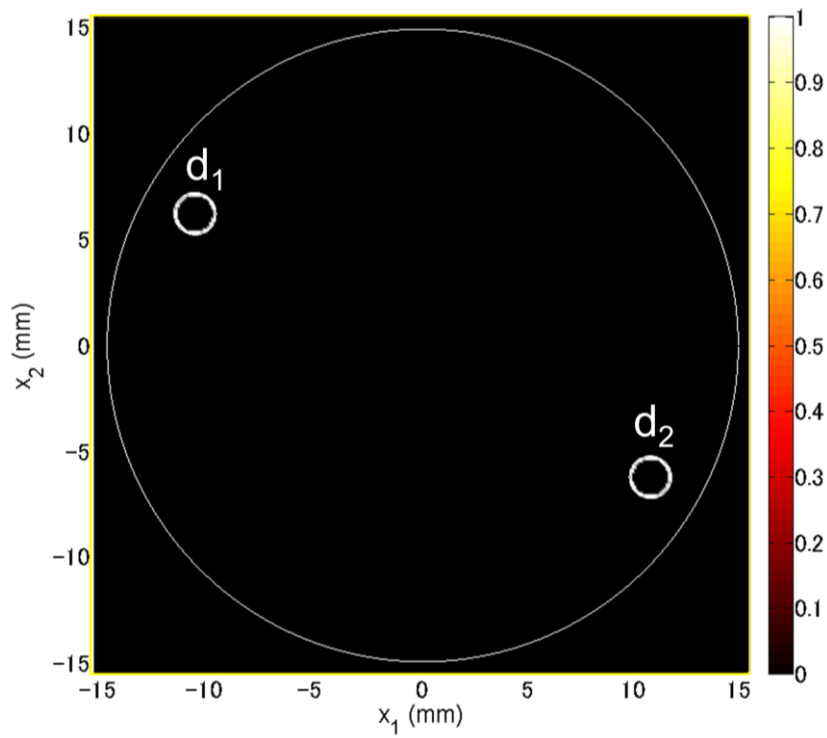


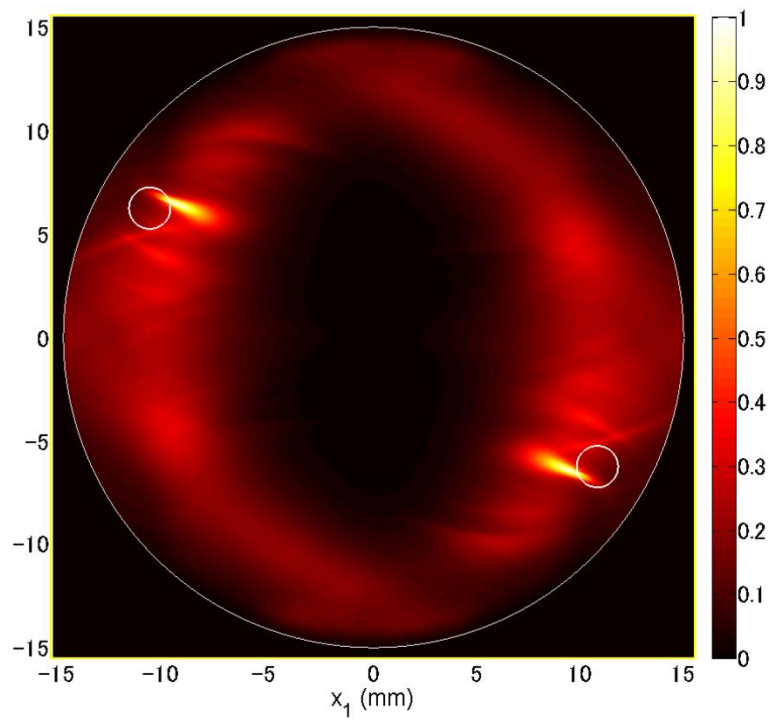
Figure 3.15 (a) Specimen for experiment case 2B and its ER in case of (b) L-mode with transducer on top and (c) T-mode with transducer at the bottom.

Figure 3.16 shows results from case 2A where SDHs d_1 and d_2 are both inside the ER of T-mode. **Figures 3.16(b)** and **3.16(c)** are superposed images using AWS-SAFT results from two and four sets, respectively.

Using HVS, both SDHs are localized correctly using only two sets of UTs. By adding two more sets where transducers are on the left and right sides of a rod specimen, the opposite boundaries of both SDHs can be imaged which give more information regarding the shape of SDHs as a benefit from doubling the time-consuming. The MSSIM values for two and four sets are 0.3508 and 0.3231, respectively, hence the difference is 0.0277. Difference in MSSIMs are very small since image configurations of both results do not differ much comparing to the benchmark in **Figure 3.16(a)**.



(a)

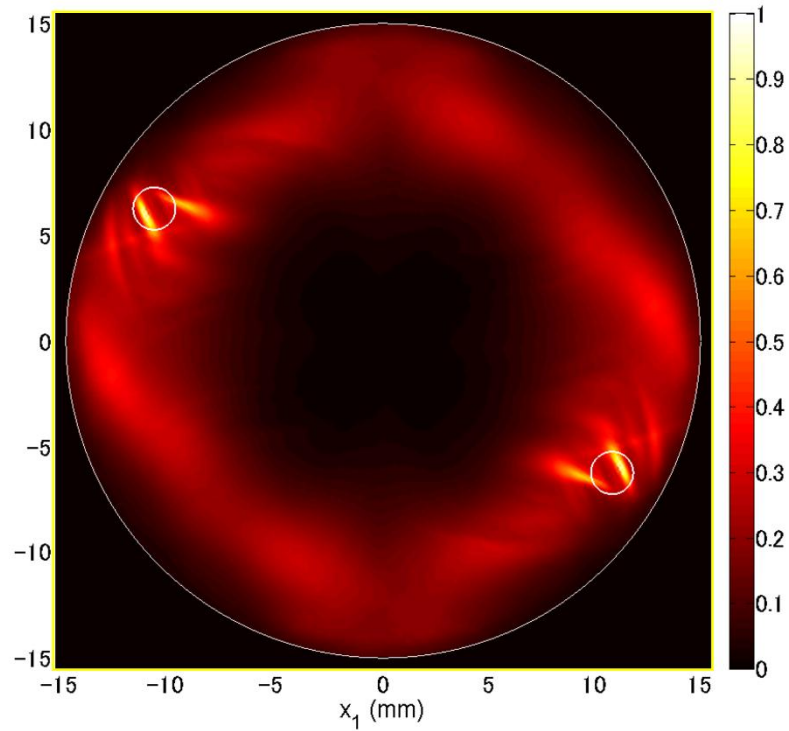


(b)

Figure 3.16 Case 2A results where both d_1 and d_2 are inside ER of T-mode.

(a) Benchmark, MSSIM = 1; (b) two tests, MSSIM = 0.3508 and

(c) four tests, MSSIM = 0.3231.

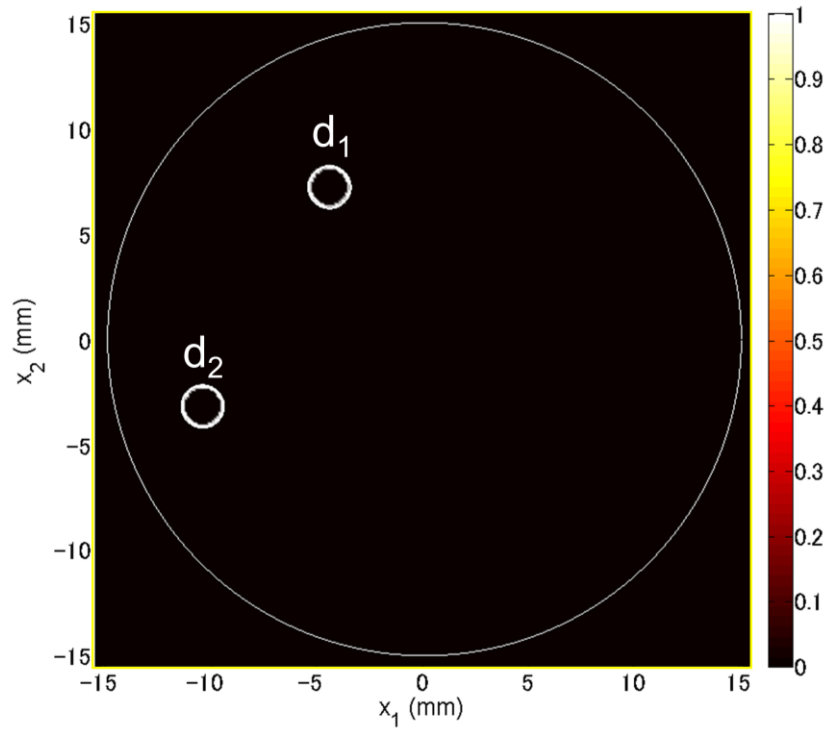


(c)

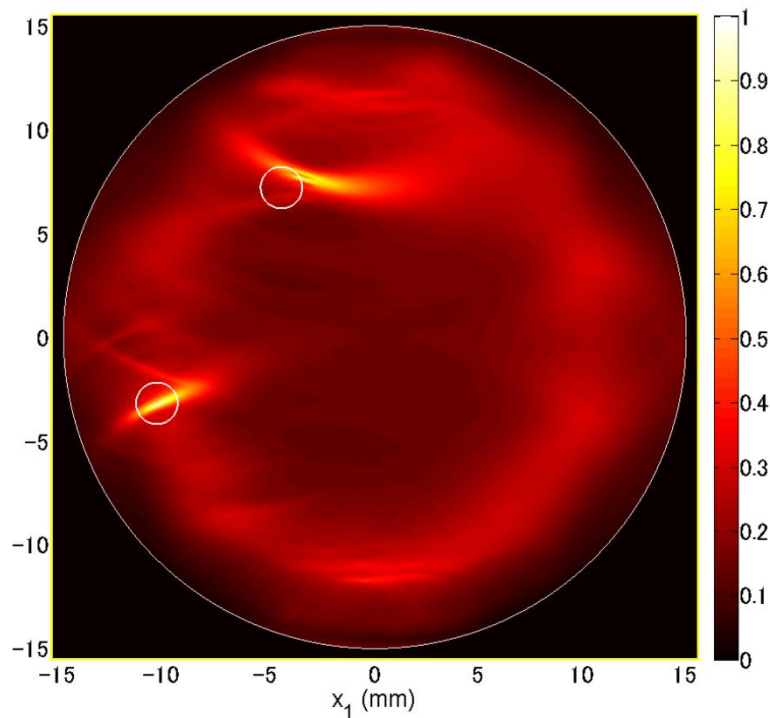
Figure 3.16 (Con't.) Case 2A results where both d_1 and d_2 are inside ER of T-mode.
 (a) Benchmark, MSSIM = 1; (b) two tests, MSSIM = 0.3508 and
 (c) four tests, MSSIM = 0.3231.

Results from case 2B where d_1 is inside the ER of L-mode, and d_2 is inside the ER of T-mode are shown in **Figure 3.17**. Superposed images from two and four sets of AWS-SAFT results are shown in **Figure 3.17(b)** and **(c)**, respectively. Another difference is that **Figure 3.17(b)** is a superposed image using L- and T-modes results, whereas, **Figure 3.17(c)** is a superposed image using only L-mode.

Using HVS, both SDHs are localized correctly by using only two sets of UTs with analysis results from L- and T-modes. By adding two more sets where transducers are on the left and right sides of a rod specimen, both SDHs are localized with the same accuracy as using two sets but twice the time-consuming. Evaluating by MSSIM, values for two and four tests are 0.2737 and 0.2787, respectively, hence the difference is 0.005. Difference in MSSIMs are remarkably small since image configuration of both results do not differ much comparing to the benchmark in **Figure 3.17(a)**.



(a)



(b)

Figure 3.17 Case 2B results where d_1 is inside ER of L-mode and d_2 is inside ER of T-mode; (a) Benchmark, MSSIM = 1; (b) two tests with L- and T-modes, MSSIM = 0.2737 and (c) four tests with L-mode only, MSSIM = 0.2787.

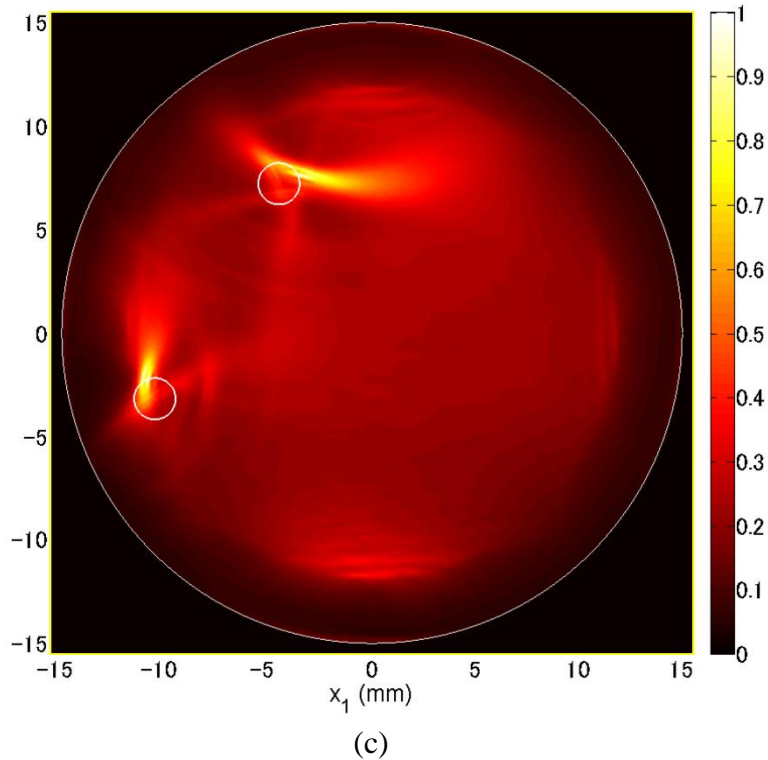


Figure 3.17 (Con't.) Case 2B results where d_1 is inside ER of L-mode and d_2 is inside ER of T-mode; (a) Benchmark, $MSSIM = 1$; (b) two tests with L- and T-modes, $MSSIM = 0.2737$ and (c) four tests with L-mode only, $MSSIM = 0.2787$.

From the results of step 2, two SDHs arranged in two different locations were imaged clearly using AWS-SAFT. Efficient way to use AWS-SAFT in imaging of a rod specimen with SDHs in arbitrary locations requires two step:

1. Conduct two tests, one where a PA is placed on the top and the another where a PA placed under the bottom
2. Obtain both L- and T-modes AWS-SAFT results, thus the ERs of L- and T-modes cover most region of a rod specimen.

Results from four sets of UTs were compared with two sets and it was observed that four sets were not necessary if AWS-SAFT was used following the above-mentioned way.

3.4 Summary

Objective II: To confirm the characteristics of AWS-SAFT

Performance of the AWS-SAFT was tested in fluid-solid two-phase media ultrasonic water immersion test of an aluminum rod specimens with an SDH in various locations. Characteristics of the AWS-SAFT were observed as follows:

Strong points

1. Improved ultrasound image can be obtained if SDH located inside the ER of either mode. Such improvement are (a) flaw image with narrower side lobes and (b) overall noise reduction.
2. Artifacts of L-mode which are normally observed in T-mode conventional SAFT image can be eliminated using the AWS-SAFT.
3. Noises outside the ER can be remarkably reduced.

Drawback: If SDH was located outside the ER, noises inside the ER would be highly amplified, hence the image of SDH became less clear.

Objective III: To propose an effective way to use AWS-SAFT

With the above-mentioned knowledge about strong points and drawback of the AWS-SAFT. An efficient way to use AWS-SAFT in imaging of a rod specimen with SDHs in arbitrary locations was proposed that it is required two steps as follows:

- Step 1: Conduct two sets of UTs, one where a PA is placed over the top and another where a PA is placed under the bottom of the specimen.
- Step 2: Obtain both L- and T-modes AWS-SAFT results so the superposition of ERs from both modes covers most region of a rod specimen.

The AWS-SAFT can improve the conventional SAFT if it is used with the consideration of ERs in a specific test configuration. Beam radiation model computed by AWS is a key to efficiently use AWS-SAFT, since it is required to plan the test so that ERs of either mode or the superposition of both modes cover the ROI of a target of inspection.

List of Publication for AWS-SAFT in fluid-solid water immersion ultrasonic test

Journal paper

1. Worawit Padungsriborworn, Akira Furukawa, Sohichi Hirose: Improvement of SAFT by Implementation of Approximate Wave Solution in Fluid-Solid Two-Phase Media: A Case Study on Imaging of Aluminum Rod with Side-Drilled Holes, Journal of Nondestructive Evaluation 34:15, May.2015.

Domestic conferences

- I. Worawit Padungsriborworn, Akira Furukawa, Sohichi Hirose: Approximated Wave Solution based Imaging of Rod by Water Immersion Ultrasonic Test, Proceedings of the 21st Symposium on Ultrasonic Testing, pp.21-22, Jan.2014.
- II. Worawit Padungsriborworn, Akira Furukawa, Sohichi Hirose: Improvement of SAFT by Considering Ultrasonic Wave Propagating Characteristics and Imaging of Rod by Water Immersion Test, Proceedings of the JSNDI Spring conference 2014, pp.11-12, Jun.2014.
- III. Worawit Padungsriborworn, Akira Furukawa, Sohichi Hirose: Improvement of SAFT in Ultrasound Imaging of Two-Phase Media, The 7th Thailand-Japan International Academic Conference 2014, Nov.2014.
- IV. Worawit Padungsriborworn, Akira Furukawa, Sohichi Hirose: Decisive Assessment of Effective Region for Flaw Detection in Ultrasound Imaging by AWS-SAFT, Proceedings of the 22nd Symposium on Ultrasonic Testing, pp.1-4 ,Jan.2015.

Chapter 4: *Application of AWS-SAFT in angle beam ultrasonic test*

In this chapter, the performances of the proposed AWS-SAFT is further investigated in solid-solid two solid media. The significance of Effective Region (ER) computed by AWS was observed in the previous chapter as a potential way to determine effective imaging region in ROI. Experimental setup which is typical for all cases is firstly explained in section 4.1. Experiment is organized in three sections: Section 4.2 explains the characteristics of AWS-SAFT in solid-solid two solid media case. Section 4.3 explains ER technique followed by its verification. Section 4.4 demonstrates the use of AWS-SAFT and ER technique in a case study of imaging the steel plate with bottom defect. Summary of this chapter is given in section 4.5.

4.1 Experimental setup

All ultrasonic tests in this chapter are performed using a 32 channels linear phased-array transducer (PA) with main frequency of 5 MHz produced by KGK (Kanagawa, Japan) as shown in **Figure 4.1**. Element size is 0.4 mm×10.0 mm aligned with the pitch of 0.5 mm between adjacent elements. Angle adjustable wedge with the range of $\theta_{PA} = 0\sim 60^\circ$, produced from Polystyrene is attached to the PA. Pulser-receiver JPR-600C produced by Japan Probe (Japan) as shown in **Figure 4.2** is used. It can generate pulses with the main frequency of 5 MHz. Wave data is acquired using control software from the same maker. Sampling frequency is 50 MHz with 16 times averaging to get stabilized signals. No gain is added in order to suppress noises to minimum level.

Steel plate specimen has a size of 100 mm×500 mm×21.5mm. Two SDHs of diameter 1.5 mm are processed into the specimen at two different depths. Typical setup of experiment is shown in **Figure 4.3**. L- and T-modes wave velocities in Polystyrene (PS) are 2300 m/s and 1140 m/s, respectively, where they are 5938 m/s and 3240 m/s for a steel specimen. All waveform data are recorded as 2000 discrete points with time interval of 0.02 μ s. Delay time is set to 15 μ s in order to minimize data length while first reflection from the interface and farthest T-mode reflection inside ROI can still be recorded.

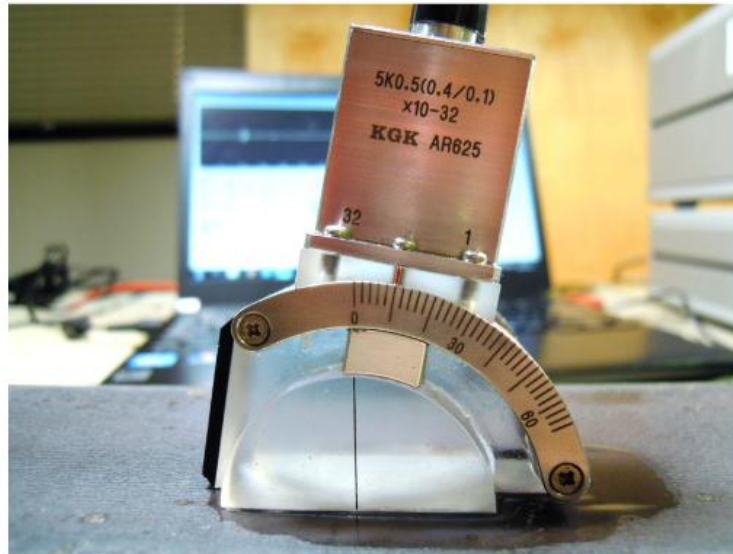


Figure 4.1 32-channels phased-array transducers with PS wedge.



Figure 4.2 Pulser-receiver system.

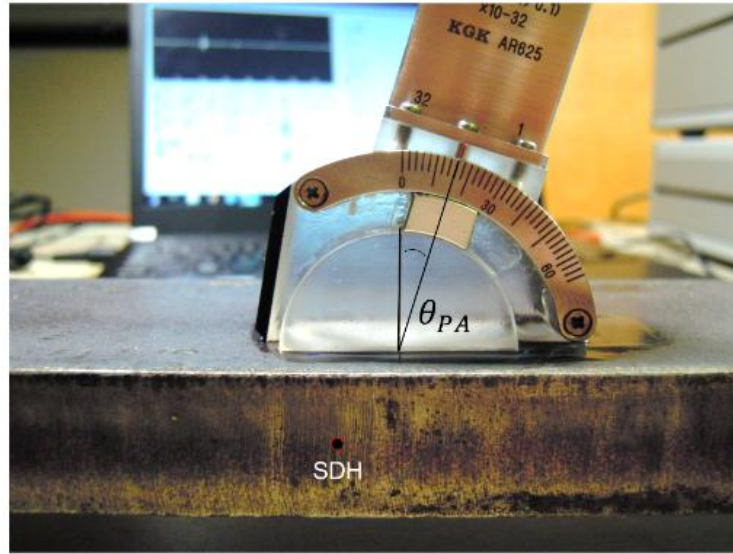


Figure 4.3 Typical setup for experiments in this Chapter.

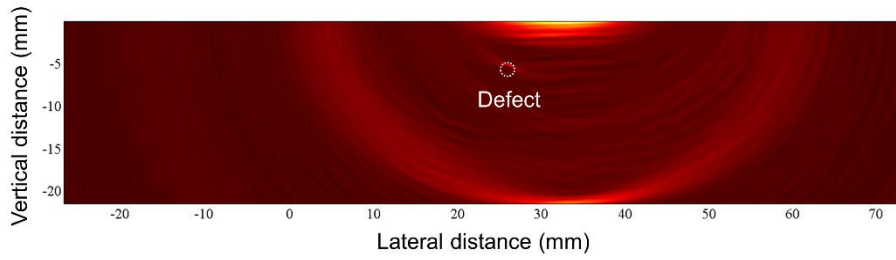
4.2 Characteristics of AWS-SAFT

This section demonstrates the ultrasound imaging by AWS-SAFT and describes its characteristics using the experimental results from the two cases explained in section 2.3.2 in chapter 2. Outline of experiment is shown in **Figure 2.14**. Gain was set to zero in all cases to minimize noises and averaging was taken at the rate of 16 times to get stabilized signals.

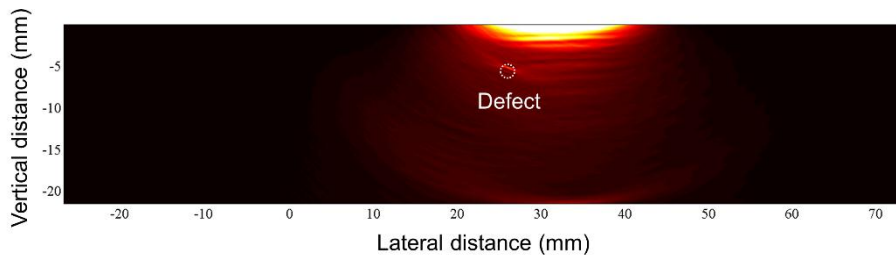
For L-mode case where θ_{PA} is set to 16° , ultrasound images from conventional SAFT and AWS-SAFT are shown in **Figure 4.4(a)** and **(b)**, respectively. Defect image is reconstructed correctly by both SAFT and AWS-SAFT. In AWS-SAFT image, noises in the region where intensities of ultrasonic beam radiation are low are mostly suppressed making the defect image reconstruction much more clearly from the background noises than in SAFT. However, reflection from the interface is very strong in L-mode, hence the pixel value over region closed to the interface was highly amplified.

Considering T-mode where θ_{PA} is set to 38° , ultrasound images from conventional SAFT and AWS-SAFT are shown in **Figure 4.5(a)** and **(b)**, respectively. Defect image is also reconstructed correctly by both SAFT and AWS-SAFT. In SAFT image, artifacts resulting from bottom echoes and its multiple reflection of L-mode ultrasonic wave can be observed at various locations. This may mislead the justification

of engineer and inspector in evaluating the defect position. By using AWS-SAFT, these artifacts can be screened out by the applied ultrasonic beam radiation, thus they are eliminated from the results. Similar to L-mode, noises in the region where intensities of ultrasonic beam radiation are low are mostly suppressed. However, pixel values over the region closed to the interface are highly amplified.

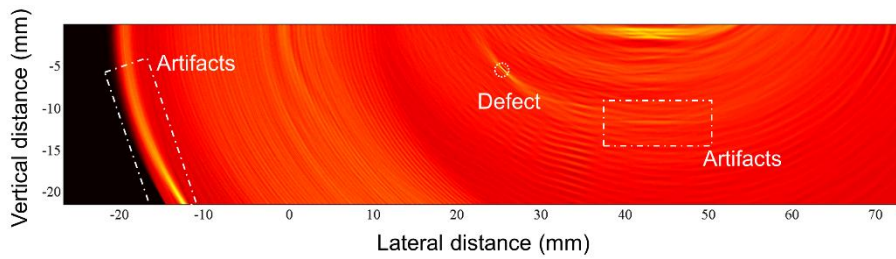


(a)

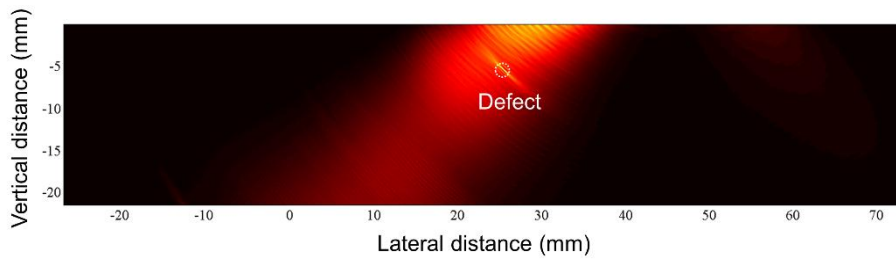


(b)

Figure 4.4 L-mode experimental result; (a) SAFT and (b) AWS-SAFT.



(a)



(b)

Figure 4.5 T-mode experimental result; (a) SAFT and (b) AWS-SAFT.

4.3 ER technique and AWS-SAFT

Considering results in section 4.2, it is obvious that AWS-SAFT can boost up resolution of defect image reconstruction over the region where intensities of ultrasonic beam radiation are high. Such region will be called an Effective Region (ER) and will be defined and explained in this section.

4.3.1 Effective Regions for each wave mode of AWS-SAFT

Intensity of ultrasonic beam radiation in a test medium from a specific transducer, can be approximated from normalized magnitude of displacement in **Equation 2.18** which can be expressed as $|\mathbf{u}|(\rho_1 c_{L,1}^2)/(ap_0)$, where a is the width of the array element. When producing an ultrasound image by AWS-SAFT, and also the conventional SAFT, phased-array transducer consisting of many elements separated by channels is normally used. Therefore, it is necessary to approximate the trend of ultrasonic beam radiation when all channels are occupied. These concept can be demonstrated by using $\sum_{i=1}^n |u_i^y(\mathbf{b}, \omega)|$, where non-dimensional displacements are used, to predict the trend of ultrasonic beam radiation when all channels are used, separately. Considering **Equation 2.18**, pressure acting over the transducer surface p_0 shall be fixed since altering this parameter will affect the magnitude of AWS displacement. Model of ultrasonic beam radiation using the summation of all available channels $\sum_{i=1}^n |u_i^y(\mathbf{b}, \omega)|$ will be called *Approximate Beam Radiation (ABR)*.

ABR for a 32 channel PA which is used throughout this dissertation is shown in **Figures 4.6** and **4.7** for L-mode ($\theta_{PA} = 16^\circ$) and T-mode ($\theta_{PA} = 38^\circ$), respectively. These angles are chosen empirically since they provide high ABR intensities for this experimental setup. Contour lines are marked with equally spaced intervals of 0.025. Regions between different contour lines are governed by different ABR intensities which means ultrasonic wave do propagates through different regions with different ultrasonic wave intensities. It is assumed that the region with higher ABR intensity tends to have higher flaw imaging capability than the lower one. In other words, defect exists inside the higher ABR region is predicted to be reconstructed more clearly than inside the lower ABR.

Here, we define *Effective Region (ER)* as a region with the ABR intensity over a certain threshold value, where a flaw can be imaged properly, governed by a known PA

location and a geometry of the test medium. In the following section, a proper threshold of ABR intensity is determined experimentally to find a reasonable ER.

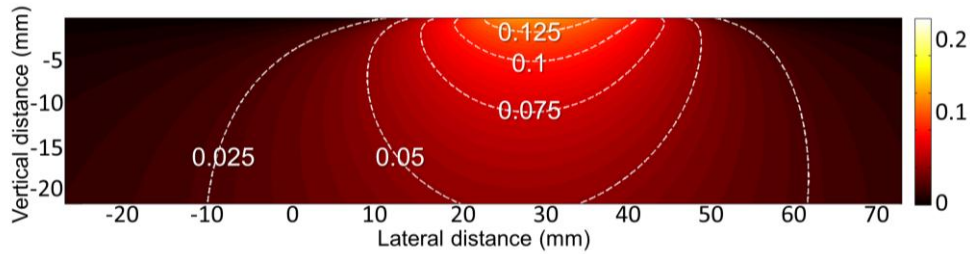


Figure 4.6 L-mode ABR using $\theta_{PA} = 16^\circ$.

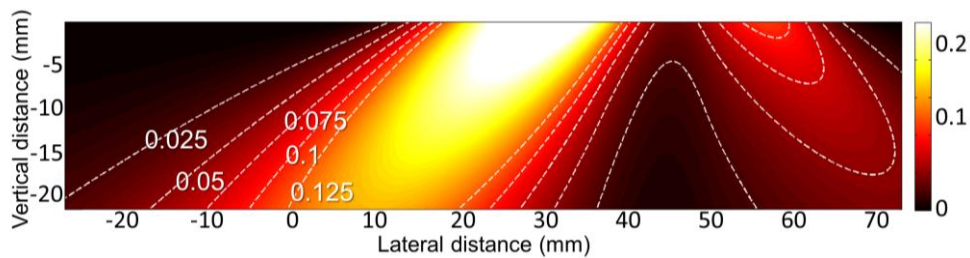


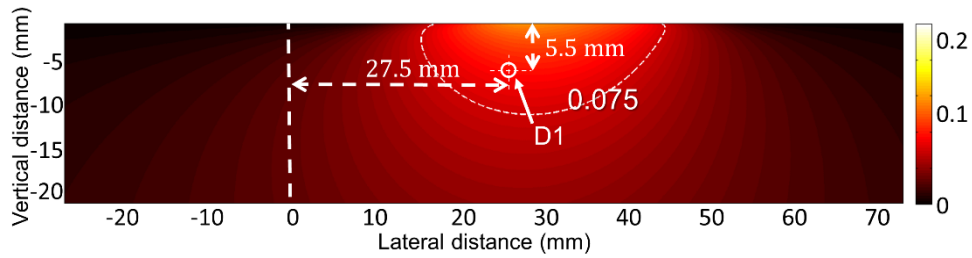
Figure 4.7 T-mode ABR using $\theta_{PA} = 38^\circ$.

4.3.2 Experimental verification of ER technique

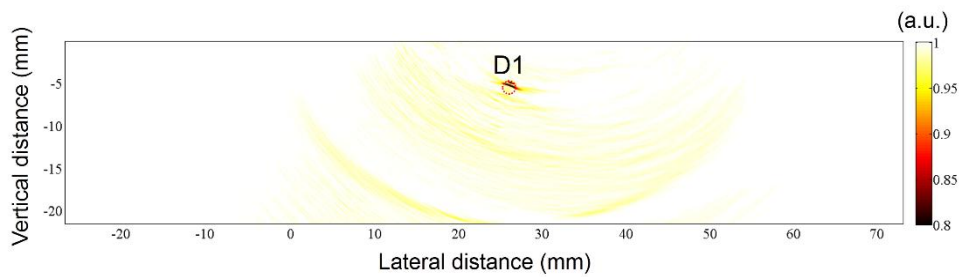
The objective of this section is to verify ER defined in section 4.3.1. Experiments are separated into case-L for L-mode using $\theta_{PA} = 16^\circ$, and case-T for T-mode using $\theta_{PA} = 38^\circ$. This paper uses Structural SIMilarity (SSIM) index, which is explained in the **Appendix A**, as a supporting aid in viewing the results. SSIM can help in identifying differences between two images. Therefore, if result from non-defective specimen is available, this technique can be used to clearly boost the defect image from other mutual echoes such as interface and bottom echoes or even background noises. Detail on this method is explained in the **Appendix A**, together with mathematical expressions of SSIM index. A plot of differences between two images is called an SSIM index map, thus it will be simply called an SSIM-MAP.

All experiments introduced in this section are used to find out the smallest value of ABR intensity χ , that can be used as a cutoff value in determination of the ER. Considering **Figure 4.8(a)** for case-L1, SDH D1 is located inside the region where $\chi > 0.075$. If such region can be defined as ER, D1 shall be reconstructed clearly. SSIM-MAP

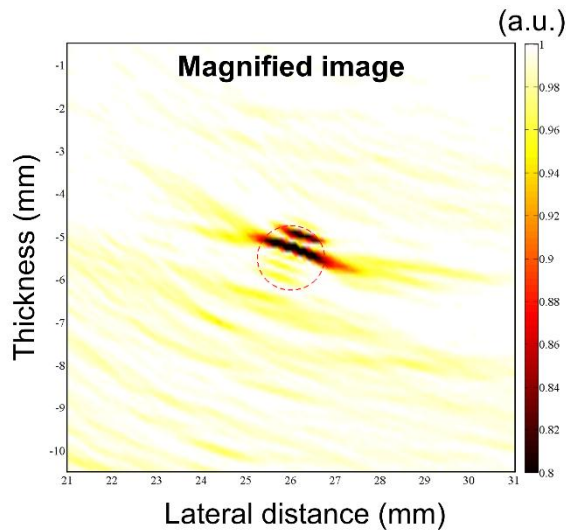
is shown in **Figure 4.8(b)** where D1 is clearly reconstructed with high resolution; means that image of D1 can be distinguished from background very easily. Magnified image is shown in **Figure 4.8(c)** to show that defect reconstruction is very clear. As a result, region where $\chi > 0.075$ can be used as ER. However, it is probably not the smallest value yet, thus next case will try with $\chi = 0.05$.



(a)



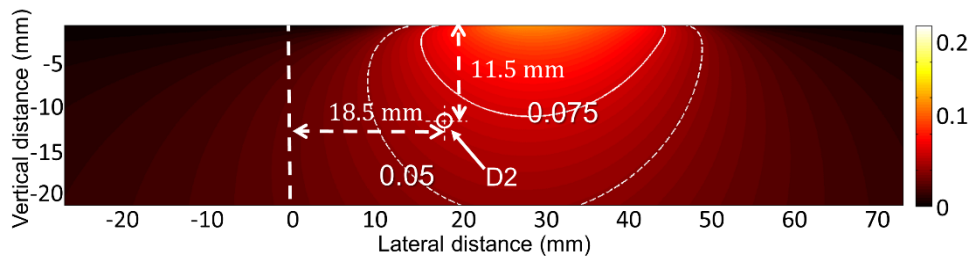
(b)



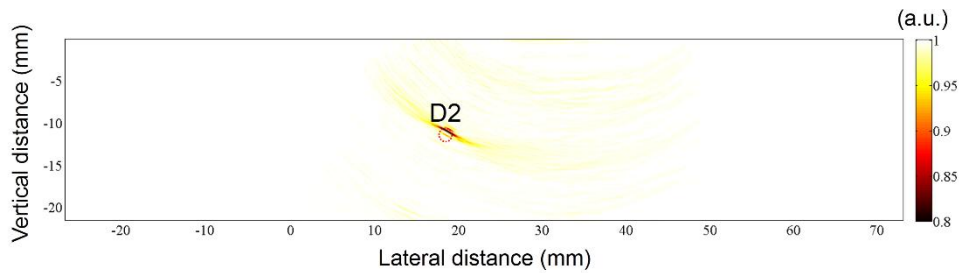
(c)

Figure 4.8 Case-L1 results testing $\chi = 0.075$;
(a) Outline, (b) SSIM-MAP and (c) Magnified SSIM-MAP.

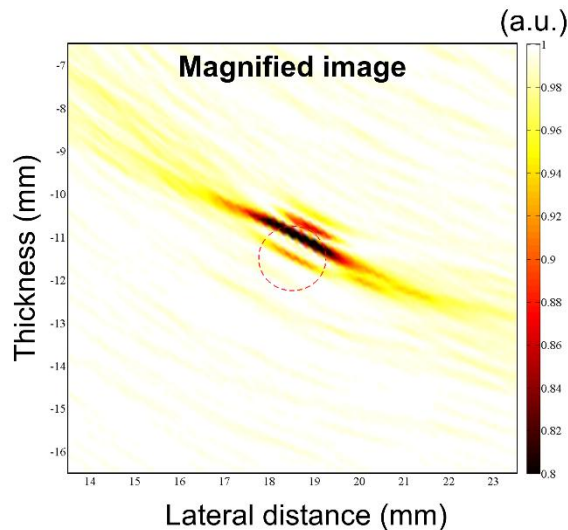
Considering **Figure 4.9(a)** for case-L2, SDH D2 is located inside region where, $0.05 < \chi < 0.075$. If $\chi = 0.05$ can be used as cutoff value for ER, D2 shall be reconstructed clearly. SSIM-MAP is shown in **Figure 4.9(b)** where D2 is clearly reconstructed with high resolution. Magnified image is shown in **Figure 4.9(c)** to prove that defect reconstruction was very clear. As a result, region where $\chi > 0.05$ can be used as ER. By the way, it is probably not the smallest value yet, hence next case will try using $\chi = 0.025$.



(a)



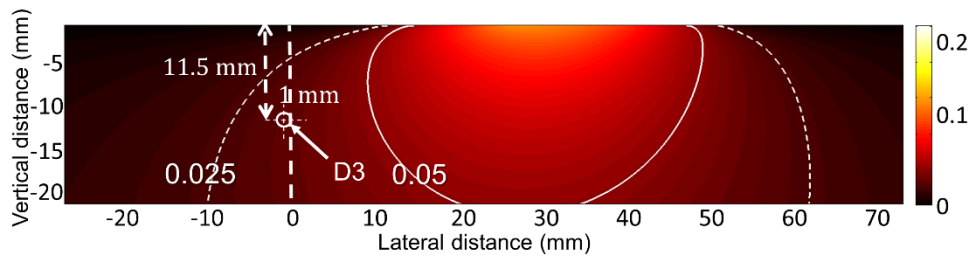
(b)



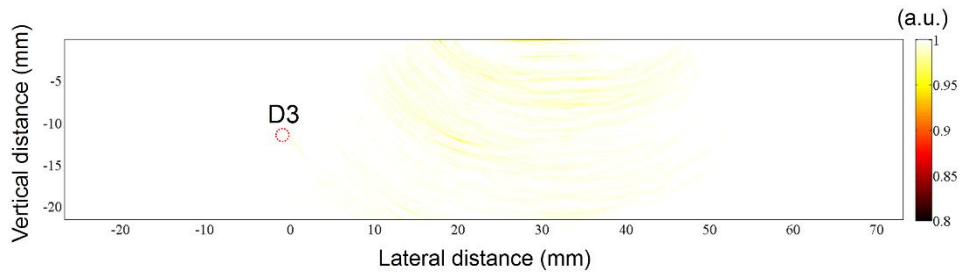
(c)

Figure 4.9 Case-L2 results testing $\chi = 0.05$;
 (a) Outline, (b) SSIM-MAP and (c) Magnified SSIM-MAP.

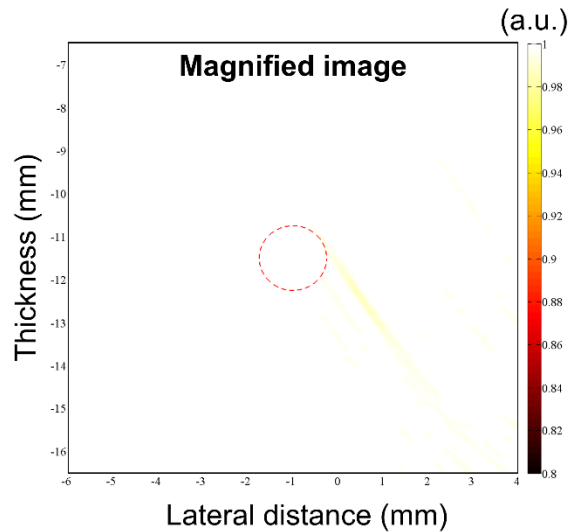
Figure 4.10(a) shows results from case-L3 where SDH D3 is located inside region where, $0.025 < \chi < 0.05$. If $\chi = 0.025$ can be used as cutoff value for ER, D3 shall be reconstructed clearly. SSIM-MAP is shown in **Figure 4.10(b)** where D3 cannot be observed. Magnified image is shown in **Figure 4.10(c)** to confirm that defect was not reconstructed. As a result, region where $0.025 < \chi < 0.05$, cannot be used as ER. Therefore, $\chi = 0.05$ is selected as cutoff value for ER in L-mode.



(a)



(b)



(c)

Figure 4.10 Case-L3 results testing $\chi = 0.025$;
(a) Outline, (b) SSIM-MAP and (c) Magnified SSIM-MAP.

ER for T-mode will be verified using the same method as L-mode. Considering **Figure 4.11(a)** for case-T1, SDH D1 is located inside region where $\chi > 0.125$. If such region can be defined as ER, D1 shall be reconstructed clearly. SSIM-MAP is shown in **Figure 4.11(b)** where D1 is clearly reconstructed with high resolution. Magnified image is shown in **Figure 4.11(c)** to show that reconstruction of defect was very clear. As a result, region where $\chi > 0.125$ can be used as ER. However, it is probably not the smallest value yet, thus next case will try with $\chi = 0.1$.

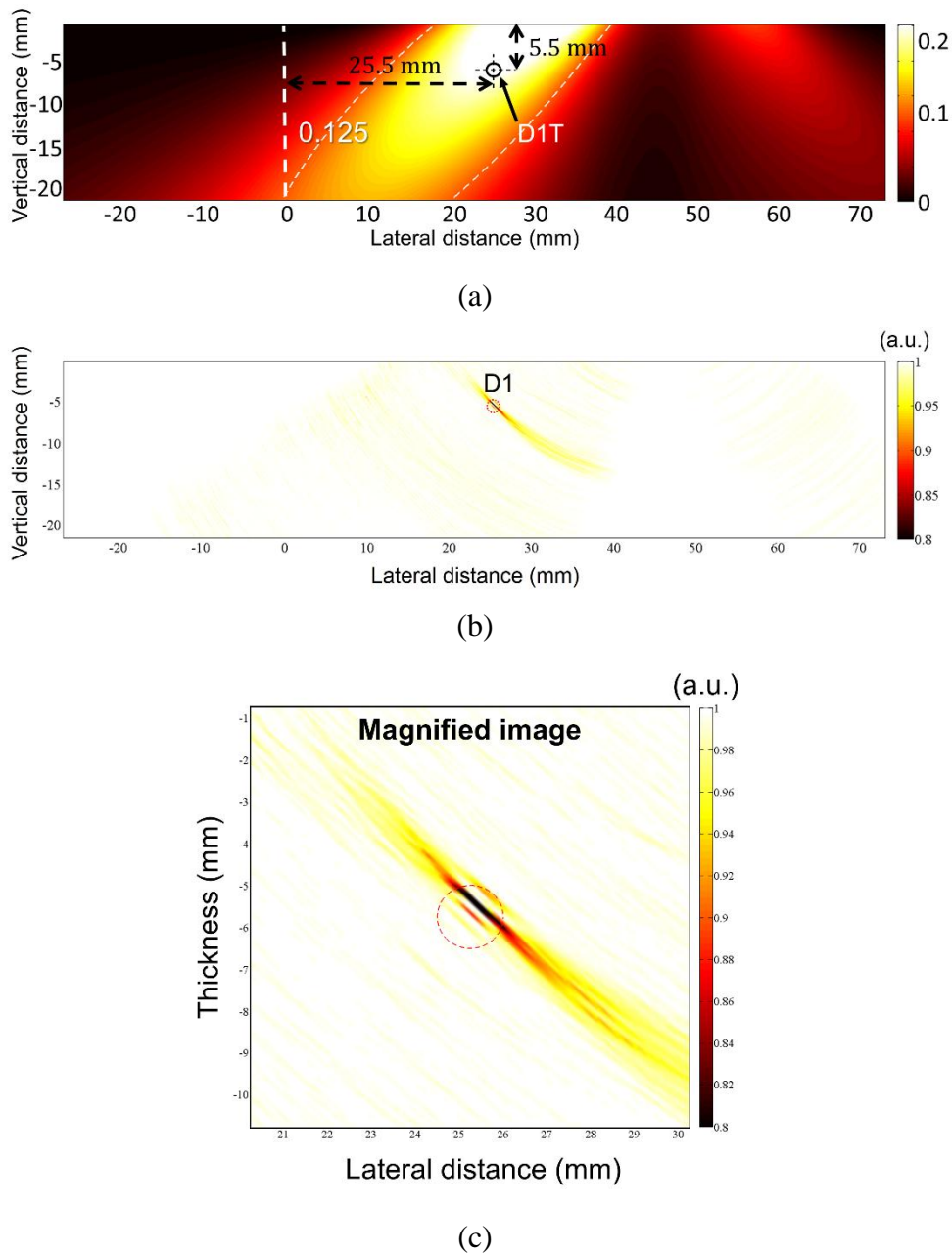
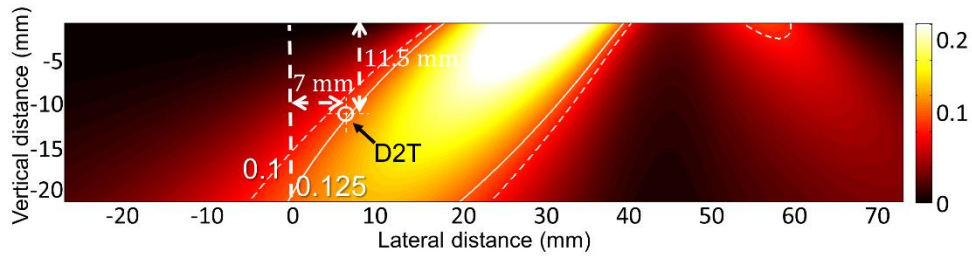
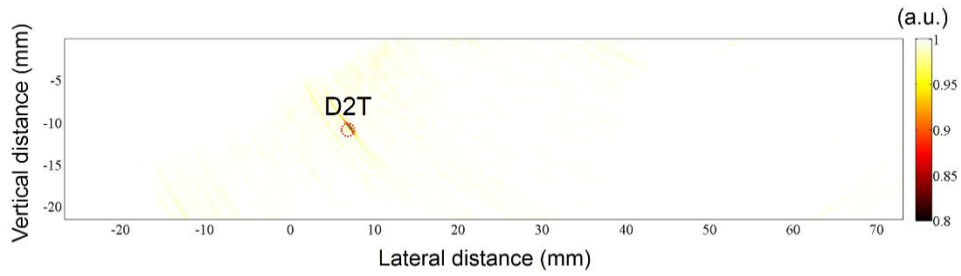


Figure 4.11 Case-T1 results testing $\chi = 0.125$;
 (a) Outline, (b) SSIM-MAP and (c) Magnified SSIM-MAP.

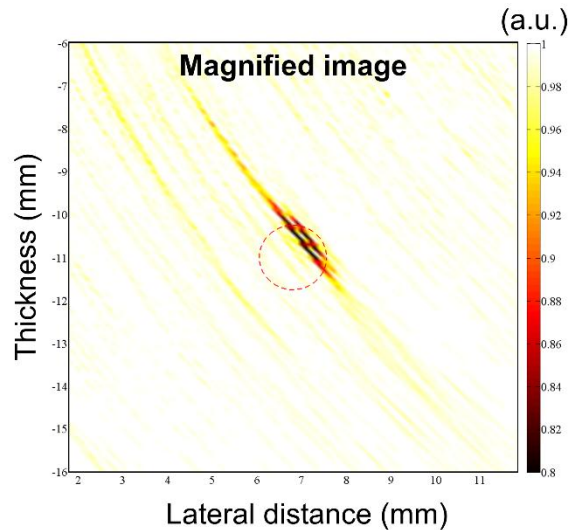
Figure 4.12(a) shows outline of case-L2 where SDH D2T is located inside region where, $0.1 < \chi < 0.125$. If $\chi = 0.1$ can be used as cutoff value for ER, D2T shall be reconstructed clearly. SSIM-MAP is shown in **Figure 4.12(b)** where D2T is clearly reconstructed with high resolution. Magnified image is shown in **Figure 4.12(c)** to prove that defect reconstruction was very clear. As a result, region where $\chi > 0.1$ can be used as ER. By the way, it is probably not the smallest value yet, hence next case will try using $\chi = 0.05$.



(a)



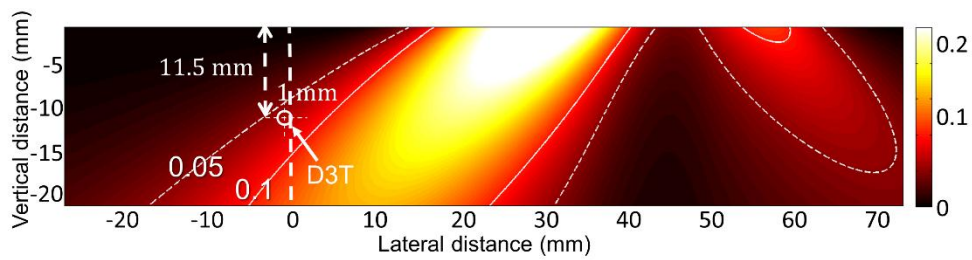
(b)



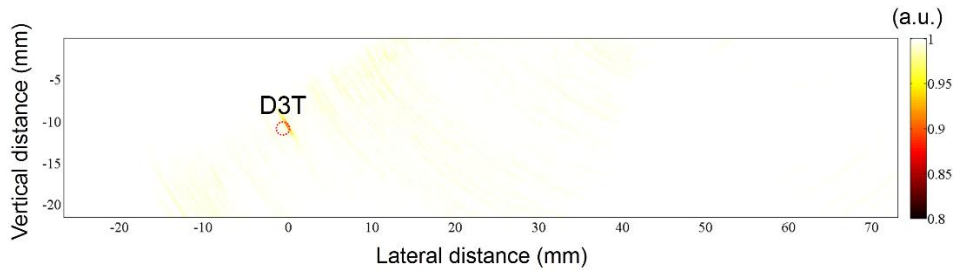
(c)

Figure 4.12 Case-T2 results testing $\chi = 0.1$;
(a) Outline, (b) SSIM-MAP and (c) Magnified SSIM-MAP.

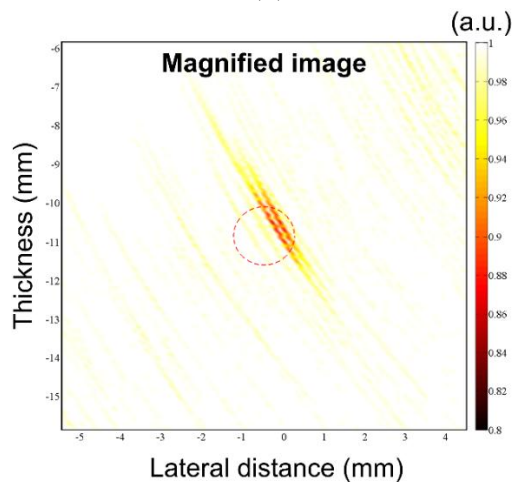
Outline of case-T3 is shown in **Figure 4.13(a)** where SDH D3T is located inside region where, $0.05 < \chi < 0.1$. If $\chi = 0.05$ can be used as cutoff value, D3T shall be reconstructed clearly. SSIM-MAP is shown in **Figure 4.13(b)** where D3T is reconstructed. Location of defect can still be precisely identified. However, reconstruction of defect is not as clear as in case-T1 and T2. Magnified image is shown in **Figure 4.13(c)** to show that defect was precisely reconstructed. As a result, region where $\chi > 0.05$ can be used as ER. However, $\chi = 0.05$ may not be the smallest value yet to determine ER, thus next case will try on $\chi = 0.025$.



(a)



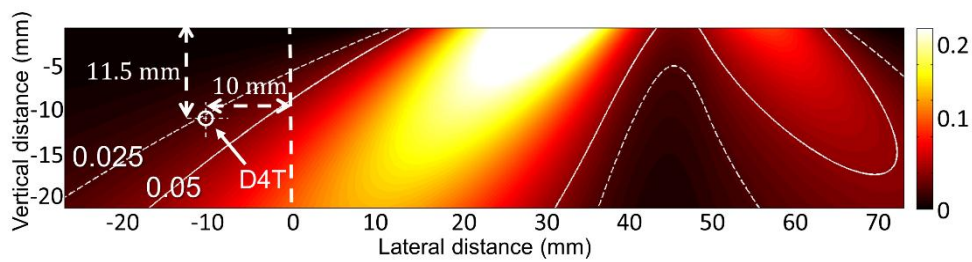
(b)



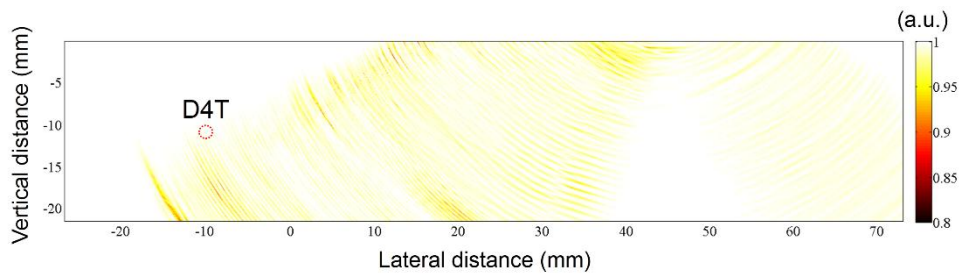
(c)

Figure 4.13 Case-T3 results testing $\chi = 0.05$;
 (a) Outline, (b) SSIM-MAP and (c) Magnified SSIM-MAP.

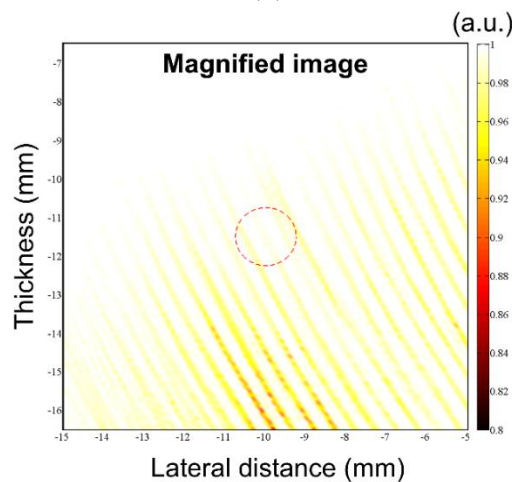
Figure 4.14(a) shows outline of case-T4 where SDH D4T is located inside region where, $0.025 < \chi < 0.05$. If $\chi = 0.025$ can be used as cutoff value, D4T shall be reconstructed clearly. SSIM-MAP is shown in **Figure 4.14(b)** where defect image is not observed. Magnified image is shown in **Figure 4.14(c)** to confirm that defect was not reconstructed. Only patterns similar to ABR computed from AWS can be observed as a result from amplification of background noises. Therefore, region where, $0.025 < \chi < 0.05$, cannot be used as ER. Finally, $\chi = 0.05$ is selected as cutoff value for ER and it is the same value confirmed in L-mode.



(a)



(b)



(c)

Figure 4.14 Case-T4 results testing $\chi = 0.025$;
 (a) Outline, (b) SSIM-MAP and (c) Magnified SSIM-MAP.

According to the results from this section, it can be implied that ERs in both L- and T-mode are regions where intensities of ABR are greater than 0.05. In L-mode, ER is the region underneath the transducer where it is the inclined regions at approximately $\pm 45^\circ$ directions in T-mode. L- and T-modes are effective in different ER, hence it is very useful to know those regions so appropriated mode can be selected for any test configurations. Next section will be used to demonstrate an application of ER technique in a case study on steel plate bottom defect.

4.4 A case study: Imaging of steel bottom defect

ER technique was introduced and verified in section 4.3. This section aims to apply such principle to a case study originated from fracture of truss member embedded inside concrete slab, at the Kisogawa bridge (Mie prefecture, Japan). Section 4.4.1 first explain the outline of studied case. Then, experimental setup is explained in section 4.4.2, followed by the results. Additional results are shown in section 4.4.3 as examples for circular and triangular flaw shapes.

4.4.1 Outline of studied problem and experimental setup

Truss fracture accident at Kisogawa bridge occurred in June 2007. Photos of the bridge and its fractured part are shown in **Figure 4.15** [4.2, 4.3]. Corrosion of the steel truss had been progressing inside the concrete slab, thus it could not be detected until it fractured. This emerged a demand to find the way in early detection of defect inside regions which are difficult to inspect with conventional NDT methods.

This dissertation attempts to use the AWS-SAFT and the ER technique in early detection of such defect because of the following two reasons: AWS-SAFT improved SAFT in a way that T-mode result can be used without artifacts. ER technique can be used to predict the region in ROI where defect shall be reconstructed, definitely. However, it would be too complicated if first attempt is applied with actual concrete embedded truss member. This leads to a simplification of actual problem by using the model on the right of **Figure 4.16**, where concrete is imitated by an inspection limit. Parameter L is defined as distance from the front edge of PS wedge to the front edge of rectangular defect. A long rectangular notch with the size of 20 mm \times 5 mm is processed onto the steel plate bottom surface to imitate corrosion. Objective of this study is to find the most farthest distance L where such artificial defect can still be detectable. All devices and materials

used in this section are similar to those in section 4.2, 4.3 and typical setup of experiment in this section is shown in **Figure 4.17**.

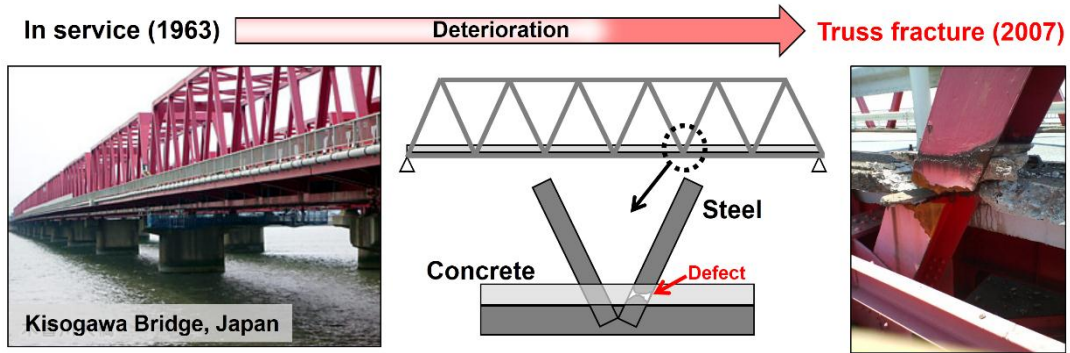


Figure 4.15 Photo and illustration of Kisogawa bridge case.

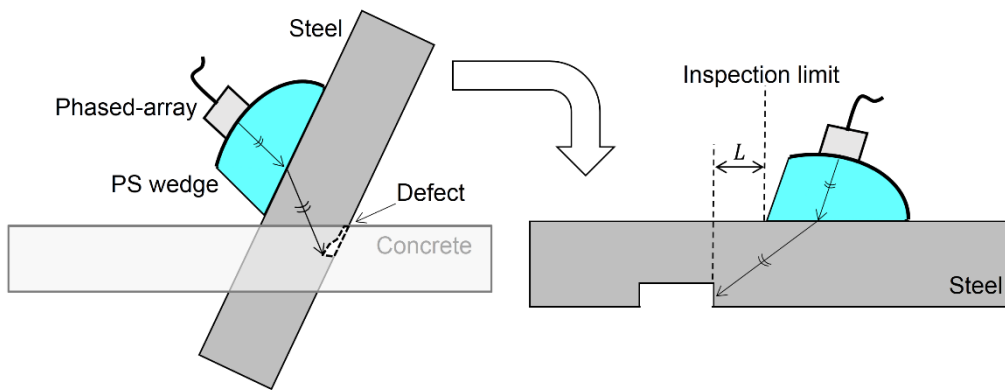


Figure 4.16 Simplified model used in this study.

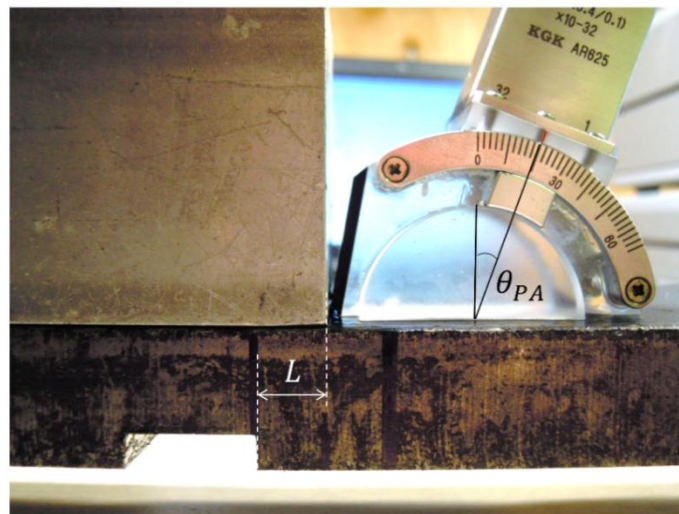


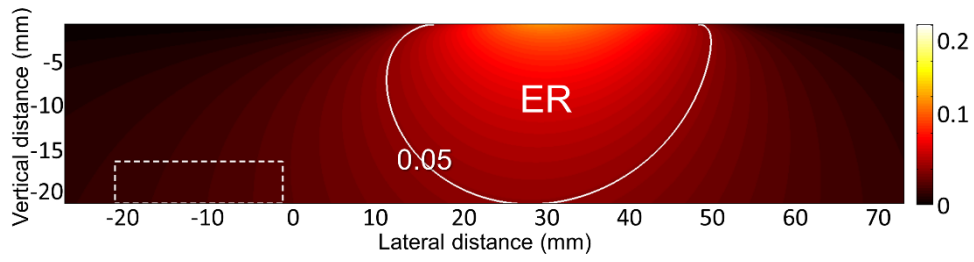
Figure 4.17 Typical setup of experiment in this section.

4.4.2 Experimental results

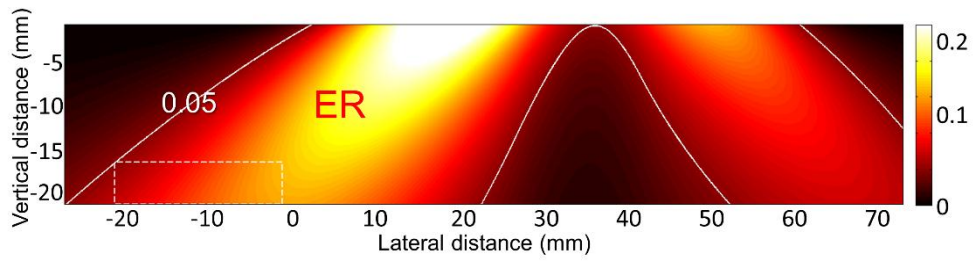
According to results in section 4.3, cutoff value of ABR intensity used to determine ER is 0.05 and if defect existed inside ER, it shall be reconstructed clearly. ER technique will be applied here, hence before performing an ultrasound imaging of specified test volume with a selected transducer, ER shall be computed in order to check the effective imaging region. Experiments are done as 3 cases using $L = 1$ mm, 10 mm and 20 mm and ultrasound image results are shown using SSIM-MAP as explained in Appendix A.

First, in case-1 where $L = 1$ mm, θ_{PA} is selected empirically as 20° and ER in L-mode is shown in **Figure 4.18(a)**. In this case, rectangular notch defect, represented by dashed lines, is outside the ER hence it is considered impossible to reconstruct such defect with L-mode in this configuration based on ER technique. ER of T-mode is shown in **Figure 4.18(b)**. In this case, ER can cover the defect thus it is predicted to be reconstructed clearly according to ER technique. Therefore, T-mode is considered the appropriated wave mode for this problem.

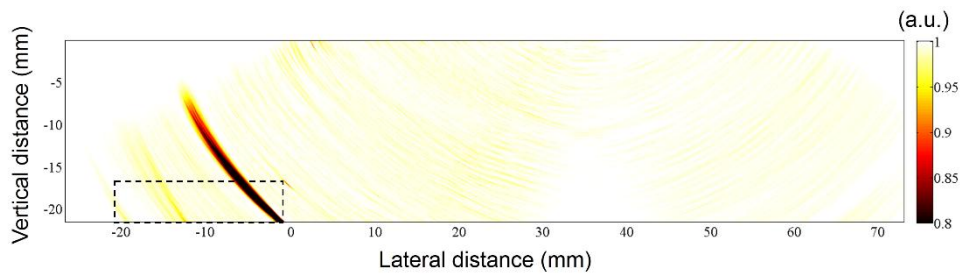
Experimental result using SSIM-MAP from T-mode AWS-SAFT is shown in **Figure 4.18(c)**. Right corner of the defect is reconstructed clearly, and even the top-right corner of defect can be imaged as seen in **Figure 4.18(d)**, hence the depth of notch can be precisely determined using location of top-right and bottom-right corners of reconstructed defect. Result proved the effectiveness of using ER technique in checking the high imaging capability region inside ROI. It can be known here that in case of $L = 1$ mm, steel bottom defect can be clearly reconstructed.



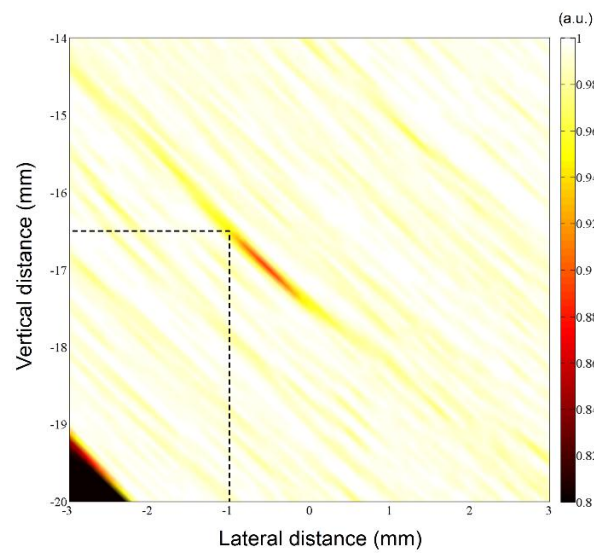
(a)



(b)



(c)



(d)

Figure 4.18 Case-1: $L = 1$ mm;

(a) L-mode ER, (b) T-mode ER (c) T-mode SSIM-MAP and (d) Zoomed SSIM-MAP

Case-2 is conducted to check the situation where L is shifted by 10 mm, θ_{PA} is fixed at 20° and ER in T-mode is shown in **Figure 4.19(a)**. In this case, defect is still inside the ER thus it shall be reconstructed clearly. Experimental result is shown in **Figure 4.19(b)**. Right corner of the defect is detected clearly. In this configuration, the top-right edge of defect was not reconstructed so the depth of notch cannot be determined. However, it still proved the effectiveness of ER technique in checking the region inside ROI where defect image can definitely be reconstructed. Case-2 result shows that in case of $L = 10$ mm, steel bottom defect can still be reconstructed, clearly.

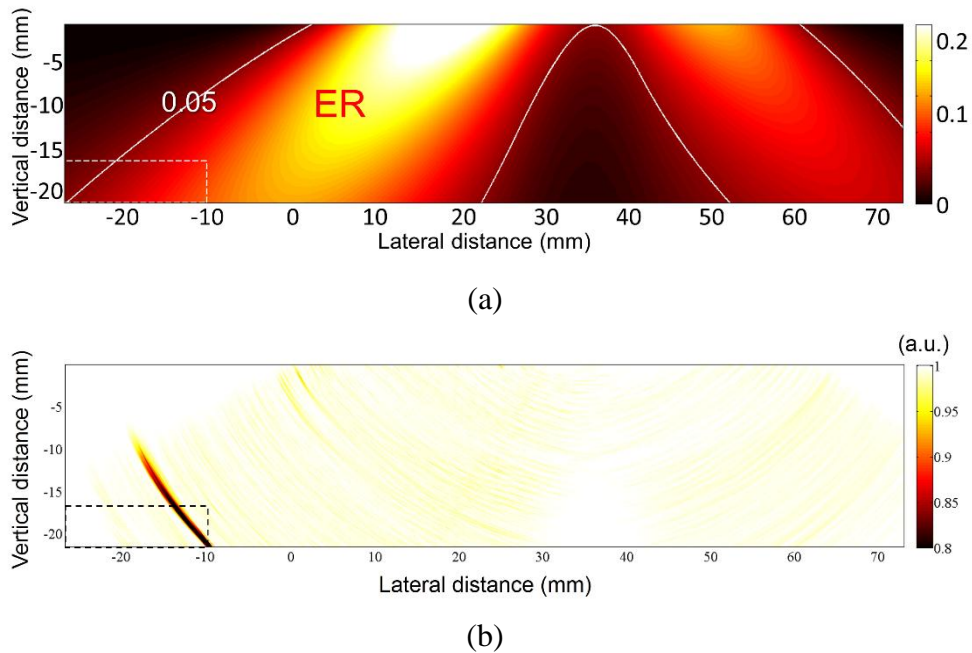


Figure 4.19 Case-2: $L = 10$ mm T-mode; (a) ER and (b) SSIM-MAP.

In case-3, L is shifted to 20 mm while θ_{PA} is still fixed at 20° . T-mode ER is shown in **Figure 4.20(a)** and it can be observed that right corner of the defect is still inside the ER, hence it shall be reconstructed clearly. Experimental result is shown in **Figure 4.20(b)**. In this case, right corner of the defect can still be reconstructed, clearly. However, the intensity of defect image is dropped than in case-1 and 2 but it still clear. This proves the effectiveness of ER technique in checking the effective region inside ROI where defect image can surely be reconstructed. Case-3 result ensures that in case of $L = 20$ mm, steel bottom defect can still be reconstructed, clearly.

Considering **Figure 4.20(a)** again, it L is shifted to 30 mm, defect will be outside the ER so it cannot be reconstructed with this configuration. Therefore, this paper stopped the investigation for farthest L and concludes that it is 20 mm for this configuration.

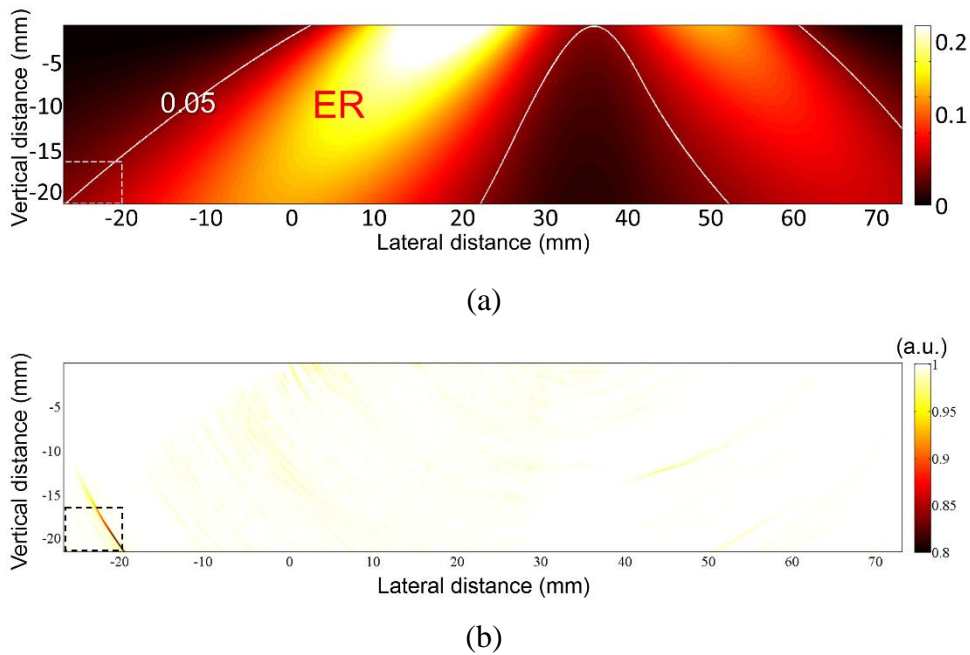


Figure 4.20 Case-3: $L = 20$ mm T-mode; (a) ER and (b) SSIM-MAP.

4.4.3 Additional results

Actual corrosion can be considered as a mixture of various geometries which are rectangular, circular and triangular. Two cases are introduced here to check the flaw detectability in case of circular and triangular notch, which wave scattering characteristics are different from the rectangular one. The two experiments are done in the same manner with rectangular notch. $\theta_{PA} = 20^\circ$, and $L = 1$ mm, where the flaw imaging capability is the highest from three cases in section 4.4.2, using the ER technique.

Considering **Figure 4.21(a)**, the circular notch is inside the ER, hence it shall be reconstructed clearly. Experimental result is shown in **Figure 4.21(b)**. In this case, right side of the circular notch can be reconstructed clearly, however, the circular shape of the flaw cannot be known.

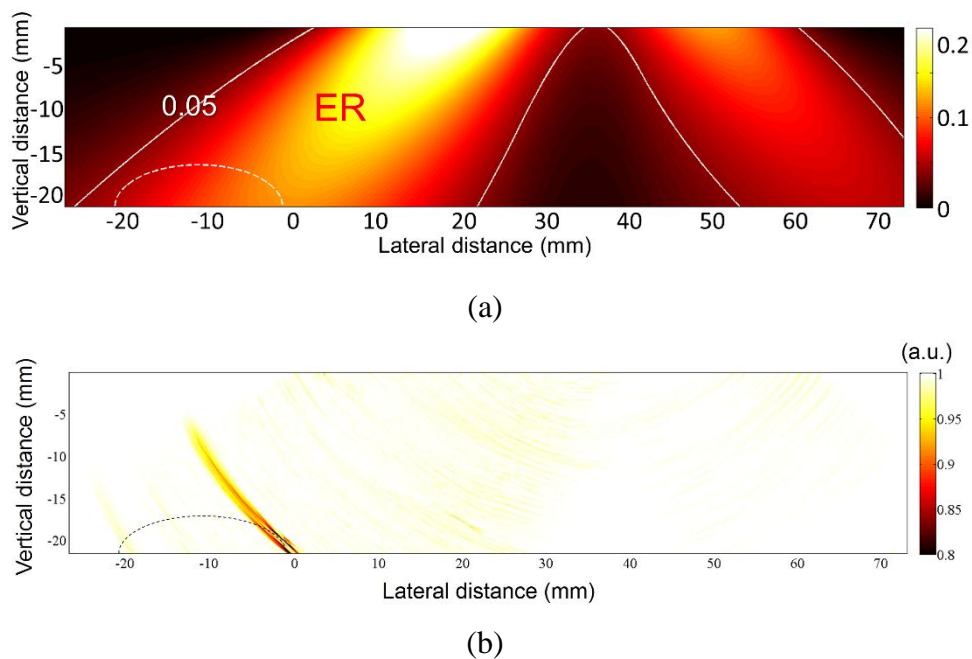


Figure 4.21 Circular notch: $L = 1$ mm T-mode; (a) ER and (b) SSIM-MAP.

ER for a case of triangular notch is shown in **Figure 4.22(a)**, the triangular notch is inside the ER hence it shall be reconstructed clearly, based on ER technique. Experimental result is shown in **Figure 4.22(b)**. In this case, no flaw image can be observed. It can be considered from such flaw shape that the ultrasonic waves propagated to the side of the flaw and reflected away to another side so the PA cannot receive the scattered waves. This demonstrate the case that ER technique is not efficient and will be noted as the limitation of this method.

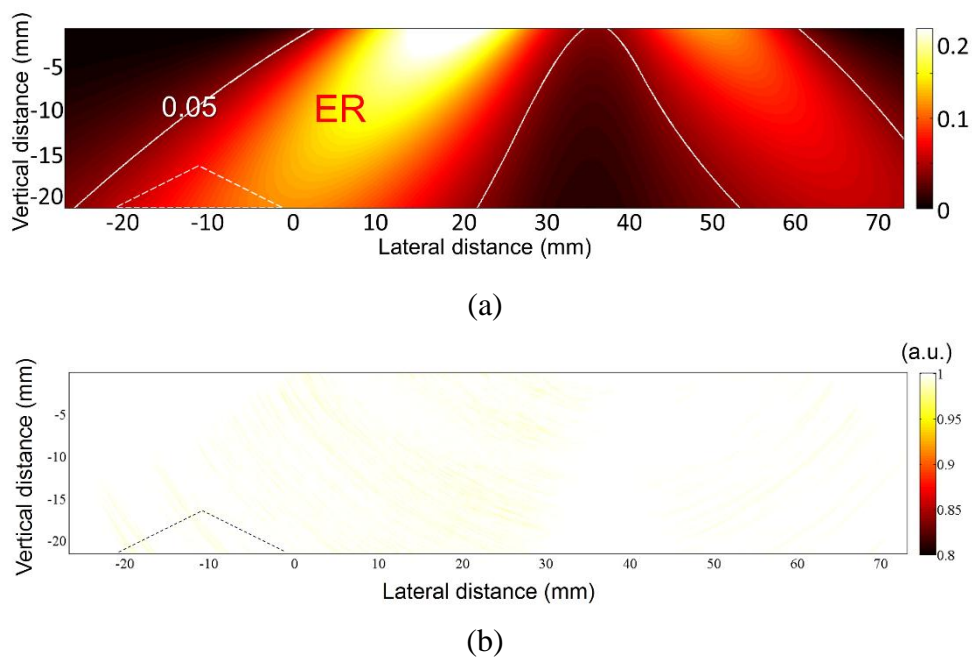


Figure 4.22 Triangular notch: $L = 1$ mm T-mode; (a) ER and (b) SSIM-MAP.

4.5 Summary

Objective II: To confirm the characteristics of AWS-SAFT

This chapter focused on the performances of AWS-SAFT in solid-solid angle beam test. Two strong points of AWS-SAFT, similar to fluid-solid two-phase media in chapter 3, were confirmed as follows:

- (1) Artifacts from L-mode bottom echoes and multiple reflections can be eliminated in T-mode results, thus helps to avoid wrong justification of engineer and inspector.
- (2) Defect image in AWS-SAFT is more distinctive from background noises than SAFT because noises in the regions where intensity of ABR are low would be suppressed.

One drawback of AWS-SAFT is that pixel value over the region closed to the interface will be highly amplified, thus it may obscure the defect information in such region. However, this drawback can be overcome by using SSIM index, explained in **Appendix A**.

Objective III: To propose an effective way to use AWS-SAFT

ER technique was proposed and verified in section 4.3. Region in either L- or T-mode where ABR intensities are over 0.05 is defined as ER which is the region where image capability is remarkably high. ER for L-mode is the region underneath the transducer where it is the inclined region approximately 45° direction for T-mode. ER technique is very useful in helping engineer and inspector select an appropriated transducer for a geometrically known specimen.

Finally, ER technique was demonstrated using a case study on imaging of steel bottom defect, restrained by an inspection limit. Imaging capability was well predicted using ER technique. However, for a triangular notch, ER technique cannot predict the imaging capability correctly, because the ultrasonic waves reflected to another side and cannot be acquired by the PA.

List of Publication for AWS-SAFT in solid-solid angle beam ultrasonic test

Journal paper

1. Worawit Padungsriborworn, Akira Furukawa, Sohichi Hirose: Applicability of Effective Region Technique in Ultrasonic Imaging by AWS-SAFT, Journal of JSCE, 2015. (Accepted on 31 August 2015, Tentative to be published on 20 October 2015)

Domestic conferences

- I. Worawit Padungsriborworn, Akira Furukawa, Sohichi Hirose: 超音波伝搬特性を考慮した開口合成法の改良と鋼板裏面の画像化, JSCE Annual conference 2014, Sep.2014.
- II. Worawit Padungsriborworn, Akira Furukawa, Sohichi Hirose: Automatic Steel Plate Bottom Flaw Detection by the Use of MSSIM in Ultrasound Imaging, The 63rd National Congress of Theoretical and Applied Mechanics, Sep.2014.
- III. Worawit Padungsriborworn, Akira Furukawa, Sohichi Hirose: Ultrasound Imaging of Steel Plate by AWS-SAFT, Proceedings of the JSNDI Autumn conference 2014, pp.47-48,Oct.2014.
- IV. Worawit Padungsriborworn, Akira Furukawa, Sohichi Hirose: Improvement of SAFT in Ultrasound Imaging of Two-Phase Media, The 7th Thailand-Japan International Academic Conference 2014, Nov.2014.
- V. Worawit Padungsriborworn, Akira Furukawa, Sohichi Hirose: Decisive Assessment of Effective Region for Flaw Detection in Ultrasound Imaging by AWS-SAFT, Proceedings of the 22nd Symposium on Ultrasonic Testing, pp.1-4 ,Jan.2015.

Chapter 5: *Conclusion*

5.1 Review of dissertation

AWS-SAFT, an improved version of SAFT, a typical method for ultrasound imaging, was developed using the implementation of Approximate Wave Solution (AWS) for ultrasonic beam radiation. Characteristics (or improvement effects) of AWS-SAFT was investigated in: (1) Fluid-solid water immersion test and (2) Solid-solid angle beam ultrasonic test. Results from both cases well verified the characteristics of the proposed AWS-SAFT. With the understanding of such characteristics, efficient method for applying AWS-SAFT with both cases was proposed and demonstrated.

Moreover, ER technique was found as a by-product of this studying and it can be used to determine effective region, where high imaging capabilities can be anticipated, in ultrasound imaging.

5.2 Summary of findings

Chapter 2: (to accomplish Objective I)

AWS-SAFT was proposed with the following points:

- 2.1. Ultrasonic beam radiation can be accounted into SAFT using multiplication.
- 2.2. Ultrasonic beam radiation computed from AWS was verified using actual beam measurement. However, only L-mode could be confirmed. It can be considered that changing of receiving transducer and couplant to ones of the transverse wave may help, however the experimental setup will be much difficult.

Chapter 3: (to accomplish Objective II and III)

The followings were confirmed in fluid-solid water immersion test:

- 3.1. Using AWS-SAFT, improved ultrasound image can be obtained if SDH located inside the ER of either mode. Such improvements are: (a) flaw image with narrower side lobes and (b) overall noise reduction
- 3.2. Using AWS-SAFT, artifacts of L-mode which are normally observed in T-mode SAFT image can be eliminated.
- 3.3. Noises outside the ER can be remarkably reduced.
- 3.4. A drawback of AWS-SAFT: If an SDH is located outside the ER, noises inside

the ER will be highly amplified hence the image of SDH outside the ER get suppressed and may be obscured.

Efficient way to use AWS-SAFT in imaging of an immersed rod specimen is proposed as the following 2 steps:

Step 1: Conduct two tests, one where the phased-array transducer (PA) is placed over a rod specimen, and another where the PA is placed under a rod specimen.

Step 2: Obtain both L- and T-modes AWS-SAFT results so the superposition of ERs from both modes cover most area of a rod specimen.

Chapter 4: (to accomplish Objective II and III)

The followings were confirmed in solid-solid angle beam ultrasonic test:

- 4.1. Using AWS-SAFT, artifacts from L-mode bottom echoes and multiple reflections can be eliminated from T-mode results, which helps to avoid wrong justification of engineer and inspector.
- 4.2. Defect image in AWS-SAFT is more distinctive from background noises than SAFT because noises in the regions where intensity of Approximate Beam Radiation (ABR) are low would be suppressed.
- 4.3. A drawback of AWS-SAFT: pixel value over the region closed to the interface will be highly amplified, thus it may obscure the defect information in that region. However, this drawback can be overcome by using the SSIM index.

ER was defined as the region where image capability is remarkably high and can be predicted using the region where ABR intensities are over 0.05. ER for L-mode is the region underneath the transducer, where it is the inclined region approximately in $\pm 45^\circ$ directions for T-mode. The use of computed ABR to determine effective region for ultrasound imaging is called the ER technique.

ER technique is very useful tool in helping engineer and inspector to select an appropriate transducer for a specimen with known geometry. ER technique was demonstrated using a case study on imaging of steel bottom defect, restrained by an inspection limit. Imaging capability was well predicted, excepted for the case of triangular notch.

5.3 Limitation in using the AWS-SAFT

This section suggest the principles and the limitations which are required to be taken into consideration while using the AWS-SAFT.

The principles:

1. ERs shall be computed beforehand and they must cover the ROI of the target, because AWS-SAFT can reconstruct flaw image with higher resolution than SAFT if the flaw is inside the ERs of either L- or T-modes.
2. If the AWS-SAFT image appears like the ERs of either L- or T-modes, it can be implied that there is no flaw in the ERs.
3. It is highly recommended but not compulsory to use SSIM-MAP (**Appendix A**) in viewing results in order to eliminate the strong echoes from the interface which is likely to obscure the flaw image.

The limitations:

1. AWSs are currently available for planar and curve interfaces.
2. This method can detect the presence of flaw, but it is difficult to determine the size and shape.
3. This method can be used for any homogeneous and isotropic materials.
4. Sizes of detectable flaws should not be smaller than the wavelength of the ultrasonic waves used in the test. Increasing the frequency can help minimizing the wavelength with the exchange of higher attenuation.
5. Shapes of flaws which can be detected are rectangular and circular, while it is difficult for a triangular one due to the wave scattering characteristics.
6. Types of defects which can be detected are cavity type. For other types such as inclusion, it is required to be further tested, however, the same principles are considered applicable.

5.4 Future work

At this stage, AWS-SAFT was developed for 2-D problem using a linear phased-array transducer. In the future, 3-D AWS-SAFT can also be developed since the AWS equations itself are originally derived in 3-D space. Trial of this technique in detection of flaw inside the concrete is also interesting. However, using of low frequency may require some additional signal processing.

ER technique can be a powerful tool in helping engineer and inspector to determine the most efficient test configuration for a given problem. However, this technique should be further verified in various inspection configurations such as different materials, transducer sizes and frequencies.

Appendix A: *Structural SIMilarity (SSIM) index*

Image Quality Assessment (IQA) had been used tremendously in the field of image processing to evaluate the quality of distorted image which usually occurs during acquisition, processing, compression, storage, transmission and reproduction. Subjective evaluation by using Human Visual System (HVS) is normally the most correct method. However, it is usually inconvenient hence objective evaluation plays an important role to overcome this problem.

Various method such as mean squared error and peak signal-to-noise ratio are the traditional image quality metrics until the introduction of Structural Similarity (SSIM) Index in 2004 by Zhou Wang et al. [34, 37]. SSIM was proved that it is a tool that highly correlated with HVS [34] and had gained widespread popularity as a tool to assess quality of images and also to evaluate the performance of image processing algorithms and system [38].

Using SSIM index, a reference image which is known as an undistorted image or a benchmark in comparison with any distorted images are required. Suppose \mathbf{x} and \mathbf{y} are two non-negative images and consider \mathbf{x} as an image with perfect quality or a benchmark and \mathbf{y} as a distorted image or the target in which the difference from \mathbf{x} will be computed. SSIM of image \mathbf{y} compared with \mathbf{x} can be calculated by the following equation:

$$SSIM(\mathbf{x}, \mathbf{y}) = \{l(\mathbf{x}, \mathbf{y})\}^\alpha \cdot \{c(\mathbf{x}, \mathbf{y})\}^\beta \cdot \{s(\mathbf{x}, \mathbf{y})\}^\gamma \quad (\text{A1})$$

where α , β and γ in **Equation A1** are indices which can be used to bias the three comparison functions. In this paper, we do not use biased comparison so $\alpha = \beta = \gamma = 1$. Comparison functions for luminance $l(\mathbf{x}, \mathbf{y})$, contrast $c(\mathbf{x}, \mathbf{y})$ and structure $s(\mathbf{x}, \mathbf{y})$ are defined as follows:

$$l(\mathbf{x}, \mathbf{y}) = \frac{2\mu_x\mu_y + C_1}{\mu_x^2 + \mu_y^2 + C_1}, \quad C_1 = (K_1L)^2, \quad (\text{A2})$$

$$c(\mathbf{x}, \mathbf{y}) = \frac{2\sigma_x\sigma_y + C_2}{\sigma_x^2 + \sigma_y^2 + C_2}, \quad C_2 = (K_2L)^2, \quad (\text{A3})$$

$$s(\mathbf{x}, \mathbf{y}) = \frac{\sigma_{xy} + (C_2/2)}{\sigma_x \sigma_y + (C_2/2)}. \quad (\text{A4})$$

In the above-mentioned equations, C_1, C_2 and C_3 are small constants introduced to avoid instability when the denominators are very close to zero. Arbitrary constants K_1 and $K_2 \ll 1$ and L is the dynamic range of the pixel values. Constants used in the MSSIM calculation of this dissertation are $K_1 = 0.01, K_2 = 0.03$ and $L = 1$. μ_x and μ_y are mean intensities of images and can be calculated from **Equation A5**.

$$\mu_x = \frac{1}{N} \sum_{i=1}^N x_i, \mu_y = \frac{1}{N} \sum_{i=1}^N y_i \quad (\text{A5})$$

where N is total number of pixel and σ_x and σ_y are standard deviation of each image which can be calculated from **Equation A6**.

$$\sigma_x = \left(\frac{1}{N-1} \sum_{i=1}^N (x_i - \mu_x)^2 \right)^{1/2}, \quad \sigma_y = \left(\frac{1}{N-1} \sum_{i=1}^N (y_i - \mu_y)^2 \right)^{1/2}. \quad (\text{A6})$$

In **Equation A4**, σ_{xy} is a correlation coefficient of image \mathbf{x} and \mathbf{y} , defined in **Equation A7**.

$$\sigma_{xy} = \frac{1}{N-1} \sum_{i=1}^N (x_i - \mu_x)(y_i - \mu_y). \quad (\text{A7})$$

Using above mentioned equations, SSIM index for any pixels in \mathbf{y} compared to \mathbf{x} can be computed. If $SSIM(\mathbf{x}, \mathbf{y}) < 1$, it means that such pixel in \mathbf{y} contain difference from benchmark \mathbf{x} .

Once the SSIM for every pixels are computed, MSSIM which is mean of SSIM can be calculated from **Equation A8** and it can be used to globally compare the quality of image \mathbf{y} from \mathbf{x}

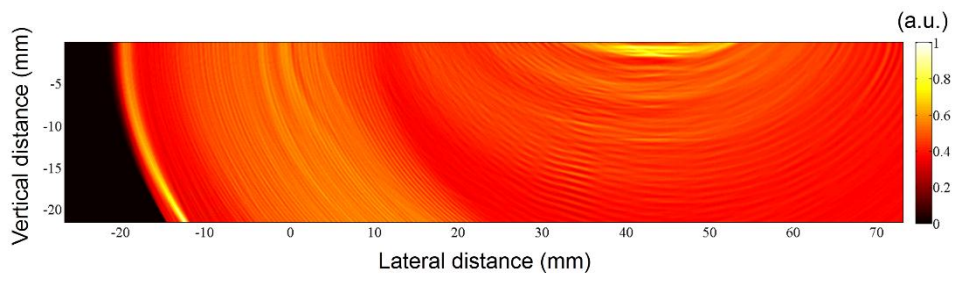
$$MSSIM(\mathbf{X}, \mathbf{Y}) = \frac{1}{M} \sum_{j=1}^M SSIM(x_j, y_j). \quad (\mathbf{A8})$$

MSSIM of image \mathbf{x} which is a benchmark shall be “1” and the smaller the MSSIM of \mathbf{y} than “1” means the more distortion the image \mathbf{y} from a benchmark \mathbf{x} .

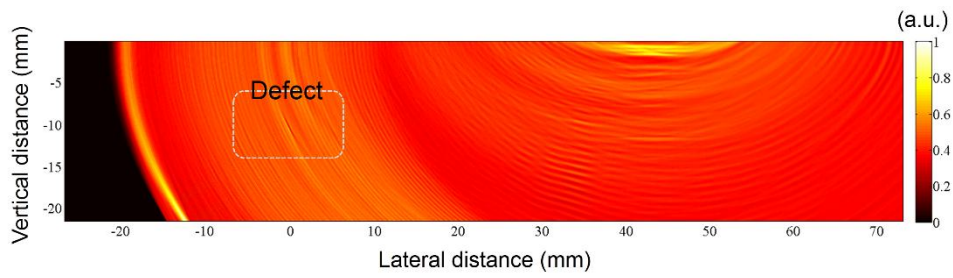
This theory can be applied to NDE problem where ultrasound image of a benchmark or non-defect part is considered as \mathbf{x} and an ultrasound image where the existence of defect is unknown would be considered as \mathbf{y} . Existence of defect can be considered as image difference between \mathbf{x} and \mathbf{y} and plotting of SSIM index, so-called SSIM-MAP, can show the clear location of defect than observing the raw SAFT and AWS-SAFT images.

A sample case from case-T3 in section 4.3 is used here. **Figure A1** shows results obtaining from conventional SAFT and **Figure A2** shows results from AWS-SAFT. SAFT and AWS-SAFT images for non-defect part of test volume are shown in **Figure A1(a)** and **Figure A2(a)**, respectively, and they are considered as \mathbf{x} in the computation of SSIM index. SAFT and AWS-SAFT images from region of test volume with defect SDH D3T inside dashed line, are shown in **Figure A1(b)** and **Figure A2(b)**, respectively, and they are considered as \mathbf{y} . Observing the two images, defect image cannot be noticed because of background noises and mutual echoes which are identical to results from non-defect case.

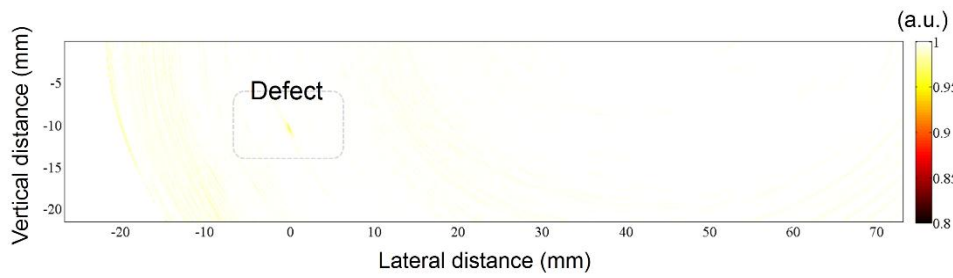
SSIM-MAPs comparing \mathbf{x} and \mathbf{y} are shown in **Figure A1(c)** and **Figure A2(c)** for SAFT and AWS-SAFT, respectively. Defect image which cannot be identified in the raw image results is now identified in both SAFT and AWS-SAFT. Especially in **Figure A2(c)** from AWS-SAFT, defect image is very distinctive from background noises and artificial echoes. This proves the effectiveness of using SSIM-MAP in identifying defect from ambiguous ultrasound images, while also shows the effectiveness of AWS-SAFT in boosting the defect image from background noises and eliminating the artificial echoes.



(a)

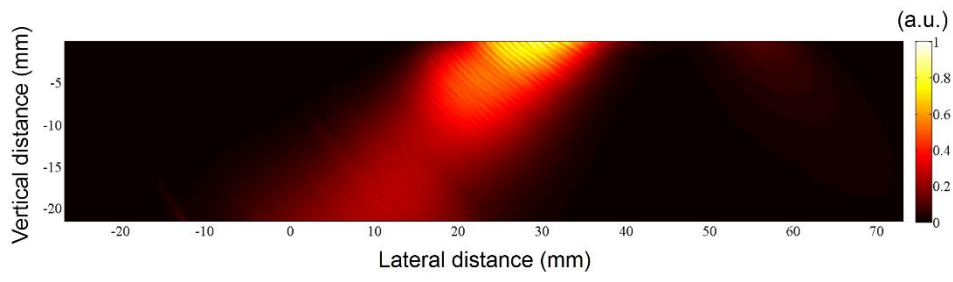


(b)

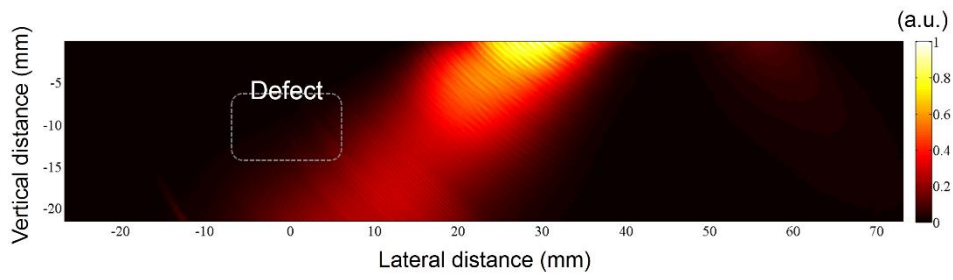


(c)

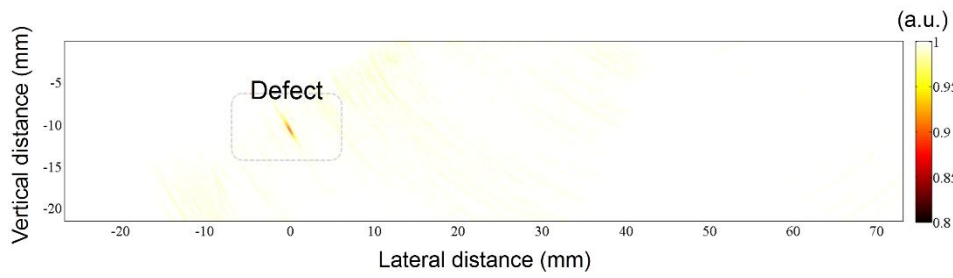
Figure A1 Results from conventional SAFT;
(a) Non-defect, (b) Defect and (c) SSIM-MAP.



(a)



(b)



(c)

Figure A2 Results from AWS-SAFT;
(a) Non-defect, (b) Defect and (c) SSIM-MAP.

Reference

- [1] AASHTO LRFD Bridge Design Specifications, 6th Edition, American Association of State Highway and Transportation Officials, Washington DC, 2012.
- [2] ACI Committee 345: Guide for Maintenance of Concrete Bridge Members, American Concrete Institute, Michigan, 2006.
- [3] Zhang, W. and Yuan, H.: Corrosion fatigue effects on life estimation of deteriorated bridges under vehicle impacts, *Engineering Structures* 71, 128-136, 2014.
- [4] Wenzel, H.: *Health Monitoring of Bridges*, John Wiley & Sons, Ltd, United Kingdom, 2009.
- [5] T.O. 33B-1-1, *Nondestructive Inspection Methods, Basic Theory*, Technical Manual, United States Army, 2007.
- [6] Achenbach, J.D.: Quantitative nondestructive evaluation, *International Journal of Solids and Structures* 37, 13-27, 2000.
- [7] Light, G.M.: *Comparison of Imaging Capabilities Between Ultrasonics and Radiography*, SwRI Project 14.07558, Southwest Research Institute, San Antonio, Texas, 2004.
- [8] Moran, T.L., Ramuhalli, P., Pardini, A.F., Anderson, M.T. and Doctor S.R.: *Replacement of Radiography with Ultrasonics for the Nondestructive Inspection of Welds – Evaluation of Technical Gaps – An Interim Report*, Pacific Northwest National Laboratory for the United States Department of Energy Contract DE-AC05-76RL01830, Richland, Washington, 2010.
- [9] Frederick, J.R., Seydel, J.A. and Fairchild, R.C.: *Improved ultrasonic non-destructive testing of pressure vessels*, US Nuclear Regulatory Commission Report NUREG-0007-1, University of Michigan, Ann Arbor, Michigan, 1976.
- [10] Sherwin, C.W., Ruina, J.P. and Rawcliffe, R.D.: *Some Early Developments in Synthetic Aperture Radar Systems*, *IRE Transactions on military electronics* 5, 111-115, 1964.
- [11] Seydel, J.A.: *Ultrasonic synthetic aperture focusing techniques in NDT*, *Research Techniques in Nondestructive Testing* 6, 1-47, 1983.
- [12] Doctor, S.R., Hall, T.E. and Reid, L.D.: *SAFT – the evolution of a signal processing technology for ultrasonic testing*, *NDT International* 19 No.3, 163-167, 1986.
- [13] Thomson, R.N.: *Transverse and longitudinal resolution of the synthetic aperture focusing technique*, *Ultrasonics* 22 Issue 1, 9-15, 1984.
- [14] Schmitz, V., Chakhlov, S. and Muller, W.: *Experiences with synthetic aperture*

- focusing technique in the field, *Ultrasonics* 38, 731-738, 2000.
- [15] Fenn, A.J., Temme, D.H., Delaney, W.P. and Courtnet, W.E.: The Development of Phased-Array Radar Technology, *Lincoln Laboratory Journal* 12 No.2, 321-340, 2000.
 - [16] Lamarre, A., Moles, M. and Lupien, V.: Phased array ultrasonic inspection of friction stir weldments, in: D.O. Thompson, D.E. Chimenti (Eds.), *Review of Progress in Quantitative Nondestructive Evaluation* 19, Plenum, New York, 1333-1348, 1999.
 - [17] Drinkwater, B.W., Wilcox, P.D.: Ultrasonic arrays for non-destructive evaluation: A review, *NDT&E International* 39, 525-541, 2006.
 - [18] Lingvall, F., Olofsson, T. and Stepinski, T.: Synthetic aperture imaging using sources with finite aperture: Deconvolution of the spatial impulse response, *J.Acoust. Soc. Am.* 114 (1), 225-234, 2003.
 - [19] Stepinski, T.: An Implementation of Synthetic Aperture Focusing Technique in Frequency Domain, *IEEE Transactions on ultrasonics, ferroelectrics, and frequency control* 54 No.7, 1399-1408, 2007.
 - [20] Matsuoka, C., Nakahata, K., Baba, A., Kono, N. and Hirose, S.: Comparative study on ultrasonic imaging methods with array transducers, in: D.O. Thompson and D.E. Chimenti (Eds.), *Review of Progress in Quantitative Nondestructive Evaluation* 35, *AIP Conference Proceedings* 975, 707-714, 2008.
 - [21] Bazulin, E.G.: Imaging of Flaws with Allowance for Multiple Reflections of Ultrasonic Pulses from Plane-Parallel Boundaries of a Tested Object, *Russian Journal of Nondestructive Testing* 43 No.7, 48-70, 2007.
 - [22] Bazulin, E.G.: Obtaining Flaws Images that Take the Effect of Multiple Ultrasonic Pulse Reflections from the Boundaries of a Test Object into Account, *Russian Journal of Nondestructive Testing* 46 No.10, 34-58, 2010.
 - [23] Spies, M., Rieder, H., Dillhöfer, A., Schmitz, V. and Müller, W.: Synthetic Aperture Focusing and Time-of-Flight Diffraction Ultrasonic Imaging – Past and Present, *J. Nondestruct. Eval.* 31 Issue 4, 310-323, 2012.
 - [24] Schmerr Jr, L.W.: *Fundamentals of Ultrasonic Nondestructive Evaluation – A Modeling Approach*, Plenum Press, New York, 1998.
 - [25] Hirose, S., Nishimoto, S., Maruyama, T. and Nagata, Y.: Improved Ultrasonic SAFT Imaging of Flaws in Structures with Curved Surfaces, in: D.E. Chimenti, L.J. Bond and D.O. Thompson (Eds.), *Review of Progress in Quantitative Nondestructive Evaluation* 36, *AIP Conference Proceeding* 1581, 36-41, 2014.
 - [26] Stepinski, T.: SAFT Performance in Ultrasonic Inspection of Coarse Grained

- Metals, in: Proceeding of the Sixth International Conference in NDE in Relation to Structural Integrity for Nuclear and Pressurized Components, Budapest, Hungary, 2007.
- [27] Digital Imaging Tutorial, <http://www.library.cornell.edu/preservation/tutorial/intro/intro-01.html>, Cornell University, accessed 24 December 2014.
- [28] Skjelvareid, M.H., Olofsson, T., Birkelund, Y. and Larsen, Y.: Synthetic Aperture Focusing of Ultrasonic Data From Multilayered Media Using an Omega-K Algorithm, *IEEE transactions of ultrasonics, ferroelectrics, and frequency control* 58 No.5, 1037-1048, 2011.
- [29] Shih, R.C., Chang, Y.F., Chang, C.H. and Tseng, P.Y.: Ultrasonic Synthetic Aperture Focusing Using the Root-Mean Square Velocity, *J Nondestruct Eval* 33, 12-22, 2014.
- [30] Hutchins, D.A. and Hayward, G.: Radiated fields of ultrasonic transducers, *Physical Acoustics: Ultrasonic Measurement Methods* 19, 1-80, 1990.
- [31] Ding, D., Zhang, Y. and Liu, J.: Some extensions of the Gaussian beam expansion: Radiation fields of the rectangular and the elliptical transducer, *J Acoust Soc Am* 113 No.6, 3043-3048, 2003.
- [32] Huang, R., Schmerr Jr, L.W. and Sedov, A.: Modeling the Radiation of Ultrasonic Phased-Array Transducers with Gaussian Beams, *IEEE Transactions on Ultrasonics, Ferroelectrics, and Frequency Control* 55 No.12, 2692-2702, 2008.
- [33] Schmerr Jr, L.W., Song, J.S.: *Ultrasonic Nondestructive Evaluation Systems: Models and Measurements*, Springer, New York, 2007.
- [34] Wang, Z., Bovik, A.C., Sheikh, H.R. and Simoncelli, E.P.: Image quality assessment: From error visibility to structural similarity, *IEEE Transactions on Image Processing* 13 No.4, 600-612, 2004.
- [35] Photo of Kisogawa bridge, <http://www.yonekou.jp/rack/jisseki.htm>, accessed 24 December 2014.
- [36] Photo of fractured truss at Kisogawa bridge, <http://mietopics.seesaa.net>, accessed 24 December 2014.
- [37] The SSIM Index for Image Quality Assessment, <https://ece.uwaterloo.ca/~z70wang/research/ssim/>, University of Waterloo, accessed 24 December 2014.
- [38] Brunet, D., Vrscay, E.R. and Wang, Z.: On the mathematical properties of the structural similarity index, *IEEE Transactions on Image Processing* 21 No.4, 1488-1499, 2012.